The CHESS Sounding Rocket: Interstellar H_2 Towards β^1 Scorpii and γ Arae

by

Nicholas Kruczek
B.S, Drexel University 2013

A thesis submitted to the
Faculty of the Graduate School of the
University of Colorado in partial fulfillment
of the requirement for the degree of
Doctor of Philosophy
Department of Astrophysical & Planetary Sciences
2019

This thesis entitled:
The CHESS Sounding Rocket: Interstellar H_2 Towards β^1 Scorpii and γ Arae
written by Nicholas Kruczek
has been approved for the Department of Astrophysical & Planetary Sciences

Prof. Kevin France

Prof. James Green

Prof. Nils Halverson

Prof. Jeremy Darling

Prof. Scott Palo

Date:

The final copy of this thesis has been examined by the signatories, and we find that both the content and the form meet acceptable presentation standards of scholarly work in the above mentioned discipline.

Abstract

Nicholas Kruczek (Ph.D., Astrophysical & Planetary Sciences)

The CHESS Sounding Rocket: Interstellar H_2 Towards β^1 Scorpii and γ Arae

Thesis directed by Professor Kevin France

We describe the scientific motivation, technical development, and flight performance of the Colorado High-resolution Echelle Stellar Spectrograph (CHESS). CHESS is a far ultraviolet rocket-borne instrument designed to study the atomic-to-molecular transitions within translucent cloud regions in the interstellar medium. CHESS is an objective echelle spectrograph, which uses a mechanically-ruled echelle, a powered (f/12.4) cross-dispersing grating, and a cross-strip anode microchannel plate detector, and is designed to achieve a resolving power R > 100,000 over the bandpass $\lambda\lambda$ 1000–1600 Å. The final two flights of the instrument (CHESS-3 and CHESS-4) observed β^1 Scorpii (β Sco) and γ Arae (γ Ara). For CHESS-4, we describe our novel method for increasing the resolution of the instrument by physically stressing the echelle grating, introducing a curvature to the surface of the optic. We present flight results of interstellar molecular hydrogen absorption, including measurements of the column densities and temperatures, on the sightlines. For β Sco, we find that the derived column density of the $J'' = 1$ rotational level differs by a factor of 2–3 when compared to the previous observations of Savage et al. (1977). We discuss the discrepancies between the two measurements and show that the source of the difference is likely due to the opacity of higher rotational levels contributing to the $J'' = 1$ absorption wing, increasing the inferred column density in the previous work. We extend this analysis to 9 *Copernicus* and 13 *FUSE* spectra to explore the interdependence of the column densities of different J'' levels and how the H_2 kinetic temperature is influenced by these relationships. Based off of our results, we find a revised average gas kinetic temperature of the diffuse ISM of $T_{01} = 68 \pm 13$ K, 12% lower than the value found in the previous work.

Dedication

To Welch's Fruit Snacks - for always being there through the good times and the bad.

... oh, and to Bethany, she was also around.

Acknowledgments

The work presented in this thesis would not have been possible without the advice, help, and support of my friends, family, and coworkers. My wife Bethany was a continuous source support throughout this entire process (even when I gave her a < 2 weeks notice that I needed to fly to the middle of the Pacific for a month). She was a great sounding board, patient with my schedule and the insanity it brought, and brought the necessary reminder that I needed to stop and breath every once in awhile. My parents and all of my siblings (who are too numerous to list) were never more of a phone call away and were always there to provide encouragement and keep me excited about the work I was doing.

While I turned a lot of the screws on CHESS, the success of the payload was directly tied to the support of my (official and unofficial) advisers. I am first and foremost thankful to Kevin for giving me the space to explore. In my mind, my most valuable experience I had in graduate school was the freedom to dig into lab work and experiment with my own paths to results, and that was only possible thanks to your patience and trust. At the same time, you were always available to provide advice whenever I hit a snag, help me keep the science goals in mind, and to remind me that large error bars aren't necessarily a bad thing. Brian was always available with an explanation for a result I measured or to provide a potential alternative solution to an issue I ran into, which went a long way in helping how I address problems.

My work on CHESS would not have happened without help of Nico, Keri, and Mike K. They got me oriented in the lab, taught me about the systems we rely on, and rescued me when I inevitably broke something. Their commitment to just taking the time to help out and teach is/was a priceless contribution to the lab. Along with that, I'm grateful to all of people that have kept ARL running, lent a helping hand, taught me something new, or asked me a question that reminded me of how little I knew. So, thank you to Bobby, Nick E, Jim Green, Stefan, Arika, Emily, and Alex. It was all of those interactions, both small and

big, that made the process as a whole rewarding and enjoyable. I am also thankful to the Halverson lab group - Nils, Jay, J. T., Greg, and Wendy - their early advice and assistance was pivotal not only to my success in grad school but to my growth as an instrumentalist, in particular helping me step back from the task-at-hand to consider the big picture and the next problem.

Finally, getting a Ph.D. will be cool and all, but I'm pretty sure I just stuck around so that I'd have an excuse to keep hanging out with the friends I made. So thank you to everyone that took part in group dinners and TV, committed to a pub crawl, played on the Isotopes, got beat by Dan Gole at Mario Kart, and went all out for one of Matteo's ridiculously themed parties. You all helped turn Colorado into a place that felt like home.

Contents

List of Figures

List of Tables

1 Introduction

1.1 The Interstellar Medium

The interstellar medium (ISM) is the collection of ions, atoms, molecules, dust, and fields (e.g. interstellar B-fields) that exist in the copious amount of space between stars. While the region containing the ISM is widespread, the concentration of matter is low, accounting for only ∼10–15% of the total mass of the Galactic disk. Its average composition is not surprising, 70.4% of the mass is in H, 28.1% in He, and the remaining 1.5% is in the heavier atoms, referred to as metals, with the three most common being O, N, and C (Ferrière, 2001). About 17% of the hydrogen mass is in the form of H_2 (Draine, 2011), making it the most common molecule in the ISM.

Describing the ISM through raw statistics paints a bland picture since they do not capture the host of on-going physical processes within the medium. Starting with the collapse of dense molecular clouds, stars are born from interstellar matter. The radiation from more massive stars will generate bubbles of ionized matter around the stars themselves. Stellar winds will drive a mixing of these ionized particles and cooler material at the ISM-wind interface. Depending on the initial mass of the stars, some may end their lives in a supernova, generating high energy shockwaves that drive tunnels and holes through the interstellar material. In some cases, they extend vertically through the Galactic disk, punching outward into the lower density galactic halo and showering the Galaxy with ionized particles. An observer could simultaneously look elsewhere in the ISM and see a similar region, long after a supernova has occurred and the matter has had time to cool. There, another dense molecular cloud will exist, its enhanced density a remnant left behind by an old shockwave, preparing to restart the stellar cycle.

In this light, the ISM can be viewed as the backbone of a galaxy, mediating the life cycles of stars and facilitating the transfer of energy throughout the disk. Understanding any one process within it requires knowledge of all of the other on-going interactions, since they provide the inputs to the system. The study of the ISM has therefore been an important line of inquiry, helping to address topics ranging from star formation to the ionization of the intergalactic medium. As will be detailed below, spectroscopic observations of the ISM are necessary to observe the variety of atoms and molecules and the physical conditions in which they exist. The UV bandpass (100–3200 Å) contains the highest density of atomic and molecular transitions of these abundant species, including the host of absorption lines associated with the Lyman and Werner bands of H_2, making it a powerful observational regime (Scowen et al., 2017). Unfortunately, this propensity to interact means that performing ground-based UV observations is not possible, as the atmosphere heavily attenuates any incident light. Instead, large space-based observatories act as the work horses of the UV bandpass.

Of importance to this work is the role sounding rockets have played in the study of the ISM, with the most significant likely being the first ever observations of interstellar H_2 (see Figure 1.1; from Carruthers 1970). Sounding rockets serve a dual purpose. First, they act as a test bed for new technologies, providing an opportunity to flight certify cutting edge hardware in preparation for its use on future large space-based missions. Second, they serve as a flexible observing platform, filling niche observational parameter spaces that are not met by current space-based observatories.

In this work, we present spectroscopic observations of the ISM taken using the *Colorado High-resolution Echelle Stellar Spectrograph* (CHESS) sounding rocket, which was designed to achieve resolving power (R) > 100,000 measurements across a far ultraviolet (FUV) bandpass from $\lambda\lambda$ 1000–1600 Å. In the subsequent introductory sections we provide a review of the morphology of the ISM, the observational diagnostics that are employed to study it, and a summary of the past space-based observatories that have contributed greatly to our present understanding of the molecular content of the ISM. §2 provides an overview of the CHESS instrument, its assembly, performance and flight results. These results are analyzed in §3 and compared to previous observations from the *Copernicus* observatory. Inconsistencies between

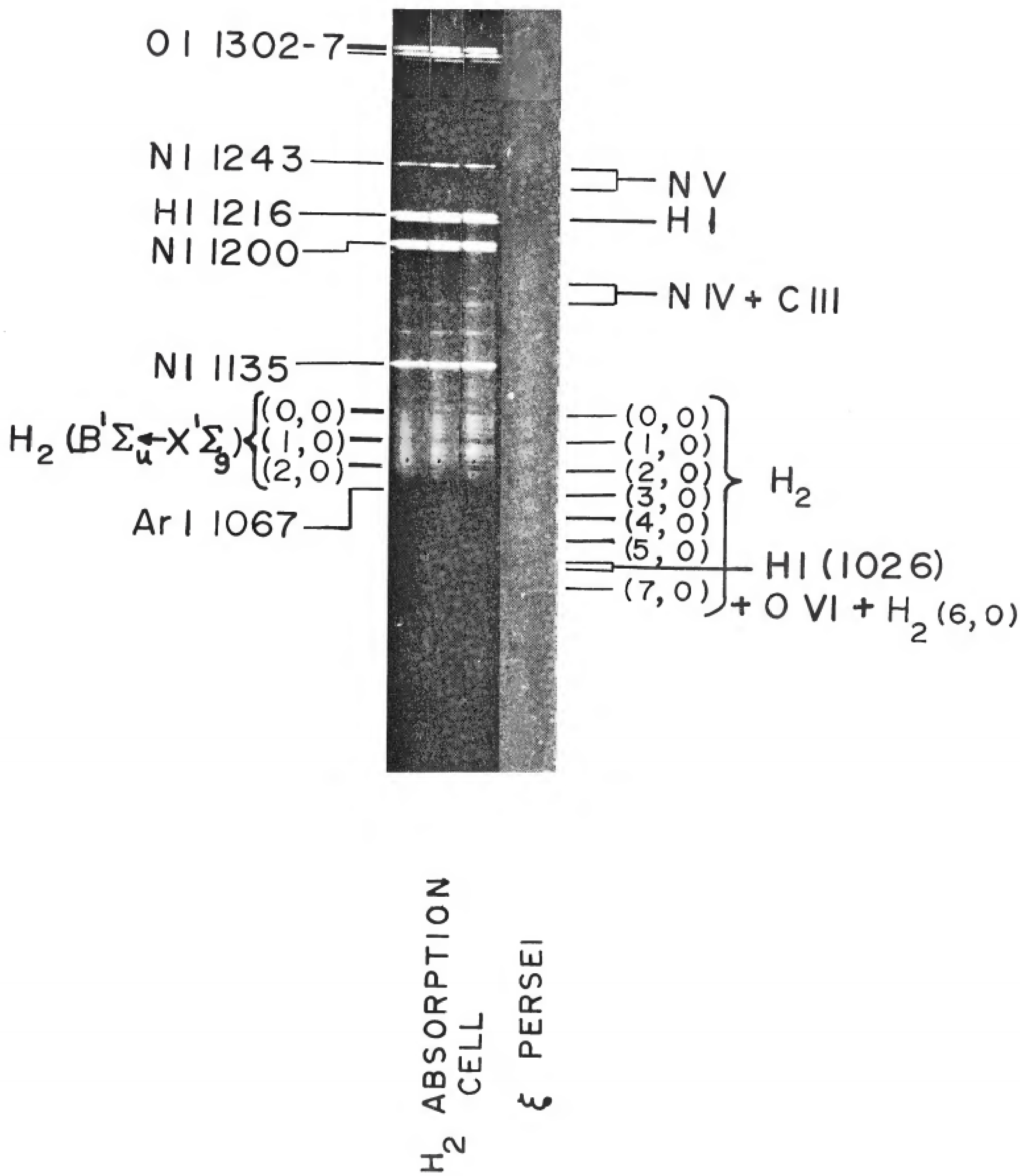

Figure 1.1: From Carruthers (1970) - the first observations of interstellar H_2, taken using a rocket-borne spectrograph. The wider dark strip on the left is a lab spectrum, with several prominent features labeled. On the right is the flight spectrum, showing the absorption features of several H_2 rotation lines.

our results and those of Savage et al. (1977) lead us to reanalyze a sample of *Copernicus* and *FUSE* data in order to correct the column densities measured by Savage et al. (1977) (§3.3). In §4, we summarize our results as well as discuss our continued efforts in the development of new technologies for potential future UV observatories, such as the *Large UV/Optical/IR Surveyor* and the Habitable Exoplanet Observatory that are currently under study.

1.2 Phases of the ISM

The roots of the current model of the ISM began with the observation of CN, CH, and CH^+ absorption lines at optical wavelengths (see e.g. Merrill 1934; Swings & Rosenfeld 1937). The regions in which these molecules existed and their formation pathways were not well understood (Gerin et al., 2016) until 21-cm observations of radio sources showed signs of absorption that were later attributed to clumps of neutral H along the sightline (Hagen & McClain, 1954; Hagen et al., 1954, 1955). Further observations were used to demonstrate that the total observed 21-cm profile, in emission and absorption, was best described by two populations of H, one cool (T $\sim$ 100 K) and one hot (T $\sim$ 1000 K) (Clark, 1965). This hypothesis was supported by the work of Field et al. (1969), who developed a model that used heating from cosmic rays to generate two hydrogen populations at different temperatures, existing in pressure equilibrium with each other. This idea established the two phase model of the ISM. These two phases are known today as the Cold Neutral Medium (CNM) and Warm Neutral Medium (WNM).

There are far more energetics to account for within the ISM than just cosmic ray heating. Understanding how they impact the ISM requires observations across the entire electromagnetic spectrum. Around the time that Field et al. were developing their description of the two phase ISM, sounding rocket observations (Henry et al. 1968; Baxter et al. 1969 appear to be the earliest) of background X-rays (E = 0.1–14 keV) found excess low energy fluxes when compared to the extrapolated power law that was expected based on measured high energy fluxes. At longer wavelengths, O VI was also observed in FUV stellar spectra (Jenkins &

Meloy, 1974). The suggested source for both of these observed phenomena was regions of hot (T $\sim 10^6$ K), low density gas that was thermally emitting in the soft X-ray and capable of maintaining an ionized population of O VI (York, 1974; Burstein et al., 1977). This lead to the creation of an updated three phase ISM model by McKee & Ostriker (1977), who accounted for this additional temperature phase by including large energy injections that were produced by supernovae. These blasts would sweep up and destroy the cold dense clouds, leaving hot, highly ionized species in their wake, generating what is presently known as the Hot Ionized Medium (HIM).

A fourth phase was discovered along similar timelines as the other three, although it seems to be excluded from those models. The first observational evidence came from Hoyle & Ellis (1963), who found a fall off in radio flux at frequencies below 5 MHz, which they attributed to absorption by a layer of ionized gas. Further evidence came from the measured dispersion as a function of frequency in the arrival time of signals from pulsars, indicating that the radio waves were traveling through a plasma (Manchester, 1972; Guélin, 1974). Finally, Reynolds et al. (1973) observed diffuse Hα emission, generated by hydrogen recombination, indicating that a bulk of the gas was in the form of ionized H. The source for this ionization was initially unclear, hot stars have the energy to produce it but the cooler phases of the ISM are optically thick enough that the extent of the stellar radiation is limited. To resolve this issue, it is necessary to consider a complete picture of the ISM environment. As a supernova expands, not only will it generate the HIM phase of the ISM, it will also drive out other matter, leaving behind large bubble and tunnel structures that act as pathways for ionizing photons. The result of this is that the light from nearby stars is able to create ionized media out to heights of $\sim$1 kpc from the mid-plane (Wood et al., 2010; Hill et al., 2015). This phase is known as the Warm Ionized Medium (WIM).

Table 1, adopted from Klessen & Glover (2016), lists the temperatures and densities of each of these phases. The coldest phase of the ISM spans a comparably small temperature range and volume of interstellar space ($\sim$1–2%), yet it contains approximately half of the

Phase	Temperature (K)	Density (cm^{-3})	Common Tracers
Molecular	10–20	$>10^2$	CO
Cold Neutral Medium (CNM)	50–100	20–50	H_2
Warm Neutral Medium (WNM)	6–10 $\times 10^3$	0.2–0.5	H I 21-cm
Warm Ionized Medium (WIM)	$\sim$8000	0.2–0.5	Hα
Hot Ionized Medium (HIM)	$\sim 10^6$	10^{-2}	O IV, Diffuse X-rays

[a] Table adopted from Klessen & Glover (2016), with data from Stark et al. (1992); Caselli et al. (1998); Ferrière (2001); Caselli et al. (1998); Wolfire et al. (2003); Jenkins (2013)

Table 1: Phases of the ISM

mass of the ISM and it is comprised of a variety of chemical constituents in a range of physical conditions (Ferrière, 2001). For this reason, it is useful to further classify the cold ISM. In this work, we follow the scheme proposed by Snow & McCall (2006), which classifies ISM regions using the local properties along a line of sight, particularly the local fraction of an atom or molecule, instead of the bulk line of sight properties, such as the column density or visual extinction. This is an important distinction because bulk properties do not tell the whole story. A high H_2 column density could indicate a single large, dense, molecular cloud or several less dense clouds. Therefore, a clearer understanding is obtained if effort is made to classify a sightline as a sum of its constituents, which in turn requires high resolution observations to distinguish contributions from each component.

1.2.1 The Cold ISM

Table 2, adopted from Snow & McCall (2006), lists information on the four subclassifications of the cold ISM and the local fractions that define them. The two atoms that are used as tracers of the different cloud types are H and C. H is important due to its abundance and its ability to shield molecular clouds from dissociating FUV radiation. H_2 in particular interacts strongly with UV and so its presence has a sizable impact on the intensity of the local radiation field deeper inside clouds. C exists in several forms across the cold ISM, acting as a key component of the chemistry in each case. The free electrons generated when C^+ is formed are able to destroy ionized molecules. Neutral C is highly reactive, acting as a

	Diffuse Atomic	Diffuse Molecular	Translucent	Dense Molecular
Defining Characteristic	$f^{n}_{H_2} < 0.1$	$f^{n}_{H_2} > 0.1$; $f^{n}_{C+} > 0.5$	$f^{n}_{C+} < 0.5$; $f^{n}_{CO} < 0.9$	$f^{n}_{CO} > 0.9$
n_H [cm^{-3}]	10–100	100–500	500–5000	$>10^4$
T [K]	30–100	30–100	15–50?	10–50

[a] Table adopted from Snow & McCall (2006)

Table 2: Classification of cold ISM cloud types

driver in the formation of a variety of molecules. CO is the second most abundant molecule in the ISM and acts as a useful probe for the densest clouds (see Dickman 1975; Martin & Barrett 1978 for some of the earliest work). Therefore, the local fractions (f^n) of interest are those of H_2 [$f^{n}_{H_2} = 2n(H_2)/n_H$], C^+ [$f^{n}_{C+} = n(C^+)/n_C$], and CO [$f^{n}_{CO} = n(CO)/n_C$], where n(X) is the number density of a specific species and n_Y is the total number density for a given atom (e.g. $n_C = n(C) + n(C^+) + n(CO)$).

Describing the cold ISM using these different cloud types is really a method of classifying the response of the ISM to UV radiation, as shown in Figure 1.2 (from Snow & McCall 2006). Diffuse atomic clouds are the lowest density clouds and so UV light is able to fully penetrate them. Any molecules will undergo photodissociation and atoms with lower ionization potentials (like C) will be ionized. As the density increases to the diffuse molecular range, the matter begins to significantly attenuate the light, allowing H_2 to form on the surfaces of dust grains (§1.5.3). The light is not attenuated enough to adequately shield C and so C^+ is still the primary form of the atom. In the translucent clouds range, most of the hydrogen is in H_2 and that provides enough shielding that C^+ is no longer the main form of C. Finally, dense molecular clouds are environments with high optical depth in which the radiation is so attenuated that CO is able to form, primarily through gas phase interactions between C^+ and OH (Snow & McCall, 2006). Following convention, the term “cloud” will be used in reference to any of the regions mentioned above, even when they may not be existing as an individual structure. As an example, a translucent cloud may actually be the outer layer of a dense molecular cloud (van Dishoeck & Black, 1989).

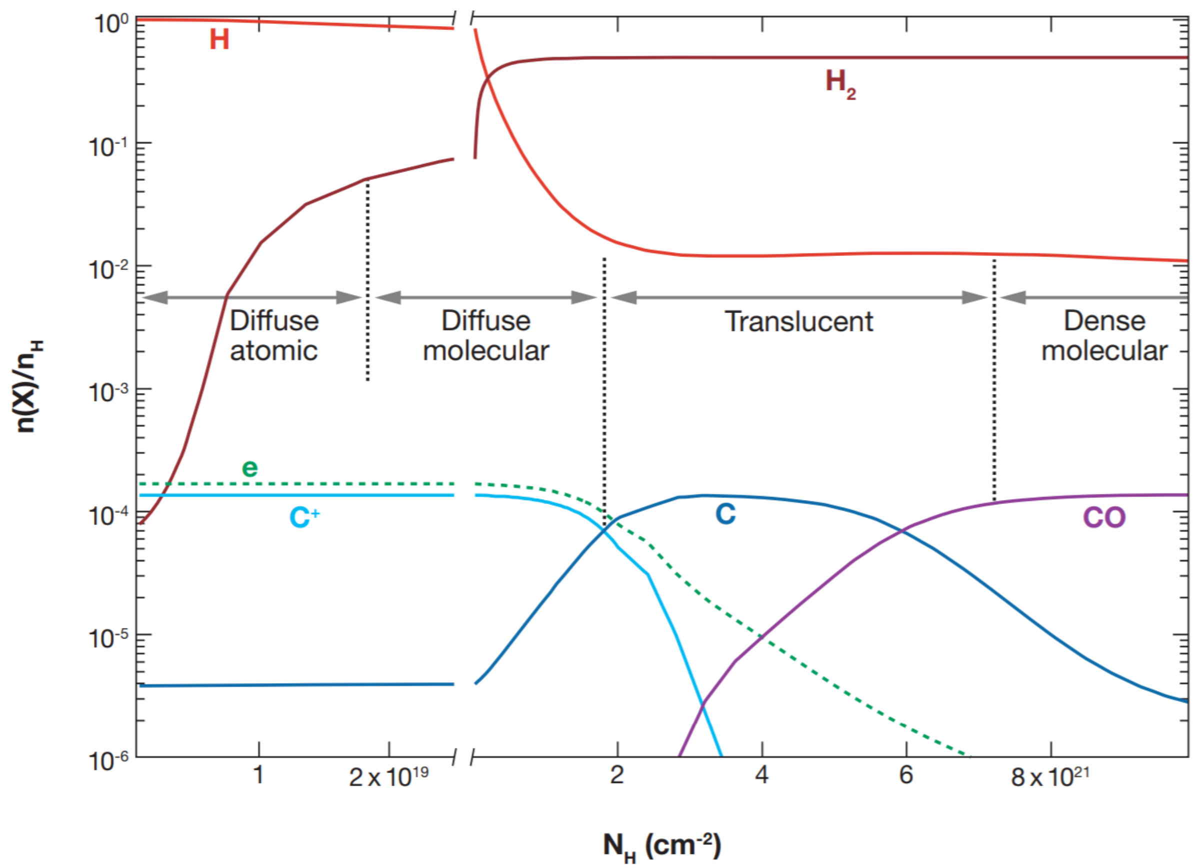

Figure 1.2: From Snow & McCall (2006). The relative densities of H and C in their different forms, illustrating the definitions of cloud types in the CNM. The y-axis is the ratio of the number density of a given species shown on the plot to the total H number density [$n_H = n(H) + 2n(H_2)$].

1.3 UV Observations of the ISM

There are generally two separate paths of study for the different cloud types (Crutcher, 1985; van Dishoeck & Black, 1989). At long wavelengths ($\lambda\lambda$ IR–radio), H_2 transitions are forbidden (§1.4.3) but an array of diatomic and more complex molecules, including CO, are observed in emission, making this wavelength range important for studying dense molecular clouds. There are exceptions to the above restrictions, such as H_2 absorption being observed along very dense (N(H_2) $\sim 10^{22}$ cm^{-2}) lines of sight (Lacy et al., 1994), but each case is a niche measurement rather than a broadly applicable result. At short wavelengths ($\lambda\lambda$ UV–optical), the rotational levels of molecules, including H_2, CH, and CH^+, and a variety of atomic transitions can be directly observed in absorption. If the optical depth of dust along a line of sight is too large, these measurements will be impossible due to extinction. For this reason, the short wavelength observations were historically limited to the diffuse clouds (see, e.g. Spitzer et al. 1973). While both observational techniques have their merits, their corresponding limitations makes the two methods complimentary to each other.

The composition of translucent clouds places them on the boundary between these two observational regimes, historically making them difficult to study. Yet they also exist in the density regime where the UV portion of the radiation field will be most important since their composition becomes complex towards their interiors while simultaneously remaining optically thin enough for UV photons to penetrate and have an impact. As UV technology advanced, introducing detectors with higher sensitivity and instruments with better spectral resolution, this outlook began to change. Most notably, the *Far Ultraviolet Spectroscopic Explorer* (*FUSE*) spectrograph (Moos et al., 2000) made high resolution ($\sim$15 km s^{-1}) surveys over an FUV bandpass possible. Preliminary analysis of sightlines with moderate extinction did not show signs of any translucent clouds, lending support to a definition for clouds that was not based on bulk line of sight properties alone (Rachford et al., 2002). Several groups used *FUSE* observations of H_2, combined with observations of C I and CO from the *Space Telescope Imaging Spectrograph* (*STIS*) (Woodgate et al., 1998) to more definitively observe translucent clouds (Burgh et al., 2007; Sonnentrucker et al., 2007; Sheffer et al., 2008). Burgh et al. (2010) further updated the guidelines of Snow & McCall (2006), suggesting that a suitable criteria for discriminating between diffuse and translucent clouds is N(CO)/N(H_2) $> 10^{-6}$ and N(CO)/N(CI) ~ 1.

Beyond searching for individual clouds along a sightline, UV spectroscopic observations provide a wealth of information that is crucial for understanding the dynamics across all phases of the ISM. By observing the ISM on a local scale, we get an up-close and three dimensional view of these ongoing interactions. At high spectral resolution, individual cloud structures, motions, and interactions with neighboring phases can all be observed. The knowledge gained from these observations can then be applied to more distant regions of the ISM or even other galaxies (McCray & Kafatos, 1987; Dickey & Lockman, 1990; Redfield, 2006; France et al., 2016).

Abundances of less common molecules and elements provide constraints on the cooling rate of clouds. Cooling occurs when atoms and molecules undergo collisional excitation followed by radiative de-excitation. The low internal temperatures of these clouds fall within the range of the fine structure transitions of common atoms and ions, such as C, C^+, and O, making them major sources of cooling in this regime (Dalgarno & McCray, 1972; Hollenbach & Tielens, 1997). This is compared to H_2 which, while common and capable of cooling through slow rotational transitions, is also an important contributor to the overall heating within the cloud through excitation by cosmic rays and evaporation from dust grains after formation (Hollenbach & Tielens, 1997; Ferrière, 2001).

Depletion of metals acts as a tracer for dust grain composition. When compared to the solar abundance, which is assumed to be equal to the cosmic abundance (Savage & Sembach, 1996), not only do observations show lower than expected metal abundances (see, e.g., Morton et al. 1973 for an early example, the effect is well documented beyond that) but the amount of depletion varies for different sightlines. The first result is generally accepted to be due to the condensing of the missing elements into dust grains. Therefore, measuring the amount of depletion gives insight into the composition of the dust without the hassle of disentangling the continuum and few emission lines that the dust produces in the IR (Williams, 2005). The fact that the depletions vary for different lines of sight is fundamentally a manifestation of the different histories along them. One sightline may have had a shock front pass more recently, while another remained relatively still. There are published models that work to relate depletion levels between different elements, but they cite a need for more data to confirm their conclusions and expand the applicable range of their work (Jenkins, 2009).

Unlike H_2, CO has a dipole moment and is able to radiate at long wavelengths (λ = 2.6 mm for the ground state rotational transition). At high H_2 densities ($n(H_2) > 100$ cm^{-3}; Sanders et al. 1984), the dominant ground state excitation pathway for CO is through collisions with H_2, making its emission a tracer for H_2. Uncertainties in relating the observed CO intensity to a column density complicates the final relationship between $N(H_2)$ and N(CO) (see, e.g. Bolatto et al. 2013 and references therein). Care must also be taken when extending this relationship down to translucent clouds, since the additional UV radiation will influence the amount and excitation level of the CO (van Dishoeck & Black, 1988). The previously mentioned works of Burgh et al. (2007); Sheffer et al. (2008); and Burgh et al. (2010) began quantifying the relationship between the two values at lower column densities. The lack of currently operational UV observatories that cover the short wavelengths of the FUV bandpass ($\lambda < 1150$ Å) has limited the progress that can be made.

Given the importance of H_2 within almost all clouds, a thorough knowledge of its energy states and pathways of interaction is necessary to understand its structure. In order to facilitate this discussion, we will provide a brief review of the fundamental physics guiding H_2 before going into their implications in present day observations of the ISM.

1.4 Molecular Hydrogen Physics

1.4.1 Energy Levels

In the electronic transitions of atoms, the orbital (L) and spin (S) angular momenta and their sum (J) are the quantum numbers that describe how the atom is allowed to radiate, based on the limitations of how those values can change under an interaction with a photon. This process can be extended to molecules but the description has more considerations due to the additional degrees of freedom. In particular, not only can a molecule undergo transitions where an electron is excited to a higher orbital, it can also be vibrationally excited, where the nuclei oscillate about the center of mass, and rotationally excited, where the nuclei spin about the various axes. While this discussion is applicable to a variety of different molecules, from the comparably simple H_2 to something more complicated like NH_3, I will restrict the summary to cover H_2 in conditions similar to those found in translucent clouds since that is most applicable to the content of this thesis. The references used to motivate this review on H_2 energy levels and selection rules is drawn primarily from Herzberg (1950), with support from Field et al. (1966); Rybicki & Lightman (1979); Shull & Beckwith (1982); and Draine (2011). Additional sources are cited within the text.

The simplest method for deriving the energy levels is to treat them all as independent, with the total energy of the molecule equal to the sum of the three energy states. Treating the states as independent requires that the electrons are uncoupled from the motions of the nuclei, which can be accomplished using the Born-Oppenheimer approximation. This assumption states that the speed of the electrons is large compared to the of the nuceli and so the electrons effectively see the nuclei as stationary particles. In that case, the electronic state will not depend on the kinetic motions of the nuclei and the energy levels of the two can be treated separately.

An example diagram of a molecular energy level is shown in Figure 1.3, demonstrating the relative scales of the different energy terms. The large red curves are the nuclear poten-

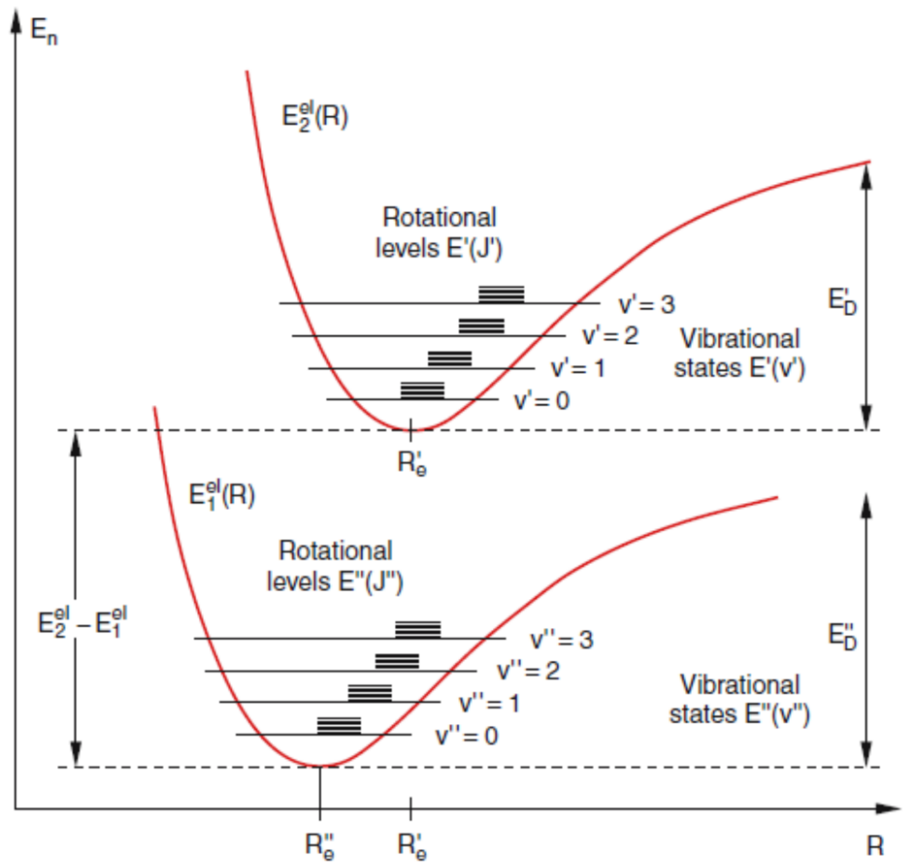

Figure 1.3: From Benedict (2011). A schematic drawing of the electronic ($E_1(R)$ and $E_2(R)$), vibrational (v′ and v″), and rotational (black boxes of lines) levels within a molecule. The x-axis (R) is the internuclear distance and the y-axis is the total energy.

tials in two different electronic energy levels, with the energy level spacing defined by the difference between the minima of the potentials. The nuclei can oscillate in the potential well at quantized vibrational energies. These levels are shown as horizontal lines within the potential well. While it is not shown in the diagram, vibrational levels can exist above the nuclear potential curve, as R goes to infinity. In that case, the nuclei have enough energy to dissociate. Those energy levels form the H_2 dissociation continuum that results from electronically excited H_2 molecules cascading to a level that has enough energy for them to separate. Finally, the rotational levels are displayed in between each vibrational level as closely spaced black lines.

As shown in Figure 1.3, the rotational energy levels have the smallest separation. The derivation of the energy level spacing can be done by treating the H_2 as a rotating dumbbell. Since the molecule will be vibrating as well as rotating, the most accurate result is found by treating the nuclei as bound together by a spring (known as a nonrigid rotator). This distinction is important because it accounts for variation in the moment of inertia that will occur as the spacing between the nuclei varies. Starting from the simpler case of a rotator with a fixed rod in the middle, the energy levels of the system can be found using the reduced mass (μ), moment of inertia ($\mathrm{I} = \mu \mathrm{r}^2$), and Schrödinger's equation to find:

$$E_{\text{rot}} = \frac{\hbar^2 J(J+1)}{2I} \tag{1}$$

This result can be extended to the nonrigid case using the centrifugal force and restoring force of the spring to calculate the updated energy levels.

$$E_{\text{rot}} = BJ(J+1) - DJ^2(J+1)^2 \tag{2}$$

Where B and D are known as the rotational constants. The above equation assumes an average nuclear separation and could be further updated to account for small changes to the mean separation, as a function of vibrational state, resulting in a small linear addition to B and D that has been omitted here.

Changes in rotational energy levels require changes in the total angular momentum. It is important to consider what types of rotational transitions are possible since a significant portion of interstellar H_2 exists in the rotationally-excited ground electronic state. As a molecule rotates, it can emit a photon through a multipole transition, the fastest being the electric dipole transition. For the electric dipole transition to happen, the molecule must have a permanent or induced dipole moment. The probability (P) of a transition occurring is proportional to:

$$P \propto \int_{\text{all space}} \psi_n^* \vec{M} \psi_m \tag{3}$$

Where $\vec{M}$ is the vector dipole moment and ψ_n and ψ_m are wavefunctions of the initial and final states.

An important rule related to this transition is that the overall parity, or symmetry of the wavefunction across the origin, must change in the transition in order for the integral to be non-zero. This is due to the fact that the dipole moment is anti-symmetric across the origin and so the integral in Equation 3 will be zero unless the product of the wavefunctions is also anti-symmetric. This is equivalent to saying the integral of an odd function over a symmetric interval is zero.

In molecules, the symmetry of their wavefunctions is the same for all even J levels and for all odd J levels. This means that any transition where the difference in J between the initial and final level is an even integer is forbidden, since it would go between two levels with the same symmetry. For that reason, electric dipole transitions must have $\Delta \mathrm{J} = \pm 1$ for two atom molecules. The same arguments apply to higher electric and magnetic multipoles, but with different restrictions on parity. Of particular interest is the electric quadrupole because H_2 is a homonuclear molecule that does not have a dipole moment. It does have an electric quadrupole moment, allowing for transitions with $\Delta \mathrm{J} = \pm 2$. The energies associated with rotational transitions are typically on the scale of thousandths of eVs ($\lambda \gtrsim 1$ mm).

The description of the vibrational state of a molecule can start from a simple harmonic oscillator in parabolic potential well, but must be extended to account for the decreasing attraction between the nuclei as they get further apart. This leads to the decaying potential at larger R seen in Figure 1.3. This correction is accounted for by including higher order expansions in the classical oscillator potential, leading to energy levels given by

$$E_{\mathrm{vib}} = h\omega\Big[(n + \frac{1}{2}) - x_1(n + \frac{1}{2})^2 + x_2(n + \frac{1}{2})^3 + ...\Big] \qquad (4)$$

where h is Planck's constant, ω is the frequency of oscillation and n is the vibrational quantum number, with $n = 0, 1, 2$, etc. $n = 0$ indicates the zero point energy level of the oscillator, which is greater than 0. The first term of the equation is the energy of the classic quantum simple harmonic oscillator, with additional small correction terms (x_1 and x_2, with $1 \gg x_1 \gg x_2$) included to account for the change in potential with increasing nuclear distance.

Classically, the simple harmonic oscillator was restricted to transitions that had $\Delta n = \pm 1$ due to the orthogonality of the vibrational wavefunctions (Sommerfeld, 1930). This restriction no longer holds in the expanded potential because the wavefunctions can be described by Fourier series of oscillating states that contain infinitely many terms. Instead, all that is required is a dipole moment. The probability of a transition is described by the Franck-Condon principle, which says that a vibrational transition is more likely to occur between states with overlapping wavefunctions. This is equivalent to saying that a molecule cannot spontaneously jump to a new position so, as the transition occurs, the molecule will shift to a vibrational state that agrees with the current configuration of the nuclei. The energies associated with vibrational transitions are typically in the range of tenths to hundredths of eV ($\lambda \sim 10$ μm).

The electronic energy levels (E_{elec}) of the molecule are the largest energy levels with separations that, for molecules of astronomical interest, are typically several eV ($\lambda < 1$ μm) in magnitude. In any given state, the total energy of the molecule (within the Born-Oppenheimer approximation) is described by:

$$E_{\mathrm{tot}} = E_{\mathrm{elec}} + E_{\mathrm{vib}} + E_{\mathrm{rot}} \tag{5}$$

1.4.2 Molecular Notation

In atoms, the electric field around the nucleus is spherically symmetric. In that case, orbital angular momentum is conserved and L is a good quantum number (meaning it can commute with the Hamiltonian). In diatomic molecules, the additional contribution to the angular momentum from the molecule rotating about its center of mass (N) and the now cylindrically symmetric electric field means that L is no longer a conserved quantity. Instead, since there is no rotation about the inter-nuclear axis of the molecule, the projection of L along this axis is a conserved quantity (where we also assume that spin-orbit coupling is not a dominant term). In that case, the projected value (Λ) is a good quantum number and it is used to describe the energy state of the molecule. Like the atomic case, Λ is quantized (see notation in Table 3) but the degeneracy is 2Λ (except when $\Lambda = 0$, in which case there is one state) since the projection can only point positive or negative. This work will focus on H_2 in its ground or first two excited states. Since H_2 is a light molecule and $\Lambda = 0$ or 1, it can be described using Hund's case b (Herzberg, 1950). In this case, the small amount of electronic angular momentum about the nuclear axis means that there is only at most a weak magnetic field generated along it and so the electronic spin will not couple to it. The projection of the spin along the axis is then undefined and instead the total electronic spin (S) is a good quantum number and it has a degeneracy of 2S+1. The various angular momentum terms are added together into a total angular momentum J = Λ + S + N.

$\Lambda =$	Σ	Π	Δ	Φ	Γ	...
$\|\Lambda\| =$	0	1	2	3	4	
analogous to	S	P	D	F	G	...

Table 3: The energy level designations of Λ

When describing diatomic and $\Lambda = 0$ molecules, more information beyond the angular momentum and spin is necessary to fully characterize their states. The first term applies to homo-nuclear molecules and relates to the symmetry of the electronic wavefunction under an inversion about the center of the molecules (positions go [x,y,z] $\rightarrow$ [-x,-y,-z]). A molecule is said to be gerade (g) if it looks identical under inversion and ungerade (u) if the electronic wavefunction changes sign under inversion. For molecules in a state with $\Lambda = 0$, we also consider the symmetry of the molecule when it is reflected about a plane containing the inter-nuclear axis. A molecule is given a "+" designation if it looks identical under this reflection and "-" if the wavefunction changes sign under this reflection.

Combined, these designators are used to construct the molecular term symbol in the following manner:

$$^{2S+1}\Lambda^{+,-}_{g,u} \tag{6}$$

The ground state of a molecule is indicated by an X in front of the symbol (e.g. $X^1\Sigma_g^+$ for H_2). In general, higher levels are designated in order of increasing energy using capital letters (A,B,C...) when the state has the same spin as the ground state. Lower case letters (a,b,c...) are used when the state has a different spin. These rules are not followed as strictly for H_2 as the level labels were established early on and remained in place as the theory was developed (Sharp, 1970). Figure 1.4 shows the first several H_2 electronic energy levels.

1.4.3 Selection Rules

The fastest occurring transitions in molecules are dipole transitions. As was briefly discussed in §1.4.1, there are constraints on when dipole transitions can occur. These selection rules originate from a variety of sources, such as constraints imposed by the photon (e.g. photons are spin-0 bosons, so they cannot impact particle spins) or imposed by the relationship between the wavefunctions and the dipole moment (see Equation 3). Below is a list of the selection rules that are important to the transitions that will be discussed in this work. This is not a comprehensive list of all of the possible selection rules. For a more detailed description, see Herzberg (1950).

1. The molecule must have a dipole moment (permanent or induced)
2. ΔJ = 0, $\pm$ 1, (but J = 0 $\not\leftrightarrow$ 0; strictly)
3. Λ = 0, $\pm$ 1
4. ΔS = 0
5. $\Sigma^+ \leftrightarrow \Sigma^+$; $\Sigma^- \leftrightarrow \Sigma^-$; $\Sigma^+ \not\leftrightarrow \Sigma^-$ (holds when $\Lambda = 0$)
6. $g \leftrightarrow u$ (holds only for molecules with nuclei of equal charge)

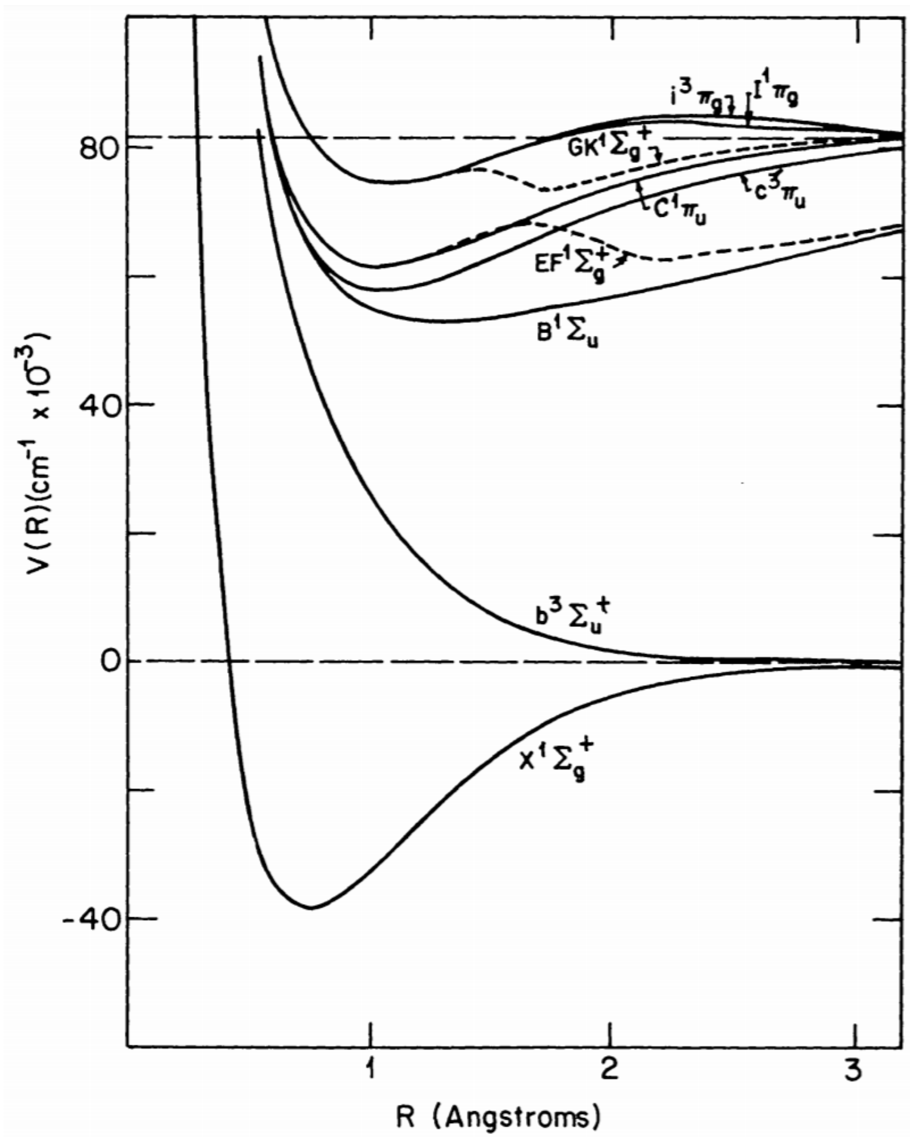

Figure 1.4: The seven lowest electronic energy levels in H_2, from Shull & Beckwith (1982). R is the internuclear separation and V is the total energy

7. ΔParity = (-1)$^{\lambda}$; where λ is the order of the monopole (λ = 1 for dipole)

For upper state (J$'$) and lower state (J$''$), the notation for a change in J is (from -2 to 2) O, P, Q, R, S, and is written in reference to the lower state. Note that "upper" and "lower" state refer to the entire state of the molecule and not just the rotational levels. For example, P(1) is a transition from J$'$ = 0 to J$''$ = 1 with ΔJ = J$'$- J$''$ = -1. The same notation is used for vibrational states (v$'$ for upper, v$''$ for lower) with a complete rovibration transition being written as (v$'$-v$''$) Q(J$''$). ΔJ = $\pm$ 2 has been included above because H_2 has a quadrupole moment and so quadrupole transitions (with ΔJ = 0, $\pm$ 1, $\pm$ 2) are allowed, but tend to be slow (rate of (0-0) S(0) $\sim 10^{-11}$ s^{-1}; Wolniewicz et al. 1998).

As discussed previously, in the ground state of H_2, all electric dipole transitions are forbidden for several reasons including the restriction that parity must flip. An important byproduct of this parity restriction comes from the fact that the nuclei in the H atom are identical fermions, which means that their total wavefunction must be anti-symmetric when their positions are interchanged. Their wavefunction is determined by the product of their spatial and spin wavefunctions, so one must always be symmetric and the other anti-symmetric. For ground state H_2, even J values form symmetric states and so the spins of the nuclei must be anti-symmetric, with total spin (I) = 0. This is known as para-H_2 and has a statistical weight of (2I + 1)(2J + 1) = (2J + 1). Odd J values form anti-symmetric states and so the spins of the nuclei must be symmetric, with I = 1. This is known as ortho-H_2 and it has a statistical weight of 3(2J + 1). In light of ΔJ $\neq$ 1 for ground state H_2, ortho- and para-H_2 cannot mix through rovibrational transitions, although interchange between the two is possible through other means that are important to this work (§1.6).

The first two electronic ground state transitions in H_2 from $X^1\Sigma_g^+$ are to the Lyman Band $B^1\Sigma_u^+$ (λ < 1120 Å) and Warner Band $C^1\Pi_u$ (λ < 1021 Å), with energies in the range of 11 to 14 eV. For $X^1\Sigma_g^+$ to $B^1\Sigma_u^+$, both states have $\Lambda = 0$. To maintain correct symmetries of the molecular wavefunction, ΔJ = 0 is forbidden and two branches of the transition are seen, R(J$''$) and P(J$''$). P(0) is not allowed because J $\geq$ 0. For $X^1\Sigma_g^+$ to $C^1\Pi_u$, the transition now involves a state with $\Lambda > 0$, which loosens the symmetry restrictions, allowing for a total of three branches Q(J″), R(J″), and P(J″). Because J is equal to the total angular momentum and $\Lambda = 1$, J cannot be less than one. This means Q(0), P(0), and P(1) transitions are not allowed (McCandliss, 2003).

1.5 Molecular Hydrogen Excitation Pathways

In a translucent cloud, there are several pathways H_2 can follow to reach an excited state. The dominant process will vary depending on the location of the H_2 molecule, with UV photon pumping and collisional excitation being common on the outer edge of the cloud and grain formation dominating closer to the core.

1.5.1 H_2 Ultraviolet Pumping and Absorption Features

Following sources like Draine (2011), we can derive the variables that describe the interactions between light and matter. Incoming UV photons can excite H_2 through dipole allowed transitions. The cross section of this interaction is given by:

$$\sigma_{\mathrm{lu}} = \frac{\sqrt{\pi}e^2}{m_e c b} f_{\mathrm{lu}} \lambda_{\mathrm{lu}} H(a, y) \qquad [\mathrm{cm}^2] \tag{7}$$

where b is the Doppler width, $H(a, y)$ is the Voigt function, which is used to describe the predicted shape of the absorption feature by accounting for both the broadening due to thermal motions of the molecules and the natural broadening that occurs as a result of the uncertainty principle. It is a function of the inverse lifetime of the upper state (Γ), with

$$a = \frac{\Gamma}{4\pi\Delta\nu} \tag{8}$$

$$y = \frac{|\nu - \nu_0|}{\Delta\nu} \tag{9}$$

$$\Delta\nu = \frac{b\nu}{c} \tag{10}$$

$f_{\rm lu}$ in Equation 7 is the oscillator strength of the transitions, which is related to the probability of a transition occurring. It is defined as:

$$f_{\rm lu} = \frac{m_e c}{8\pi^2 e^2}\frac{g_{\rm u}}{g_{\rm l}}\lambda_{\rm lu}^2 A_{\rm ul} \tag{11}$$

$A_{\rm ul}$ is the Einstein A coefficient of the transition. $g_{\rm u}$ and $g_{\rm l}$ are the degeneracies of the upper and lower states, respectively.

For UV pumping of H_2 that is observed in absorption, we describe a source with initial intensity $I_{\lambda,0}$ that is attenuated by H_2 along the line of sight to the observer. The subscript λ indicates a wavelength of interest. The final intensity (I_λ) that the observer sees is related to $I_{\lambda,0}$ through the optical depth (τ_λ) by:

$$I_\lambda = I_{\lambda,0}e^{-\tau_\lambda} + (1 - e^{-\tau_\lambda})S_\lambda \tag{12}$$

where S_λ is the source function for the cloud itself, which is assumed to be constant in this case. τ_λ is a dimensionless quantity that is related to the amount of interacting matter along a sight line of length ℓ, and is given by

$$\tau = \int_0^\ell \mathrm{n}\sigma_{\rm lu} dz = \sigma_{\rm lu}\int_0^\ell \mathrm{n} dz = \sigma_{\rm lu}\mathrm{N} \tag{13}$$

Where n is the number density of the species of interest and N is the column density, typically in units of cm^{-2}.

Historically, the column density was measured from an absorption spectrum by calculating the equivalent width (W) of different features and then constructing a curve of growth. Equivalent width is defined as

$$W_\lambda = \int_{-\infty}^{+\infty} \frac{I_{\lambda,0} - I_\lambda}{I_{\lambda,0}} d\lambda = \int_{-\infty}^{+\infty} (1 - e^{-\tau_\lambda}) d\lambda = \int_{-\infty}^{+\infty} (1 - e^{-\mathrm{N}\sigma_{\rm lu}}) d\lambda \tag{14}$$

The first equality in the above equation shows that equivalent width is a normalized measurement of the area within an absorption feature. It relates the size of the absorption line to the width of a rectangle with unit height. This measurement is particularly useful because it is a conserved quantity under convolution, meaning knowledge of the instrument profile is not necessary when performing the calculation.

The variation of W as a function of the dependent variables N, $f_{\rm lu}$ and λ is demonstrated in the curve of growth plot in Figure 1.5, where three specific regions of interest can be seen. For low values of N$f_{\rm lu}\lambda$, or equivalently $\tau_\lambda \ll 1$, W has a linear dependence on N$f_{\rm lu}\lambda$. This region is called the "linear" portion of the curve of growth. As τ_λ increases and becomes greater than 1, the Doppler broadening of the absorption feature becomes important and W $\propto b\sqrt{\ln(\mathrm{N}f_{\rm lu}\lambda/b)}$. This region is called the "flat" portion of the curve of growth. Finally, for very large τ_λ, the Doppler contribution to the curve of growth becomes saturated and growth of the line will depend on the natural broadening term. This region is called the "square root" portion of the curve of growth where W $\propto \sqrt{\mathrm{N}f_{\rm lu}\lambda}$.

Column densities for different J$''$ levels of H_2 can be derived by measuring the equivalent widths of several transitions involving the same J$''$ and then using their known $f_{\rm lu}$ and wavelengths, constructing a curve of growth to back out N and b. One difficulty associated with this method is the need to adequately sample the curve of growth to ensure the accuracy of the final results, particularly along the flat portion where N and b are highly degenerate (see, e.g. Wakker 2006). An alternative solution, and the one that is employed in this work, is directly fitting the lines using model H_2 absorption profiles (McCandliss, 2003) that account for b and N in their shape. This method requires a knowledge of the instrumental profile but can perform the measurement on a smaller number of absorption lines (see, e.g. Burgh et al. 2007; France et al. 2013). In this case, knowing where the observed lines fall on the curve of growth is still important, since the degeneracy between b and N will still exist. But, by simultaneously fitting lines on multiple parts of the curve of growth, this approach does give the most robust constraints on N and b.

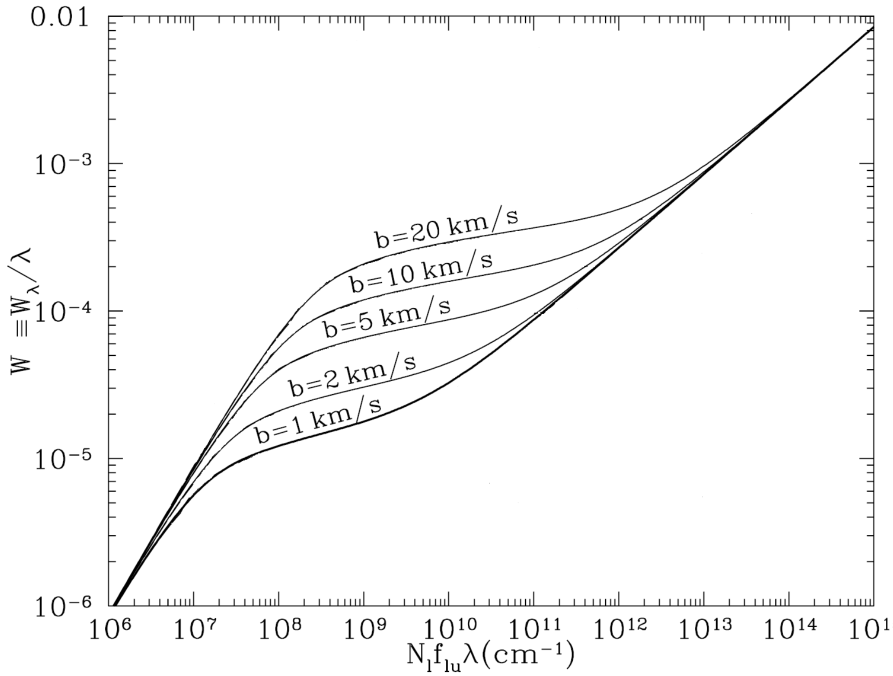

Figure 1.5: The curve of growth for a Lyα, from Draine (2011) with edits for clarity by N. Kruczek. Multiple curves are shown for different b values, demonstrating the sensitivity of W on b in the flat portion of the curve of growth. All five curves converge on similar results in the linear and square root limits.

1.5.2 Collisional Excitation

While the center of a translucent cloud will be cool ($\sim$50 K), the temperature will increase towards the edge of the cloud. Given the spacing of the lower rotational levels of H_2 (ΔT(J $= 2 \rightarrow 0) = 510$ K), rotational excitations from collisions can begin to become important at temperatures as low as 100 K (Le Bourlot et al., 1999).

If the temperature and density are large enough, such that collisions become the dominant reaction within the population of some species, the different energy levels will be driven into thermal equilibrium with one another. In that case, the relative populations between two different energy levels (x and y) are described by the Boltzmann equation:

$$\frac{\mathrm{N}_x}{\mathrm{N}_y} = \frac{g_y}{g_x} e^{(E_{xy}/kT)} \tag{15}$$

where g_x (g_y) is the degeneracy of the x (y) state, E_{xy} is the difference in energy between the two states, and T is the temperature of the gas.

Collisional excitation of H_2 provides an important source of cooling in transluncent clouds, since kinetic energy in the gas is converted to an energetically excited state. As the molecule de-excites, it will release a photon that can escape from the cloud carrying the energy with it. As will be discussed in §1.6, collisional excitation likely plays an important role in populating higher J'' levels of H_2.

1.5.3 Ejection After Grain Formation

Current predictions show that the dominant H_2 formation mechanism happens on dust grains. Following the review by Tielens & Allamandola (1987), the process of H_2 formation on grains starts with a free H atom colliding with a dust grain. The atom will adhere to the surface following a sticking probability that depends on the energy of the incoming atom and on the dust grain's ability to dissipate the impacting energy. The crystalline structure of dust grains leads to open chemical bonds that the H atoms can attach to. The H atom will migrate (through quantum tunneling) around the surface of the dust grain until it finds one of these chemical bonds or finds another H atom already in a chemical bond. In the latter case, there is a probability of the two atoms bonding and forming an H_2 molecule. The surface tunneling timescale is short ($\sim 10^{-9}$ sec) compared to the H_2 formation timescale ($\sim 10^{-6}$ sec), so any given H atom will migrate around several hundred times before forming the molecule but, in general, any H atom on the surface of the grain will eventually find itself in an H_2 molecule.

Once formed, the $\sim$4.5 eV energy released from the reaction will excite the H_2 molecule (Draine, 2011). In this electonically and rovibrationally excited state, the H_2 is able to be ejected from the surface of the dust grain if enough of its energy is transferred into a translational motion degree of freedom. There are other channels that the excess energy can be transferred to, such as into other rotational states in the H_2 molecule or into the dust crystal lattice, so ejection is not guaranteed. When it does occur, an excited H_2 molecule is sent into a cloud, acting as a source of heating (Black & Dalgarno, 1977). The distribution of the 4.5 eV of energy amongst the various degrees of freedom (kinetic, vibrational, rotational) within the molecule remains a poorly understood component of this process, with different models producing a range of results and driving larger uncertainties in the contribution of this effect to the overall heating (Takahashi et al., 1999; Meijer et al., 2001; Lacour et al., 2005).

1.6 Molecular Hydrogen De-excitation

Once excited through one of the previously described pathways, the H_2 fluoresces back down to the ground state. The amount of fluorescence through the various pathways is determined by the branching ratio:

$$r_{\text{branch}} = \frac{A_{\text{ul}}}{\Sigma A_{\text{ul}}} \tag{16}$$

If the de-excitation rate is faster than the photon arrival rate or any other excitation process, the H_2 molecule will ultimately end up in some rotationally excited state in the ground level. The distribution of populations in the ground state can be observed in absorption in the FUV, which is done in this work as well as many of the citations within it. From the column densities extracted using these techniques, an excitation diagram is made detailing the energetics of the environment the H_2 resides in.

Example excitation diagrams are shown in Figure 1.6. Two distinct populations of H_2 can be seen. The low J$''$ states are well described by a low temperature thermal distribution, the higher J$''$ states are described by a high temperature (T_{exc}) distribution, and a transition between the states is generally seen around J$'' = 2$ and 3.

In clouds that are suitably self-shielded (N(J $= 0$) and N(J $= 1$) $> 10^{17}$ cm^{-2}; Savage et al. 1977), the lack of available radiation leads to H_2 relaxing down to the J $= 0$ and 1 states. Given that transitions between para-H_2 (J $= 0$) and ortho-H_2 (J $= 1$) are radiativley and collisionally forbidden in the ground state of H_2 (§1.4.3), observing the two species

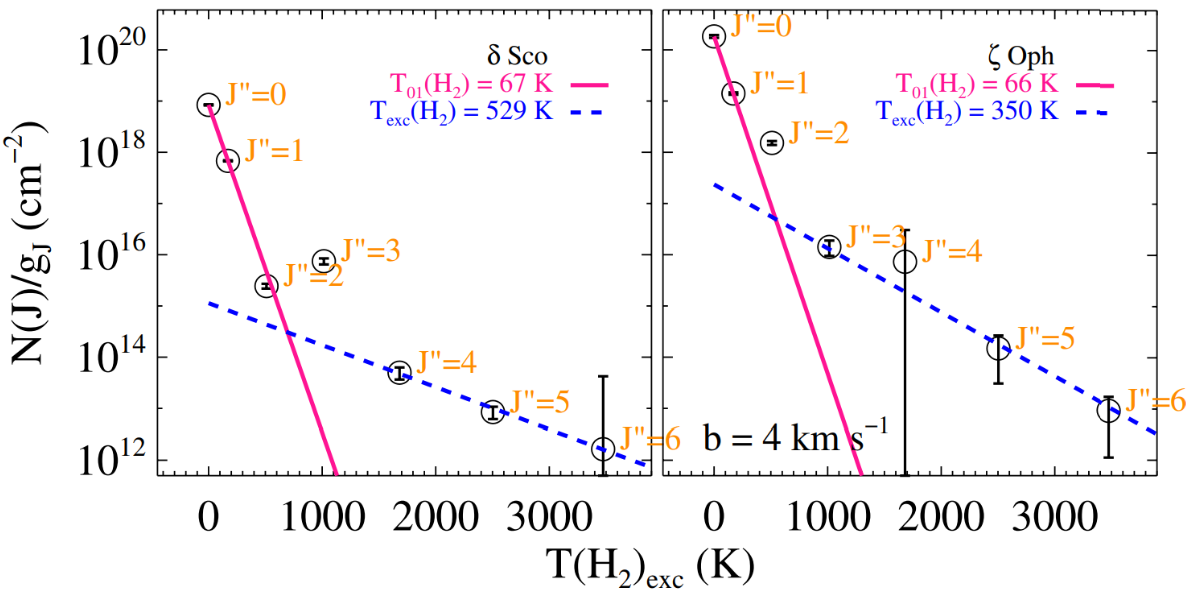

Figure 1.6: Two example excitation diagrams measured using data from the Suborbital Local Interstellar Cloud Experiment (SLICE) sounding rocket, taken from France et al. (2013). The pink lines show the low kinetic temperature of the gas that describes the low J″ level populations. The blue dashed line shows the high excitation temperature that describes the high J″ level populations.

in a thermally populated equilibrium is, on the surface, an unexpected result. Dalgarno et al. (1973) demonstrates that one solution to this problem comes from free protons (H^+) existing within the cloud. These protons are generated by high energy photons (UV–X-ray) and cosmic rays. They collide with the H_2 molecules initiating a proton interchange reaction:

$$H^+ + \text{ortho}-H_2 \leftrightarrow \text{para}-H_2 + H^+ \tag{17}$$

The free proton fully replaces one of the existing H_2 nuclei, generating an effectively new molecule and bypassing the spin-flip restrictions of other transitions. When this collision is the dominant reaction, a thermal distribution of the $J'' = 0$ and 1 (and sometimes 2) states is generated, described by the thermal energy of the free protons. This value is typically used as a measurement of the gas kinetic temperature (T_{01}), which can be calculated from the observed column densities of the lowest two states ($N(J'' = 0)$ and $N(J'' = 1)$) using Equation 15. Previous FUV measurements have found an average T_{01} in the range of 70–80

K (Savage et al., 1977; Rachford et al., 2002; Burgh et al., 2007; Sheffer et al., 2008; Rachford et al., 2009) for sightlines in the diffuse to translucent density range. The temperature for the proton interchange reaction is 170.5 K. At the temperatures of these clouds, this will mean that $J = 1 \rightarrow 0$ will be the dominant conversion and will act as a source of heating (Dalgarno et al., 1973).

While it was originally thought that UV pumping, from the host star if it is close enough or from the average interstellar radiation field, was the driver of the observed high J'' thermal distribution (see, e.g. Stecher & Williams 1967), continued work on the subject has called into question this assumption. Black & Dalgarno (1976) showed that H_2 ejected from dust grains was more efficient than UV pumping at populating high J'' levels. This conclusion was extended by Wagenblast (1992), who demonstrated that the ratio of column densities for the high J'' states (J'' = 4–7) should generally be fixed, within the para- to ortho-H_2 ratio of the cloud, when UV pumping was the primary driver of the excitation. The author showed that the measurements along three sightlines disagreed with this predicted result, indicating UV pumping was not responsible for maintaining the high J'' populations. He further showed that H_2 formation or collisions of H_2 molecules that were heated by a recent event, such as a passing shock front, provided adequate descriptions of the observed distributions.

While the explanation of H_2 formation on grains was the favored explanation, more recent evidence suggests that it too fails to account for the observed high J'' populations along an increasing number of sightlines. Gry et al. (2002); Sonnentrucker et al. (2003); and Lacour et al. (2005) use *FUSE* observations to measure the column densities of H_2 for several different lines of sight and all find that their column densities are best described by collisional excitation of warm H_2. This population could be generated by small-scale shocks or turbulent vortices resulting from ions interacting with the neutral medium. The population could be in the form of a shell around the denser cloud center or it could be more widely distributed along the sightline (Rachford et al., 2002; Lacour et al., 2005). Jensen et al. (2010) suggests a possible test for constraining the location of the warm H_2 by measuring the b-values and velocity offsets of the different J$''$ levels, but ultimately find that their conclusions are limited by the resolution of the *FUSE* instrument, motivating the need for a modern, high-resolution, replacement FUV observatory disentangle this problem.

1.7 History of FUV Missions

Similar to the previously discussed results from the *FUSE* instrument, we can trace a number of important ISM discoveries by following the development of space-based UV instruments, since each iteration introduced new, more powerful optics and electronics that revealed previously unseen details. Understanding the roles of each of these instruments also helps motivate future designs, which can utilize new technologies to surpass the limitations of their predecessors. We provide an overview of the most prominent of these missions here, with particular attention paid to three missions that were important motivators for the CHESS sounding rocket - *Copernicus*, IMAPS, and *FUSE*. We also provide example ISM results obtained through the use of each instrument, but note that they do constitute and exhaustive list of each instruments accomplishments.

1.7.1 High Resolution and UV Spectroscopy

To better express the motivations of these different instruments, a basic understanding of UV spectroscopy is necessary. Spectroscopy uses dispersing elements, like gratings, to separate incident light as a function of wavelength, as dictated by the grating equation:

$$\frac{m\lambda}{d} = [\sin(\alpha) + \sin(\beta)]\cos(\gamma) \tag{18}$$

Where m is the order, d is the groove spacing, α is the angle of incidence, β is the diffraction angle, and γ is the tilt of the grating in the direction perpendicular to the dispersion.

The performance of a grating is described using two parameters, groove efficiency and resolution. Groove efficiency is the ratio of the intensity of diffracted on-order light to the total intensity. Effects such as scatter off of the grating surface can decrease the groove efficiency. The resolution of a grating ($\Delta\lambda$) is a description of the smallest wavelength separation that can be distinguished when dispersed by a grating. This is frequently described using the unitless resolving power (R), which is defined as:

$$\mathrm{R} = \frac{\lambda}{\Delta\lambda} = \frac{m\mathrm{W}}{d} \tag{19}$$

Where W is the width of the illuminated portion of the grating. For high resolution studies of the ISM, where the goal is to resolve kinematics and individual cloud components, a velocity resolution on the order of 3 km s^{-1} is necessary, which is equivalent to R = 100,000 (Jenkins & Tripp, 2001).

An echelle is a particular grating design that is optimized to achieve a large resolution by operating in a high dispersion configuration. If we take the derivative of Equation 18 with respect to λ (and assume α is constant), the angular dispersion of a grating is found to be:

$$\frac{d\beta}{d\lambda} = \frac{m}{d\,\cos(\beta)\cos(\gamma)} = \frac{[\sin(\alpha) + \sin(\beta)]\cos(\gamma)}{\lambda\,\cos(\beta)} \tag{20}$$

Where, in the final step, the grating equation was substituted in for $\frac{m}{d}$. From this equation, we see that operating at high angles of incidence and diffraction ($\alpha = \beta \rightarrow 90°$) produces a larger angular dispersion as a function of wavelength (Palmer & Loewen, 2005). A higher angular dispersion means that two wavelengths will have a larger physical separation, making them easier to resolve.

This relationship is utilized in echelles to produce high resolution spectra. A couple considerations must be made when designing a grating of this type. First, orders in the grating equation can be positive or negative, with two different angles of diffraction. To direct light into the order of interest, a blazed groove profile is used. This profile is commonly implemented as a sawtooth pattern, with one steep side that has a large angle relative to the plane of the grating (referred to as the blaze angle, θ_{b}) and one shallower side. To properly

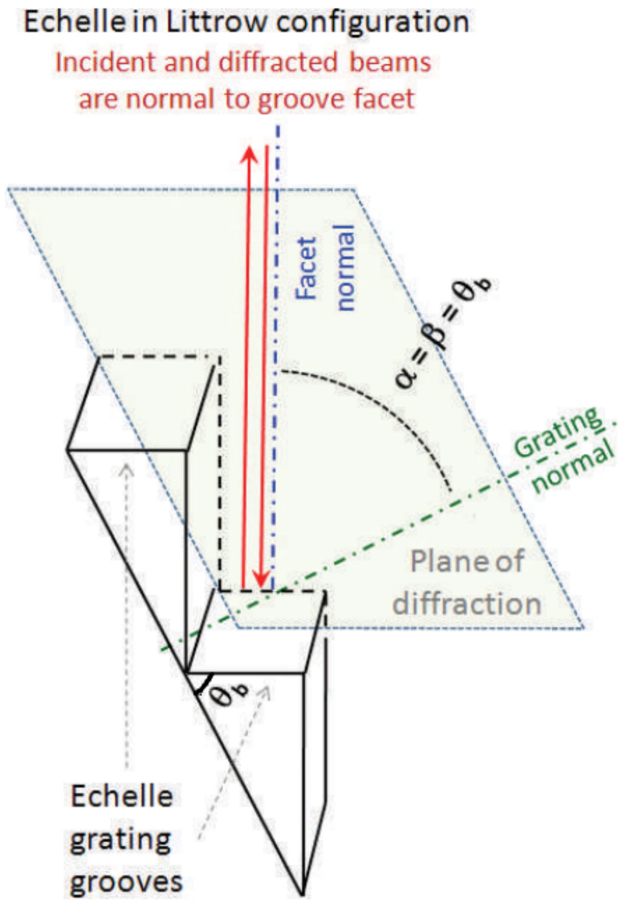

Figure 1.7: A close up image of an echelle grating operating in Littrow configuration. Image is from Bykov et al. (2013), with modifications by N. Kruczek. If the grating were to operate out of Littrow in either direction the efficiency would decrease.

illuminate the grating facet, the echelle is operated in Littrow configuration where $\alpha = \beta = \theta_{\rm b}$. This is visualized in Figure 1.7. To prevent overlap between the incoming and outgoing beams, the echelle is tilted at a small γ.

We see in Equation 20 that, to achieve the large $\frac{d\beta}{d\lambda}$, the grating will need to operate in either a high order or have a short groove spacing. The differences between the two arise from the free spectral range (FSR) which, for a given order, is the wavelength interval that is not contaminated by light from neighboring orders. Specifically, following the derivation of Palmer & Loewen (2005), light with wavelength $\lambda + \Delta\lambda$ in order m will have the same angle of diffraction as light with wavelength λ in order m+1. By equating Equation 18 for the two wavelengths, we find:

$$\Delta\lambda = \lambda\Big(\frac{m+1}{m} - 1\Big) = \frac{\lambda}{m} \tag{21}$$

Where $\Delta\lambda$ here is the FSR. We see that, for higher orders (longer groove spacings), there will be a smaller FSR. In that case, a method for further separating the spectrum is necessary to avoid overlapping orders. The solution to this is to use a second grating, called a cross disperser, that separates light in the perpendicular direction. For lower orders (shorter groove separations), the FSR is longer and so a cross disperser may not necessarily be needed. The trade off is that the orders are physically longer, since they contain more unique wavelength space. This requires a larger detector to capture the entire spectrum or the spectrum needs to be reimaged. Given the size constraints of detectors and difficulty associated with fabricating high groove density gratings, the high order echelle with a cross dispersing grating is the design that has typically seen use.

The difficultly associated with working in the FUV comes from the lack of highly reflective materials (Hass, 1955). The optimal surface material for FUV optics is bare aluminum (Al) but it readily oxidizes and that oxidation layer severely degrades its performance. The reflectivities, or ratio of reflected intensity to total intensity, of bare and oxidized Al are show in Figure 1.8, for reference. To mitigate this issue, a thin protective overcoat is applied to the surface of the aluminum soon after coating, reducing the amount of oxidation that occurs.

Two common protective materials are lithium fluoride (LiF) and magnesium fluoride (MgF_2). The choice of material is strongly motivated by the bandpasses they support. LiF maintains good reflectivity down to $\lambda \sim 1000$ Å, but has the drawback of degrading in the presence of water and so great care must be taken in handling the coatings outside of dry or high vacuum environments (Angel et al., 1961; Fleming et al., 2017). MgF_2 has a longer wavelength cutoff at 1150 Å, meaning it cannot observe the Lyman and Werner H_2

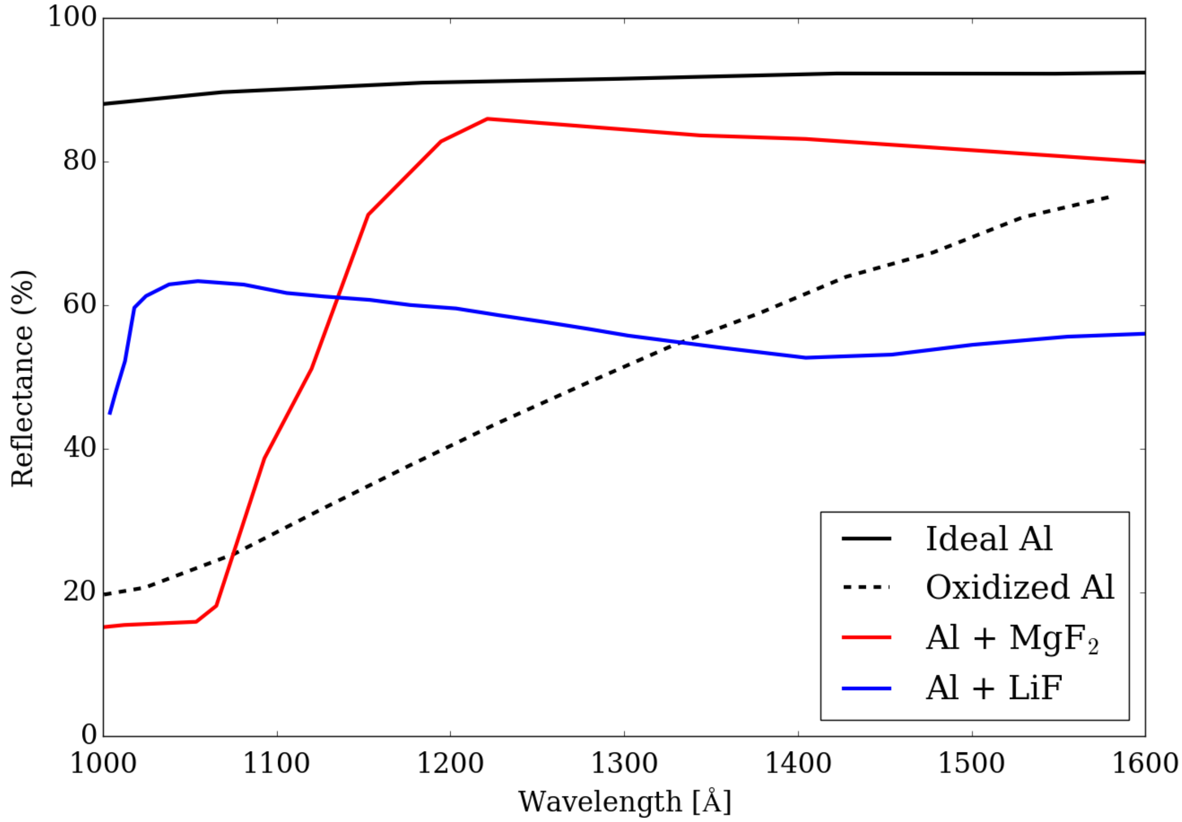

Figure 1.8: Example FUV reflectance curves for different coatings. The values for ideal and oxidized Al were taken from Hennessy et al. (2017, 2018). The values for Al+MgF_2 and Al+LiF were taken from Fleming et al. (2017).

absorption features, but it has higher reflectivty than LiF at longer wavelengths (Figure 1.8) and is less sensitive to moisture.

It is important to remember that the reflectivities presented in Figure 1.8 represent reflection off a flat surface. In the case of gratings, the final efficiency is a product of this reflectivity and the groove efficiency, leading to lower efficiencies overall. Given the significant losses inherent to the UV bandpass, it is advantageous to reduce the number of reflections in the instrument as much as possible. The trade-off to this is that additional optics provide additional opportunities to disperse the light or remove aberrations in the resulting spectrum. As will be shown in the sections below, instrument design at this bandpass is driven by the balance between these two limitations.

Channel	Carriage	Exit Slit [μm]	Resolution[a]	Bandpass [Å]
U1	1	23	11,000	710–1500
V1	1	24	24,000	1640–3185
U2	2	98	3,000	750–1645
V2	2	96	6,000	1480–3275

[a] Approximate R, taken at the center of the bandpass.

Table 4: Summary of *Copernicus* channels

1.7.2 Far Ultraviolet Spectroscopy Missions

One solution to reducing the number of reflections in a UV instrument is to use a grating with a curved surface, allowing for the simultaneous focusing and dispersing of incident light. The most basic form of this uses a cylindrical concave grating as the diffractive optic, with the grooves running perpendicular to the curvature. A circle with its diameter equal to the radius of curvature of this grating is known as the Rowland circle. It has the property that, if a point source and the grating are located on the circle, the grating will disperse and refocus the point source to another position on the circle. A spectrograph in this configuration is known as a Rowland circle spectrograph.

The UV spectrometer on the *Copernicus* satellite utilized a Rowland circle design. The satellite housed two experiments, a Princeton-built UV spectrometer and an X-ray experiment (NASA, 2003). For clarity, when we refer to *Copernicus*, we are referencing the UV spectrometer. The Rowland circle spectrometer was fed by an f/20 Cassegrain. To capture the image, *Copernicus* had two motor carriages that each held two exit slits in front of phototubes, which use a photocathode to convert photons into electrons that are attracted to, and subsequently detected by, an anode. The four detectors were split into two bandpasses, designated by U and V and two exit slit widths, or equivalently two resolutions, designated by a 1 or a 2 (Rogerson et al., 1973). A summary of each of the four channels is provided in Table 4.

Launching in 1972, *Copernicus* produced the first ever large (n = 109) survey of molecular H_2, using the U1 and U2 channels to record the FUV absorption features (Savage et al., 1977).

Using these data, the authors measured, or obtained upper limits on, the column densities of H_2 in the $v'' = 0$, $J'' = 0$ and 1 levels. They calculated, among other values, an average T_{01} of 77 ± 17 K, a number that has seen continued use as the point of comparison when measuring the average kinetic temperature of the diffuse/translucent ISM (Rachford et al., 2002; Burgh et al., 2007; Sheffer et al., 2008). The instrument also provided the most recent FUV observations at $\lambda < 1150$ Å of the CHESS-3 and CHESS-4 targets and so we use it as a point of a comparison for our results (§3).

The *International Ultraviolet Explorer* (*IUE*) launched in 1978. This was a dual channel spectrograph, with the two channels covering different bandpasses (1150–1950 and 1900–3200 Å). Both channels had similar designs, so we will focus on the short wavelength version. The optical path within a channel had two configurations, a high and low resolution. The high resolution channel was an echelle spectrograph and it achieved resolving powers ranging from R = 11,000–13,500. The optical path consisted of an f/15 Cassegrain that fed a collimating off-axis paraboloid mirror. The collimated beam was directed at the echelle followed by a spherically-curved grating that provided the cross dispersion. The five bounce optical path likely ruled out the use of LiF as the protective coating, and so MgF_2 was used and it set the short wavelength end of the bandpass. The basic form of the detector was a television camera that was sensitive to visible light. To convert the UV light to visible, an MgF_2 window with a CsTe photocathode generated photoelectrons from the incident light. A phosphor screen was used to amplify the resulting signal and convert the electrons into visible photons that were passed to the camera through fiber optics (Boggess et al., 1978). Compared to *Copernicus*, *IUE* provided a more uniform coverage of longer wavelengths, making it useful for follow-up observations of depletions and non-H_2 molecules (Grewing et al., 1978; Cardelli & Boehm-Vitense, 1982).

The next major mission to begin operations was the Hopkins Ultraviolet Telescope (HUT) aboard the *ASTRO* Observatory. This instrument was apart of both flights of the shuttle mounted observatory, the first mission lasting from Dec. 2–10 1990 and the second from

Mar. 3–17 1995 (NASA, 2013). The instrument itself consisted of only two bounces, an f/2 primary mirror focused light into a Rowland circle spectrograph, with the entrance slit, f/2 spherical concave grating and detector all in fixed positions. The detector was an array of 1024 Si diodes, which produced an internal current when impacted by electrons. This diode array was fed by a stack of two microchannel plates (MCP), which are glass plates containing an array of small pores. The chemical composition of the glass makes it an electron multiplier. The top of the MCP stack is coated with a photocathode, CsI in this case, which converts the incoming light into an electron. A voltage is applied vertically down the plates so that the photoelectron is accelerated down the pores through the plate, impacting the walls as it goes, and ultimately generating a cloud of electrons at the exit of the MCP stack. This much larger signal allows for photon-counting observations of UV sources. The low number of reflections and unique coating selections (iridium and osmium) gave *HUT* an impressive bandpass, spanning from 850–1850 Å, but the simple design could only achieve R $<$ 1000 (Davidsen & Fountain, 1985; Davidsen et al., 1992). While this low resolution meant that the primary science goals of *HUT* were not ISM-related, observations helped in measuring the dust and HI extinction in the Milky Way (Buss et al., 1994).

Following the end of the *Copernicus* satellite, the Interstellar Medium Absorption Profile Spectrograph (IMAPS) sounding rocket continued the thread of FUV observations at wavelengths below 1150 Å. The instrument flew three times between 1984 and 1988, with the most prominent being their second flight in which they obtained R = 150,000 observations of π Sco (Jenkins et al., 1996). The success of the instrument led to it being included on two launches of the *ORFEUS-SPAS* mission, another short duration observatory like *ASTRO*, in 1993 and 1996. IMAPS was an echelle spectograph with a parabolic cross dispersing grating. The major difference between it and *IUE* was that IMAPS utilized two bounces, compared to the five in *IUE*. This was accomplished by replacing the two telescope optics and collimating mirror with a single "mechanical collimator", which used a series of mesh wire grids to restrict the field of view to a 1° circle. The collimator throughput was still

$\sim$60%, so they effectively eliminated the losses associated with two of the three optics they removed. The trade-off was that the collecting area of the collimator was limited to the size of the echelle (200 cm^2), so they did not benefit from the larger collecting area provided by a telescope (Jenkins et al., 1988, 1996).

The optical path of IMAPS can be seen in Figure 1.9 and has been included because it was the basis for the design of the CHESS instrument. Both of its optics were coated with Al and a LiF protective layer. The bandpass of the ORFEUS-SPAS version of the instrument spanned 950–1150 Å at a velocity resolution on the order of 4 km s^{-1}. The IMAPS detector was designed around a permanent magnet-based focusing system. Incoming light would impact a KBr photocathode plate. The resulting electrons would be accelerated by an applied potential and perform a single gyration about the B field, focusing them onto a back-side illuminated charge-coupled device (CCD). CCDs use an array of electrodes to define pixels across a silicon substrate. When, in this case, an electron impacts the silicon it creates numerous electron-hole pairs that subsequently separate due to the applied voltage from the electrodes. The resulting signal is read-out by a clocking of the electrode potentials, effectively passing the charge horizontally pixel-by-pixel, eventually reaching final pixel column, which is read-out vertically (Lumb et al., 1991).

The entire spectrum fit on the detector in the cross dispersion direction. It did not fit in the echelle dispersion direction and so four exposures were needed at different echelle angles to construct a complete image (Jenkins et al., 1996). Observations presented by Jenkins & Peimbert (1997) reignited interest in a phenomena first seen in *Copernicus* data (Spitzer & Cochran, 1973; Spitzer et al., 1974), where H_2 lines were broadened as a function of J$''$ level. The authors cited shocks as a possible source for the excitation, yet subsequent observations along nearby sightlines did not show the same effect (Jenkins et al., 2000). Understanding this effect is still an on-going topic of study and it plays an import role in theories related to the origin of high J$''$ levels (§1.6).

The 1990's also saw the launch of the *Hubble Space Telescope* (*HST*) which has served

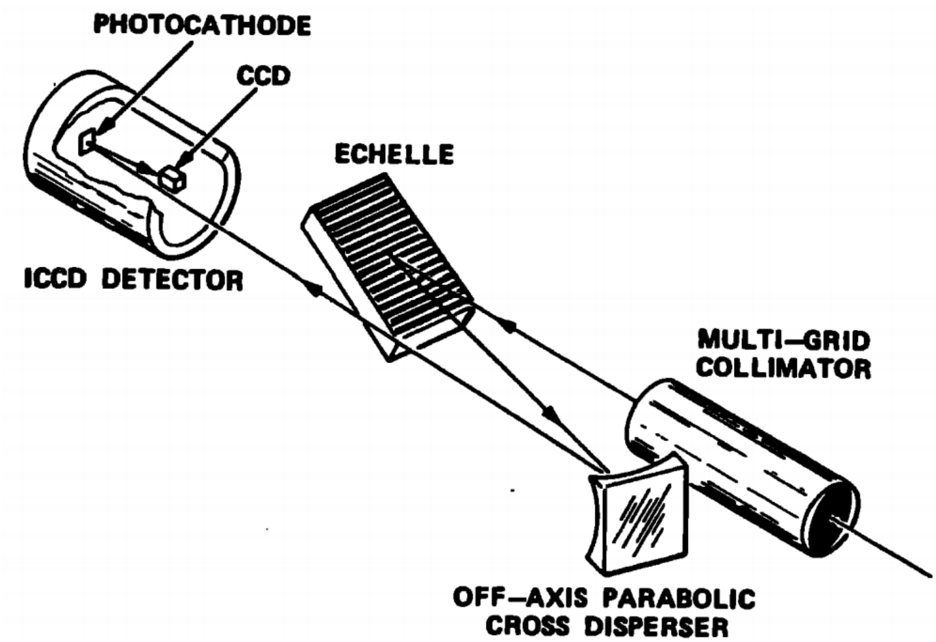

Figure 1.9: From Jenkins et al. (1996), the optical path of the IMAPS instrument.

as the observing platform for three UV spectrographs. *HST* itself is an f/24 Cassegrain telescope, both mirrors are coated with MgF_2 (STSCI, 2017). One of its first instruments, the Goddard High Resolution Spectrograph (GHRS), was an FUV spectrograph that was in operation from 1990–1997. It contained seven different spectroscopic modes ranging from a low resolution first order grating mode (R $\sim$ 2,000) to two high resolution echelle grating modes (R $\sim$ 85,000) and had a bandpass of 1130–2100 Å. It used two detectors that were identical in design except for the bandpasses over which they were optimized. Each consisted of an array of 512 (50 x 400 μm) individual diodes, 500 of which were used for science. A CsI photocathode deposited onto a LiF window set the bandpass for the first detector. The second used a CsTe photocathode on a MgF_2 window. In both cases, the electrons produced by the photocathode are focused onto the detector using a set of permanent magnets (Brandt et al., 1994). The single strip of diodes meant that only one echelle order could be observed at a time and so obtaining full coverage of the bandpass was a time consuming endeavor.

GHRS operated through the installation of the Corrective Optics Space Telescope Axial Replacement (COSTAR), the two optic extension to the *HST* optical path that corrected for a fabrication error in the primary mirror (Crocker, 1993). Science results were obtainable in the pre- and post-COSTAR configurations, but they were both limited by different throughput constraints (Heap et al., 1995; Robinson et al., 1998). Given the larger number of bounces and MgF_2 coatings, GHRS served as a successor to *IUE* when it came to studying the ISM, providing line of sight measurements of metal abundances and CO (see, e.g. Cardelli et al. 1991; Smith et al. 1991; Savage & Sembach 1996).

In 1997, STIS was installed in part as a replacement for GHRS. It provides a broadband imaging camera and an array of 16 gratings designed for spectroscopy and spectral imaging at a variety of wavelength ranges, spanning 1150–10,000 Å. The peak resolution of the instrument occurs in the FUV echelle mode, which achieves R = 114,000 (Woodgate et al., 1998). The FUV detector is a Multianode Microchannel Array (MAMA), which uses an MgF_2 window and a curved single plate CsI-coated MCP to define the bandpass and intensify the signal. The MCP illuminates an array of anodes that are laid out in a specific pattern such that different charge ratios are read out from different anodes, depending on the location of the electron cloud. An anode array of this type is better at handling higher count rates, but that comes at the expense of spatial resolution on the detector (Timothy & Bybee, 1986). The primary science results, as they relate to this work, were the previously discussed observations of N(CO) along sightlines with measured N(H_2) (§1.6).

The versatility of STIS also came with a more complicated optical path, having no fewer than six bounces in any mode. This means that the efficiency of STIS was limited and it cannot observe fainter targets of interest. The Cosmic Origins Spectrograph (COS) was proposed as a complementary instrument to STIS, with the goal of achieving high efficiency at moderate resolutions to greatly increase the number of faint objects that could be observed. Like HUT and IMAPS, this sensitivity was gained by reducing the number of reflections in the optical path. The COS team utilized developments in grating manufacturing to create low-scatter gratings that simultaneously focused and corrected for aberrations in the *HST* beam. Using these techniques, they designed an instrument with three FUV modes, all of which required only a single optic. The total FUV bandpass was designed to be 1150–1775 Å, but in-flight testing revealed that signal is attainable down to $\lambda \sim 920$ Å (McCandliss et al., 2010). The primary observing mode achieves R = 20,000. The detector was again a CsI-coated MCP, utilizing three plates and a delay line anode, which is made from long conductive strips that determine position by differencing the arrival time of the signal on either end of the anode. This means the detector does not have physical pixels, which helps improve the spatial resolution of the instrument, but it is unable to handle as large of count rates when compared to MAMA detectors (McPhate et al., 2000; Vallerga et al., 2001; Green et al., 2012). COS was deployed in 2009 with the primary science goal of gaining a better understanding of the mass distribution on cosmological scales by measuring absorption lines along quasar sightlines. The high sensitivity also allowed it to observe ISM absorption features along highly reddened sightlines, measuring depletions and the column density of CO at the upper edge of the translucent cloud regime (Snow et al., 2010).

The *FUSE* satellite launched in 1999 as a successor to the *Copernicus* satellite, with the goal of achieving higher sensitivity and velocity resolution that was at least as good, if not better, over a similar bandpass. It utilized four coaligned prime focus telescopes, made from off-axis parabolas, that each directed light into their own Rowland circle spectrograph that contained an aberration-correcting grating (Moos et al., 2000). The motivation behind the array of four telescopes was that a single large primary mirror would need to have a fairly small f-number (f/2 in the case of HUT) to avoid having an instrument that is too long, but that low f-number would have resulted in larger aberrations. By dividing the single mirror into several separate ones, a smaller beam is produced by each one and so they can all be slower, with reduced aberrations, while covering a comparable collecting area (Hurwitz & Bowyer, 1986). The optics in all four channels were identical, but two of them used Al+LiF coatings for a bandpass of ∼1000–1187 Å and two used silicon carbide (SiC) for a bandpass of 905–1105 Å. *FUSE* used two KBr-coated delay line MCP detectors. Each one was illuminated by a LiF channel and a SiC channel, running parallel to one another. To make the detectors large enough, a single detector was actually made from two 88 mm segments, separated by a 10 mm gap, and curved to roughly match the Rowland circle (McPhate et al., 2000). Each grating assembly had three different entrance apertures that could be selected by adjusting the telescope pointing (Moos et al., 2000).

Preliminary measurements of the in-flight velocity resolutions produced values around 20 km s^{-1}, which was further reduced to $\sim$13 km s^{-1} for the LiF channels using the highest resolution entrance aperture. *FUSE* was designed to observe faint objects. The target brightness limit was determined by what would maximize the lifetime of the detectors, which could lose sensitivity if they were subjected to large photon rates. In light of this, *FUSE* and *Copernicus* had few overlapping targets and *FUSE* was able to observe a large number of sightlines that were not previously accessible beyond the limited work of short duration missions (Sahnow et al., 2000). This resulted in several surveys of H_2 column densities in the ISM along a variety of lines of sight, including ones potentially containing translucent clouds (Rachford et al., 2009), at high galactic latitudes (Wakker, 2006; Gillmon et al., 2006), and in the large and small Magellenic clouds (Tumlinson et al., 2002).

FUSE remained operational until 2007 and since then there have been no space-based observatories (and none under construction) that are optimized for observations at $\lambda < 1150$ Å. Instead, sounding rocket missions have continued the work. The precursor to the CHESS instrument was the Sub-orbital Local Interstellar Cloud Experiment (SLICE) sounding rocket, which launched in 2013. It had a small 20 cm f/7 Cassegrain telescope that fed a Rowland circle spectrograph that matched the f/7 of the telescope (Kane et al., 2013). It was optimized for a bandpass of 1020–1070 Å at a detector limited resolving power of R = 5,300. The SLICE detector was a RbBr-coated MCP that utilized a total of five plates. The electron cloud illuminated a single anode that could read out charge at each of its corners. The position of the cloud was determined by comparing the amount of charge collected at each corner Kane et al. (2013). During the flight of SLICE, it observed four different targets and was able to obtain measurements of the H_2 column density up to $J'' = 7$ for two of them

(δ Sco and ζ Oph, Figure 1.6). The lower resolution of the payload meant that it was not able to separate out individual velocity components of clouds along the line of sight (France et al., 2013).

When combined, the FUV coverage, sensitivity, and resolution of these instruments is impressive and essentially comprehensive. But, more recently, there has been a gap in the high efficiency, high resolution, and short wavelength parameter space that has not been met since the observations performed by IMAPS in 1996. Since that time, observations have identified a number of interesting sightlines that would benefit from additional high resolution FUV observations. This need led to the creation the CHESS instrument, an IMAPS-motivated design that utilizes state-of-the-art grating fabrication techniques and detector technologies to obtain high resolution spectra of bright targets over a broad FUV bandpass. It further simultaneously covers the full range of H_2 and C absorption features, probing all of the key FUV diagnostics of diffuse and translucent clouds in a single observation.

The goal of the CHESS instrument is to contribute to these past data sets by providing new observations of H_2 along sightlines towards bright stars. While the resolution and S/N of the CHESS instrument was lower than designed, limiting the achievable science related to CO and depletion patterns, we are able to construct excitation diagrams along two sightlines that were last observed at $\lambda < 1150$ Å in the mid-1970's. As will be shown shortly, the work has motivated a re-examination of the methods used to calculate T_{01} and has produced column density measurements up to $J'' = 7$, potentially providing additional points of comparison for models working towards understanding the origin of the high J'' excitation.

2 Colorado High-resolution Echelle Stellar Spectrograph

CHESS is a rocket-borne astronomical instrument that first launched from White Sands Missile Range (WSMR) aboard NASA/CU mission 36.285 (CHESS-1) on May 24$^{\text{th}}$ 2014 and has since completed three additional launches: 36.297 UG (CHESS-2) on February, 21$^{\rm st}$ 2016, 36.323 UG (CHESS-3) on June 26$^{\rm th}$, 2017, and 36.333 UG (CHESS-4) on April 17$^{\rm th}$, 2018 (Beasley et al., 2010; Hoadley et al., 2014, 2016; France et al., 2016; Kruczek et al., 2017, 2018). This section will present information on the CHESS targets, instrument optics, alignment, calibration, and analysis of the flight spectra, with particular focus on CHESS-3 and CHESS-4.

2.1 Targets

The CHESS experiment is designed to study translucent clouds by utilizing a combination of bandpass and spectral resolution that was not achievable by past and present space-based observatories. The bandpass of the instrument ($\lambda\lambda$ 1000–1600 Å) contains absorption lines of H_2 (1000–1120 Å), C II (1036 and 1335 Å; however we note that saturation effects can complicate the interpretation of these lines), C I (several between 1103–1130, 1261, 1561 Å), and the A$-$X, B$-$X, C$-$X, and E$-$X bands of CO ($<$ 1550 Å). High resolution (R $>$ 100,000) is required to resolve the velocity structure of the C I lines and the rotational structure of CO. High resolution is therefore essential to the accurate determination of the column density of these species (Jenkins & Tripp, 2001). By choosing sightlines with intermediate H_2 column densities (10^{19}–10^{20} cm^{-2}), the transition from a neutral-to-molecular fraction of the available carbon can be examined. The bandpass also provides access to many absorption lines of metals, such as Fe, Mg, Si, and Ni, allowing for an exploration of the depletion patterns in translucent clouds. CHESS, with its designed high-resolution and large bandpass, including wavelengths shorter than 1150 Å, is well-suited to study diffuse and translucent clouds and to help create an observational base for models of the chemistry and physical conditions in interstellar clouds. While a fabrication error in the cross dispersing optic (§2.3.2) limited the science we were able to achieve with the instrument, we were ultimately able to reexamine the H_2 content along three lines of sight that were last observed at $<$ 1150 Å by the *Copernicus* satellite.

Flight	Target	Spectral Type	d [pc]	E(B-V)	$\log_{10}$N(H_2) [$\log_{10}$ cm^2]
CHESS-1	α Virginis	B1 IV	86	0.03	12.95
CHESS-2	λ Orionis	O8 III	530	0.12	19.11
CHESS-3	β^1 Scorpii	B0.5 V	161	0.20	19.83
CHESS-4	γ Arae	B1 I	689	0.08	19.24

Note: All values from Savage et al. (1977)

Table 5: CHESS targets

Table 5 lists the targets that were observed during each of the four CHESS missions. Due to the low efficiency of an experimental echelle grating used on CHESS-1 (§2.3.1), science results were not obtained (Hoadley et al., 2014). This issue was corrected for CHESS-2, resulting in a measurement of N(H_2) as well as a characterization of the depletion patterns along the sightline towards λ Orionis (Hoadley et al., 2016, 2019).

The target for CHESS-3 was β^1 Scorpii (β Sco), a B0.5 V star at d = 161 pc with intermediate reddening (E(B-V) = 0.20, Av $\sim$ 0.6) (Savage et al., 1977; Abt, 1981), indicating that the sightline may be sampling translucent material. H_2, C I, and CO were all detected by *Copernicus* along the line of sight to β Sco, however observations with higher sensitivity and spectral resolution were needed to understand the structure of the intervening matter (Federman et al., 1980). Additional studies found depletion of molecular material and ionized metal features, such as CO, Fe II, and Mg II, a result that is inconsistent with some nearby sightlines, such as ζ Oph and ρ Oph (Bohlin et al., 1983). This star was the original target for CHESS-1, but the decision was made to switch to α Virginis due to the in-flight count rate for β Sco being too low. We subsequently installed a higher efficiency echelle and successfully observed the sightline.

The fourth flight of CHESS observed γ Arae (γ Ara), a B1 I star at d = 689 pc that was chosen because it is known to display a variable and equatorially-enhanced stellar wind (Prinja et al., 1997) that could potentially host a population of rovibrationally excited H_2 at the wind/ISM interface. CHESS is ideally suited to study this molecular population, providing insights into a key catalyst in the chemistry of the diffuse and translucent ISM and the thermal and turbulent environments of both atoms and molecules in our Galactic neighborhood.

2.2 Instrument Design

CHESS is an objective f/12.4 echelle spectrograph. The instrument design included the development of two novel grating technologies and flight-testing of a cross-strip anode microchannel plate (MCP) detector (Beasley et al., 2010). The high-resolution instrument was designed to achieve resolving powers $\geq$ 100,000 $\lambda/\Delta\lambda$ across a bandpass of 1000$-$1600 Å. It is an aft-looking payload, housed in three 17.26" diameter rocket skins. It is split into two sections - a vacuum (spectrograph) section and an electronics section - that are separated by a hermetic bulkhead. The vacuum section uses two 113.36 cm long rocket skins with hermetic joints The overall length of the payload is 292.10 cm from mating surface to mating surface and its weight is 361 lbs.

A SolidWorks rendering of the spectrograph and electronics sections of CHESS is provided in Figure 2.1, a Zemax ray trace of the optical path in Figure 2.2, and a picture of the physically assembled spectrograph section in Figure 2.3. The only mechanical mechanism on CHESS (other than the NASA Sounding Rockets Operations Contract supplied shutter door) is a manual butterfly valve attached along the 180° line on the aft spectrograph skin. This allows for the evacuation of the experiment throughout development, integration, and pre-flight activities, in order to safeguard the sensitive optical coatings and detector photocathode. A carbon-fiber optical metering structure, comprised of five 2.54 cm diameter x 182.88 cm long carbon fiber tubes, is attached to the aft side of the hermetic bulkhead. Along these tubes are three aluminum disks that act as the mounting points for the mechanical collimator, echelle grating, and cross disperser grating. The assembly of carbon fiber tubes and aluminum plates will be refered to as the "space frame" throughout this work. The detector is mounted with a hermetic seal to the forward side of the 1.00" thick hermetic bulkhead and faces aft, into the vacuum section. Combined, these components comprise the CHESS spectrograph. A brief overview of each component in the instrument is given below, with further details provided in the referenced sections.

- A mechanical collimator, consisting of an array of 44 12 mm $\times$ 12 mm $\times$ 1000 mm anodized aluminum tubes, sets the CHESS collecting area and field of view and allows on-axis stellar light through to the spectrograph. Each tube has an open area of 10.74 mm $\times$ 10.74 mm. Eight of the tubes feed the aspect camera system, while the remaining 36 are used for science. During the integration of CHESS-1 it was found that a direct line of sight between the right-most column of six (four science, two aspect camera) tubes could directly illuminate the detector and so these were blocked to prevent stray light contamination. The remaining open area provides CHESS with a total collecting area of 36.9 cm^2 (after also accounting for the echelle) and a field of view of 0.67°.

- A square echelle grating (§2.3.1), with a ruled area of 102 mm $\times$ 102 mm, a designed groove density of 87 grooves/mm and a designed angle of incidence (AOI) of 63°, intercepts and disperses the FUV stellar light into higher diffraction terms (m = 200–124). The grating is coated with Al+LiF.

- Instead of using an off-axis parabolic cross disperser (Jenkins et al., 1988), CHESS employs a holographically-ruled cross dispersing grating with a toroidal surface figure (§2.3.2). The cross disperser is ruled over a square area (100 mm $\times$ 100 mm) with a groove density of 351 grooves/mm and was designed to have a surface radius of curvature (RC) = 2500.25 mm and a rotation curvature (ρ) = 2467.96 mm. The grating spectrally disperses the echelle orders and corrects for grating aberrations (Thomas, 2003). The grating is coated with Al+LiF.

- The cross-strip MCP detector (Siegmund et al., 2009; Vallerga et al., 2010) is circular in format, 40 mm in diameter, and capable of total global count rates of $\sim$10^6 counts/second (§2.4.1). The cross-strip anode allows for high resolution imaging, with

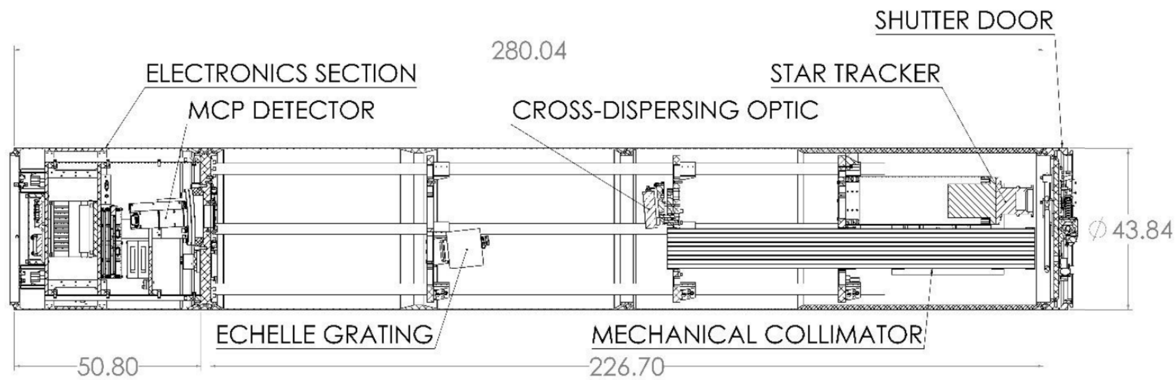

Figure 2.1: A SolidWorks rendering of the spectrograph and electronics sections of CHESS. Labeled are relevant spectrograph structures and optical components. All stated quantities are in units of centimeters.

the location of a photoelectron cloud determined by the centroid of current readout from nine anode "fingers" along the x and y axes. Figure 2.4 displays an example of a laboratory spectrum taken with the fully integrated and aligned CHESS instrument.

The CHESS instruments also flew with as many as three additional optical paths. The first was the aspect camera, which was used to align the spectrograph to the target during calibrations and flight. The aspect camera system uses two pick-off mirrors and the cross disperser to direct zeroth-order visible light to an intensified Xybion camera. This system existed on all four flights of the payload. On CHESS-3 and CHESS-4, we additionally flew a side pointing Nocturn camera to assess its flight performance as a potential aspect camera. This low-light camera is an off-the-shelf device manufactured by Photonis and could be useful as a replacement for the Xybion aspect camera currently commissioned aboard sounding rocket missions. The Nocturn took a series of images during both flights to show that it remained functional for the duration of the missions. Example images are shown in Figure 2.5.

Finally, for CHESS-4 we planned on flying a new CCD detector (§2.4.2) which would not have provided the same instanteous feedback as the MCP. That feedback is useful for confirming that our optical path maintained alignment during launch. While the Xybion

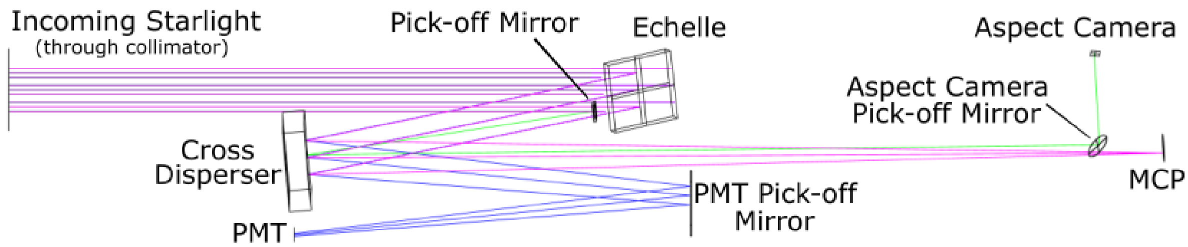

Figure 2.2: The Zemax ray trace of CHESS, including the secondary aspect camera system and the PMT. The mechanical collimator reduces stray light in the line of sight and feeds starlight to the echelle. The echelle disperses UV light into high-dispersion orders, which are focused by the cross disperser onto the detector plane. The green lines trace light with $\lambda =$ 5500 Å through to the Xybion aspect camera. The blue lines trace light with $\lambda = 1850$ Å to the PMT, which only flew on CHESS-3. The pink lines trace light with $\lambda = 1216$ Å to the MCP.

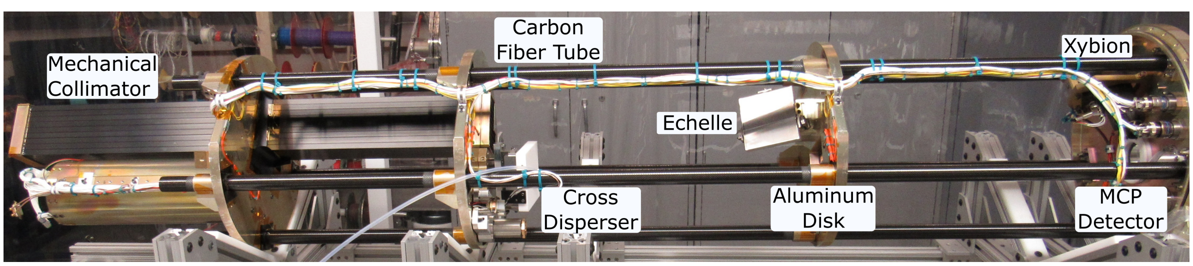

Figure 2.3: A picture of the assembled spectrograph section with several prominent features labeled. The cross disperser is pictured under a nitrogen purge cover that was used to maintain a dry and clean environment on the surface of the optic while it was not under vacuum. The pictured echelle was the grating that flew on CHESS-1 and was no longer in use, so the same precautions were not taken.

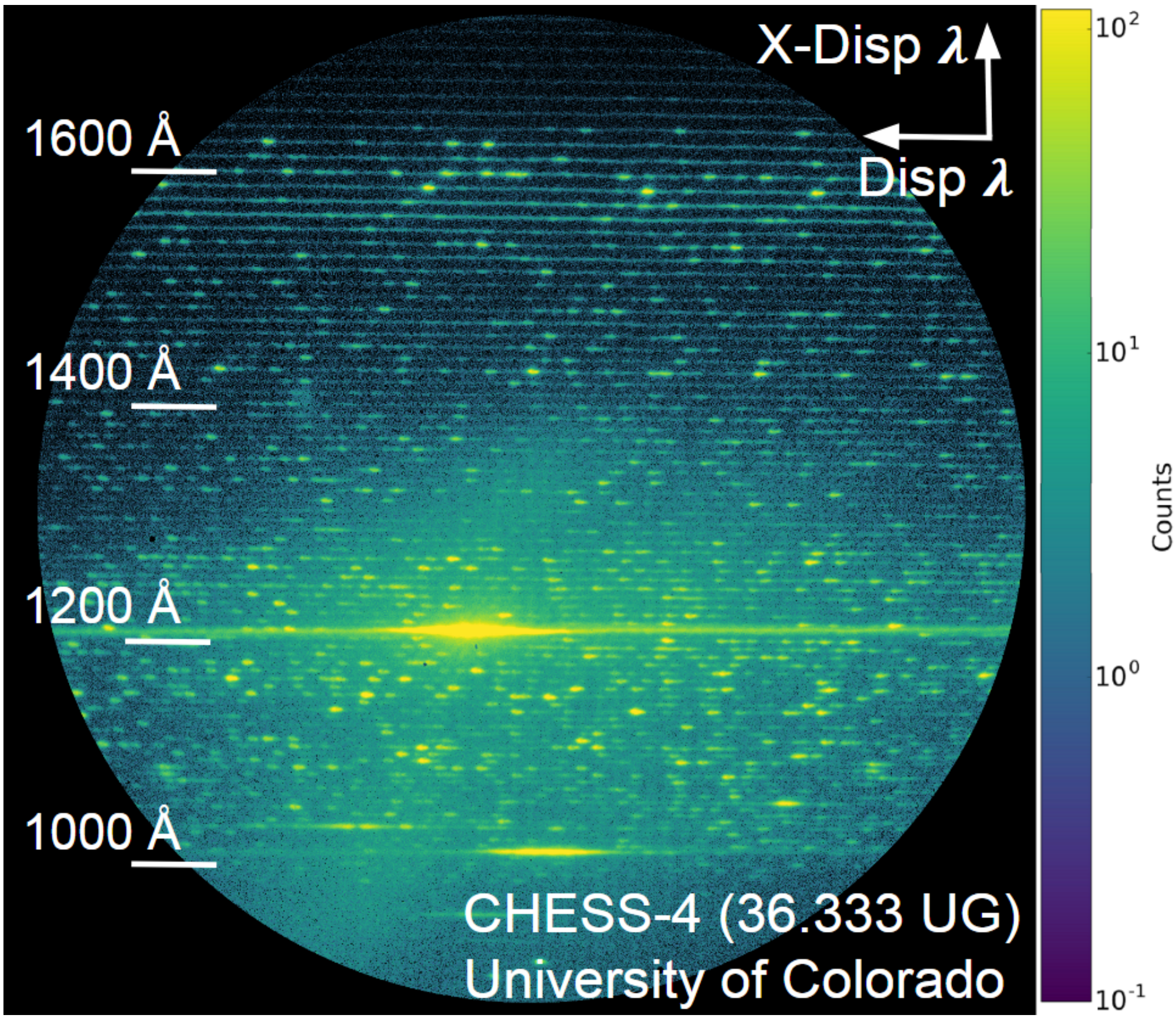

Figure 2.4: A false-color representation of the laboratory echellogram of CHESS-4 in the pre-flight configuration, binned to 4096 × 4096 pixels. The black/purple represents little to no counts in the binned pixel location, while yellow represents emission lines from atomic and molecular hydrogen. Overlaid are arrows showing the direction of dispersion from the echelle and cross disperser and the tick marks showing the approximate location of different spectral regions. The final laboratory calibration image contains ∼70 million photon counts. The displayed orientation, with dispersion direction running along the x axis and the cross dispersion direction running along the y axis, will be used to reference spectral directions in subsequent sections.

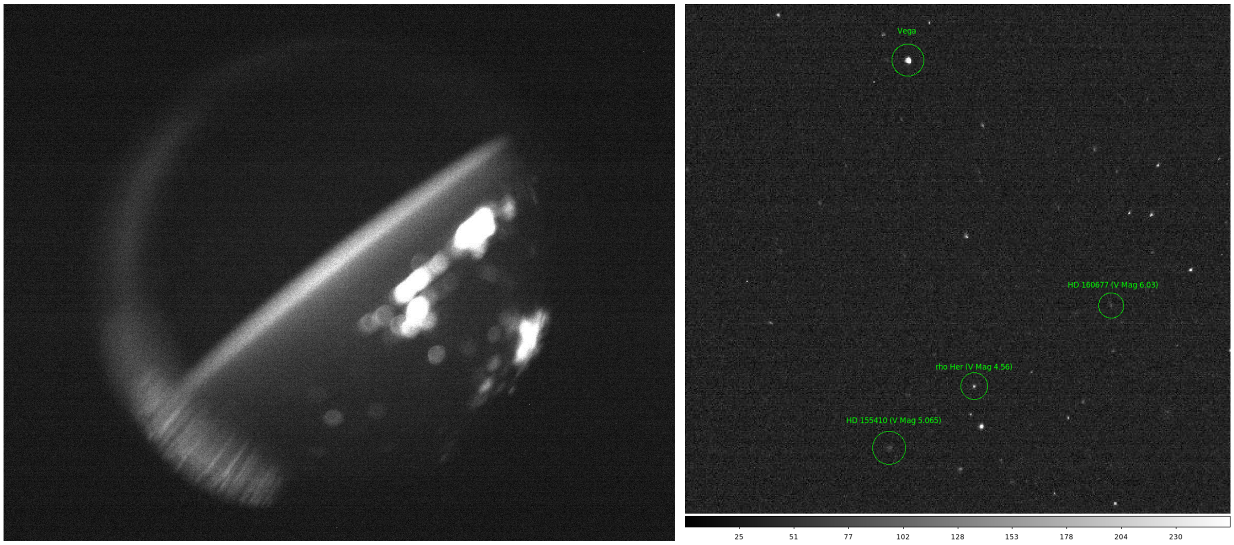

Figure 2.5: *Left:* An image of Earth's limb, taken by the side-pointing Nocturn on CHESS 3. *Right:* An image of the Hercules constellation taken by the Nocturn on CHESS 4.

provided a secondary check that the payload is aligned, its optical path uses a reference flat instead of the echelle. To obtain a complete confirmation that the optical path did not shift during flight, we planned on using a photomultiplier tube (PMT) from Hamamatsu, Inc. as an on-board photon counting device. As an initial test, we installed the PMT next to the cross disperser for CHESS-3. The PMT system used the echelle, the m = +1 order from the cross disperser, and a UV-enhanced mirror to direct FUV light to the PMT (see Figure 2.2). Alignment was then confirmed by measuring a peaked count rate in the PMT while on-target.

2.3 Optical Components

2.3.1 Echelle Grating

The original CHESS echelle was fabricated as a part of a research and development effort to produce higher efficiency gratings. Two of the most common grating ruling techniques are mechanical and holographic. Facets on mechanically-ruled gratings are physically cut into the surface of the grating substrate using a diamond tipped stylus. This method excels at

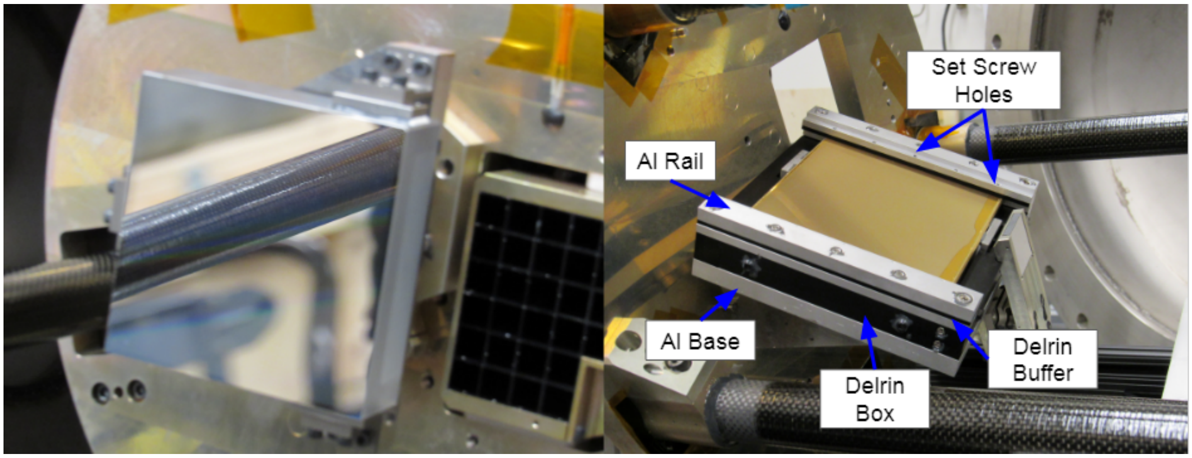

Figure 2.6: *Left:* The CHESS cross disperser. *Right:* The CHESS echelle that flew on the third and fourth launches of the payload. In this image it is mounted in the CHESS-4 curvature-inducing case, with several prominent features labeled.

creating sharp blazed facets but the wear that occurs on the diamond tip leads to variability in the final groove profile, resulting in increased inter-order scatter (Landsman & Bowers, 1997).

Holographically-ruled gratings are created by the interference of two laser beams on the surface of a light sensitive material, called photoresist. The photoresist under regions where the laser fringes are coherent becomes weakened and can subsequently be chemically etched away, leaving behind the desired groove pattern. The resulting pattern has a high degree of uniformity and holographic gratings historically have better scatter properties than mechanically ruled gratings. At the same time, holographic gratings have limitations that restrict their applicability. Their groove spacing is dependent on the wavelength of the laser and, by extension, the photoresist used for production. Due to the selection of commercially available photoresists and lasers, holographically-ruling low line density gratings has generally not been possible. In addition to this, the interference fringes do not have binary amplitude. Instead, the intensity follows a sinusoidal variation and therefore the grooves it produces are also sinusoidal. This wavy profile suffers from lower groove efficiency compared to the saw tooth profile produced by a mechanically ruled gratings. While blazed profiles can be produced through post processing, that process comes with added cost, complexity, and additional limitations (Lerner et al., 1981; Palmer, 1989; Palmer & Loewen, 2005).

Given the blazed facets and low line densities of echelle gratings, they are generally produced using mechanical ruling processes and their performance suffers as a result of the inherent scatter. In an effort to maximize the efficiency of the CHESS instrument, the original echelle was designed to be a lithographically-etched grating, relying on a deposited mask to define square well grooves that would have the combined ideal groove efficiency of mechanical ruling and the low scatter of holographic ruling. This process was tested on CHESS-1 where the grating was a 100 mm x 100 mm x 0.7 mm silicon wafer with a groove density of 69 grooves/mm and $\alpha = \beta = 67°$. As detailed in Hoadley et al. (2014), attempts to fabricate an echelle that met these specifications using lithography lead to gratings with peak efficiencies of ~5%, four times smaller than the minimum acceptable value for CHESS. Additional attempts were made using an electron-beam etching method lead to similar results (Hoadley et al., 2016). For this reason, the echelles flown on CHESS-2 through CHESS-4 were commercially-available mechanically-ruled gratings, coated with Al+LiF.

For CHESS-3 and 4, the echelle was fabricated by Richardson Gratings (formerly Milton-Roy; Rochester, NY). It was a 110 mm x 110 mm x 16 mm thick block of Zerodur, with a designed 87.0 grooves/mm and $\alpha = 63.0°$, that was ruled over a 102 mm x 102 mm area. During initial alignments of CHESS-3 (see Section 2.6.1), we found that these values were closer to 89.5 grooves/mm and $\alpha = 63.2°$, which were still within the CHESS tolerances. Figure 2.7 shows the peak order groove efficiency of the Richardson grating compared to the echelle used in CHESS-2. The Richardson echelle greatly outperformed the CHESS-2 grating at $\lambda \gtrsim 1216$ Å, which contributed to the boost in effective area (§2.5) measured for CHESS-3 and 4, as shown in Figure 2.11.

The CHESS-3 echelle mounted to the payload through three Invar pads that are bonded to the neutral plane of the optic, nearly 120° apart, and are connected to three titanium flexures. The flexures are attached to an aluminum mounting plate. The plate was further

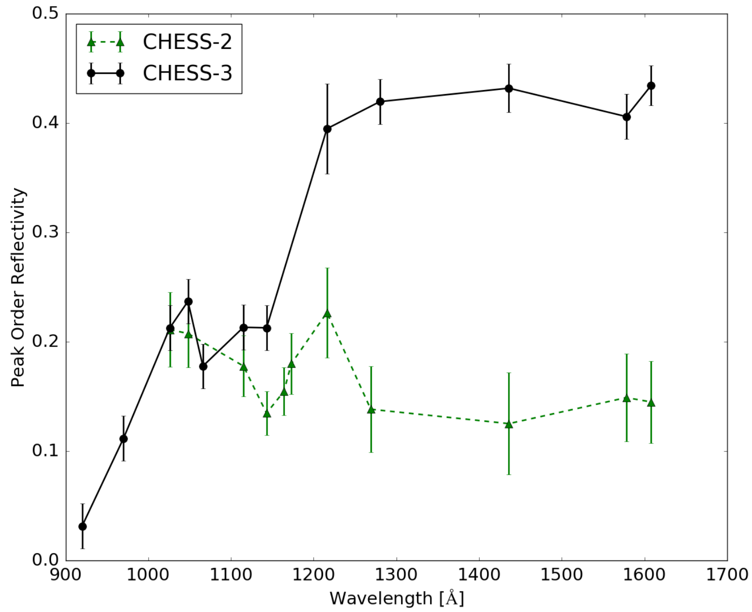

Figure 2.7: A comparison of the peak order reflectivities of the echelles used on CHESS-2 (green dashed line) and CHESS-3 (solid black line). Both gratings had an Al+LiF coating applied for flight.

held within an aluminum mount, which was set to the desired AOI and was attached directly to the forward most disk of the space frame (Figure 2.6). The flexures prevent the surface of the optic from warping due to stress transfer from a coefficient of thermal expansion mismatch in mounting components.

Due to a fabrication error in the cross disperser (§2.3.2) we found that the CHESS instrument was unable to achieve its designed resolving power. To help improve the instrument resolution for CHESS-4, we shaped the echelle grating by precisely torquing set screws at various points on the optic. This process required a new grating mount that could facilitate the different set screw positions. This mount was based on the secondary flight housing used on the FORTIS sounding rocket (Fleming et al., 2011) and can be seen in Figures 2.6 and 2.9. It is comprised of an aluminum base and Delrin box. The grating is held in the box by aluminum rails, with Delrin spacers underneath, that run along the sides of the optic. The grating sits in the box on top of a square Delrin spacer. To shape the optic, each aluminum rail has five holes for set screws that can be torqued into the Delrin beneath. The Delrin acts

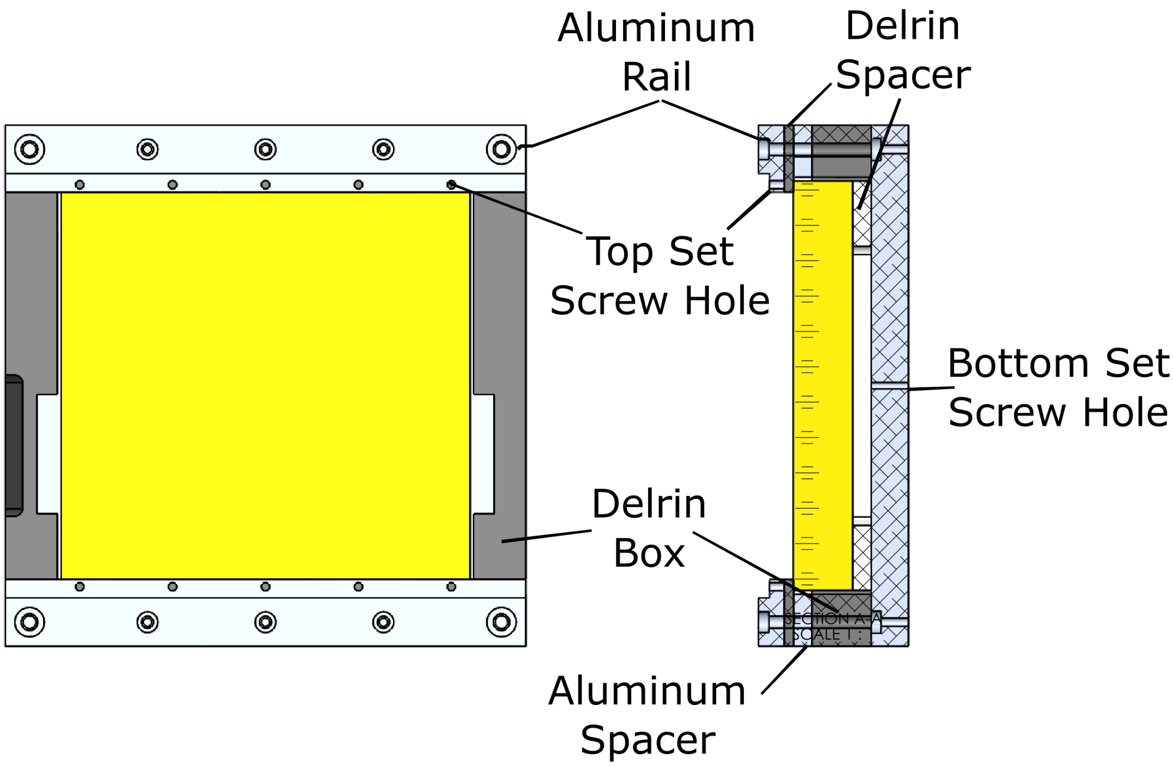

Figure 2.8: A CAD drawing of the echelle mount used to achieve the bend. Prominent features are labeled for reference.

as a buffer layer that prevents direct contact between the metal screw and Zerodur optic and helps distribute the pressure applied by the screw. There are two additional holes that pass up through the bottom aluminum layer into the lower Delrin spacer that are used to apply pressure to the bottom of the optic, facilitating the creation of a concave bend. A labeled CAD image of the mount is shown in Figure 2.8.

To ensure that the shaped grating surface did not impact its efficiency, we induced a roughly "flight-like" curvature in it, using two set screws on top and two on the bottom, and then measured its reflectivity at four different spots that spanned the range of surface

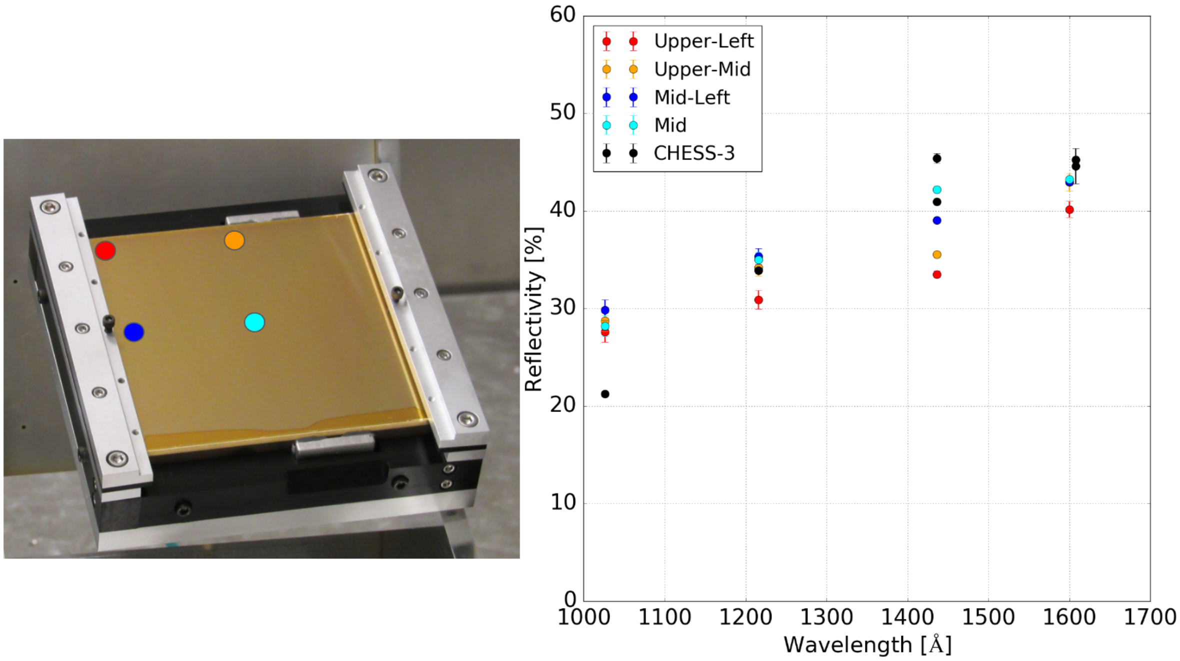

Figure 2.9: *Left:* The echelle in the reflectivity chamber. The four colored spots indicate the different positions where measurements were taken. The orange and blue spots are located at the highest and lowest points on the optic. For reference, one of the bottom sets screws was roughly located under the orange circle, the other was in the same spot on the opposite edge of the grating. *Right:* The measured reflectivities at the four points shown on the left, as well as the reflectivites of the unbent echelle from CHESS-3, for reference.

heights. The resulting reflectivites are plotted in Figure 2.9. We did not see any significant impact to the overall efficiency as a function of position on the grating. The one exception was a larger variation in the reflectivities at 1446 Å. Due to the consistency of the other points and the lower signal produced at this wavelength, we suspect that is more indicative of uncertainties in our setup. This variation was seen when performing other optics tests at this wavelength, but no longer appears to be an issue after a full system alignment was performed in Fall of 2018. §2.6.2 provides details on the procedure followed to induce the bend in the optic for flight.

2.3.2 Cross Disperser Grating

The CHESS cross disperser grating is a 100 mm $\times$ 100 mm $\times$ 30 mm fused silica optic with a toroidal surface profile. The toroidal surface shape separates the foci of the spatial and sagittal axes of the dispersed light. The cross dispersing optic is a novel type of imaging grating that represents a new family of holographic solutions and was fabricated by Horiba Jobin-Yvon (JY). The line densities are low (351 lines per mm), and the holographic solution allows for more degrees of freedom than were previously available with off-axis parabolic cross dispersing optics. The holographic ruling corrects for aberrations that otherwise could not be corrected via mechanical ruling. The grating is developed under the formalism of toroidal variable line spacing gratings (Thomas, 2003) and corresponds to a holographic grating produced with an aberrated wavefront via deformable mirror technology. This results in a radial change in groove density and a traditional surface of concentric hyperboloids from holography, like those used in ISIS (Beasley et al., 2004) and COS (Green et al., 2003). The cross disperser mounted to the payload using similar Invar pads + flexures that were used for the CHESS-3 echelle. In this case, the aluminum mounting plate was affixed directly to the middle disk of the space frame (Figure 2.6).

As previously mentioned, during the integration of CHESS-2, we noticed that the cross disperser needed to move closer to the MCP than expected to reach the focus of the orders, indicating that the radii of curvature of the optic were not correct. This was tested post-flight by mounting the cross disperser in its flight orientation on an optical bench and measuring the two focal lengths using a white light source. The resulting measurements showed that the focal lengths were the correct values, so the substrate was manufactured correctly, but the grooves were ruled 90° off. This meant that the RC and the ρ were interchanged, making it impossible to simultaneously focus the spectral lines and orders thus limiting the spectral resolution of the instrument. The resulting line spread function (LSF) caused by this defect is shown in Figure 2.10. Instead of a single high-resolution peak, we see a four peaked structure that is a result of the fact that the individual rows of the collimator tube

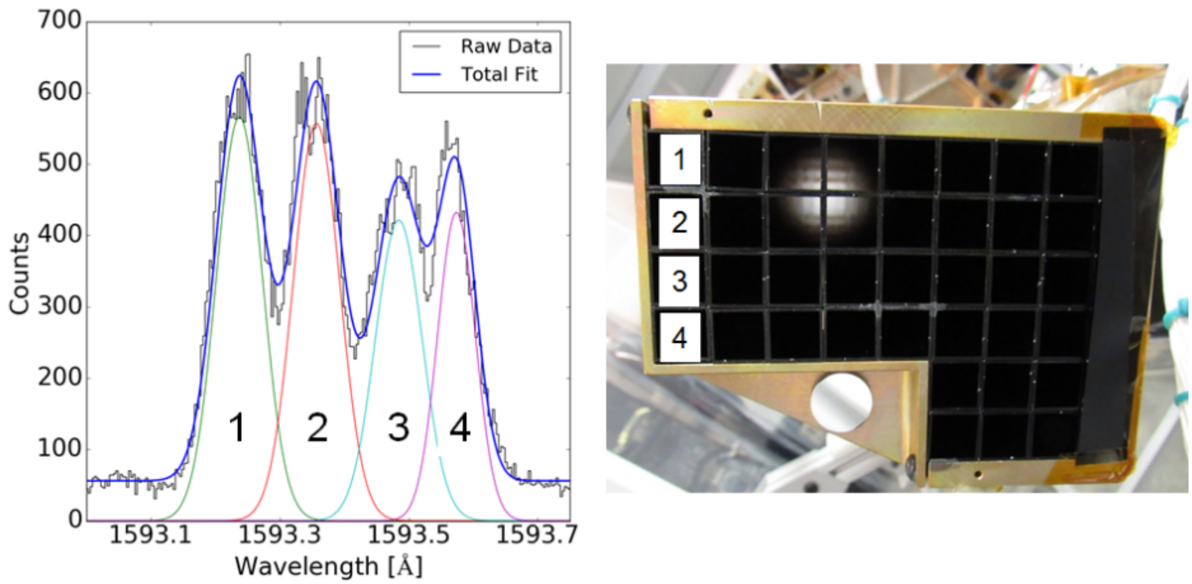

Figure 2.10: *Left:* An example LSF from the CHESS-3 spectrum, showing the four peaked structure that results from each collimator tube being resolved at the detector. The numbers in each peak correspond to the collimator tubes numbered in the image on the right.

are all still resolvable at the detector. This was mitigated in CHESS-4 by introducing the mechanically stressed echelle grating.

Figure 2.11 shows the efficiency of the cross disperser for the m = -1 order. The Al+LiF coating was not reapplied between flights, instead the optic was stored in a nitrogen purge cabinet when not in use. We did not see any significant degradation in the performance of the optic between the two flights. The cross disperser is effective at dispersing most of the on-axis light into the m = $\pm$ 1 orders and suppressing the m = 0 order because of the characteristic sinusoidal groove profiles created via the ruling procedure at JY. Additionally, at optical wavelengths, the reflectivity of the m = 0 order becomes comparable to the m = $\pm$ 1 orders. This allowed us to build the secondary camera system to track the movements of our optical axis and target acquisition during flight.

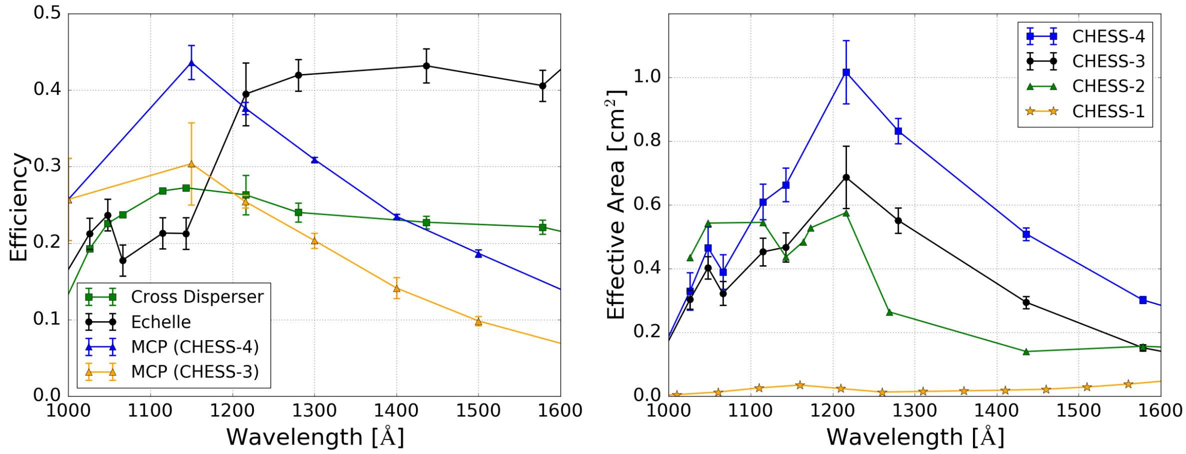

Figure 2.11: *Left:* Performance (for each grating: peak order reflectivity, and for the detector: DQE) of all optical components of CHESS-4. Our in-house measurements of the MCP DQE end at ~1100 Å. We used values provided by Sensor Sciences Inc. to extend the curve down to 900 Å. *Right:* A summary of A_{eff} for all four CHESS launches.

2.4 Detectors

2.4.1 Cross-Strip Anode Microchannel Plate Detector

The 2015 NASA Cosmic Origins Program Annual Technology Report, which lists the prioritized technologies that are crucial for the technical and scientific success of future missions, emphasized that the technology readiness level (TRL) for large format, high count rate, and high detective quantum efficiency (DQE) MCP detectors needed to meet the goals of future UV missions. In support of this effort, a cross-strip MCP detector was built and optimized to meet the CHESS spectral resolution specifications at Sensor Sciences (Siegmund et al., 2009; Vallerga et al., 2010). The detector has a circular format and a diameter of 40 mm. The detector uses two plates made from lead silicate glass, each containing an array of 10 μm diameter channels. The plates are stacked on top of one another and are arranged in a "chevron" configuration (see Figure 2.12). The top plate is coated with a CsI photocathode.

There are two wire grids that help maximize the performance of the MCP. The first is an ion-repeller grid. Like photoelectrons, incoming ions can generate an electron cloud in the plates. So, to prevent spurious counts, a positively-charged grid is placed in front of

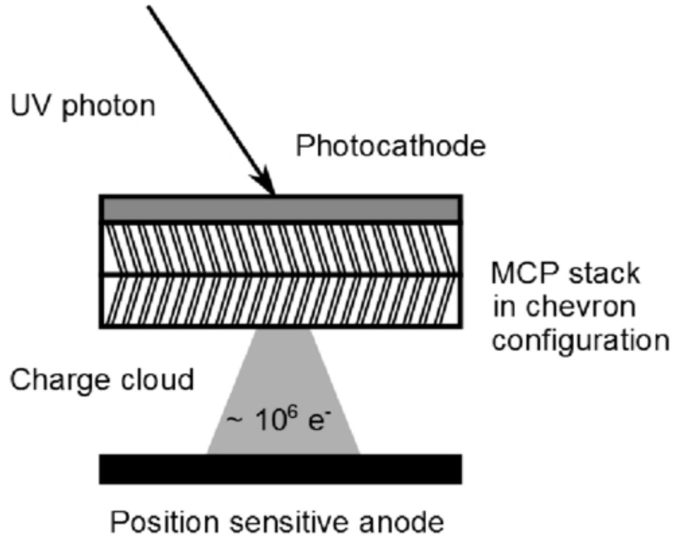

Figure 2.12: A cross-sectional view of an MCP detector, demonstrating the chevron configuration of the plates. From Hermanutz et al. (2014).

the MCP to repel incoming charged particles. The second grid is the DQE-enhancement grid. Photoelectrons can be ejected from the photocathode in any direction. Therefore, some signal could be lost due to electrons flying up and away from the plates instead of down into them. To mitigate this, a second negatively-charged wire grid is placed close to the surface of the MCP, creating a negative potential that drives the escaping electrons back down towards the plates.

The previously discussed delay line and MAMA MCP detector architectures (§1.7.2) both suffered from trade-offs in the spatial resolution vs dead time (i.e. the shortest possible time between events a detector can handle) parameter space. For a high resolution instrument, like CHESS, that is observing bright targets, the ideal detector would maximize both of those parameters. The cross-strip detector is one such device. A cross-strip anode is a two layer series of anode strips, running vertically (for x positioning) on one layer and horizontally (for y positioning) on the other (Figure 2.13). Each strip has its own associated read out electronics, facilitating the desired higher count rates. The charge cloud produced by the

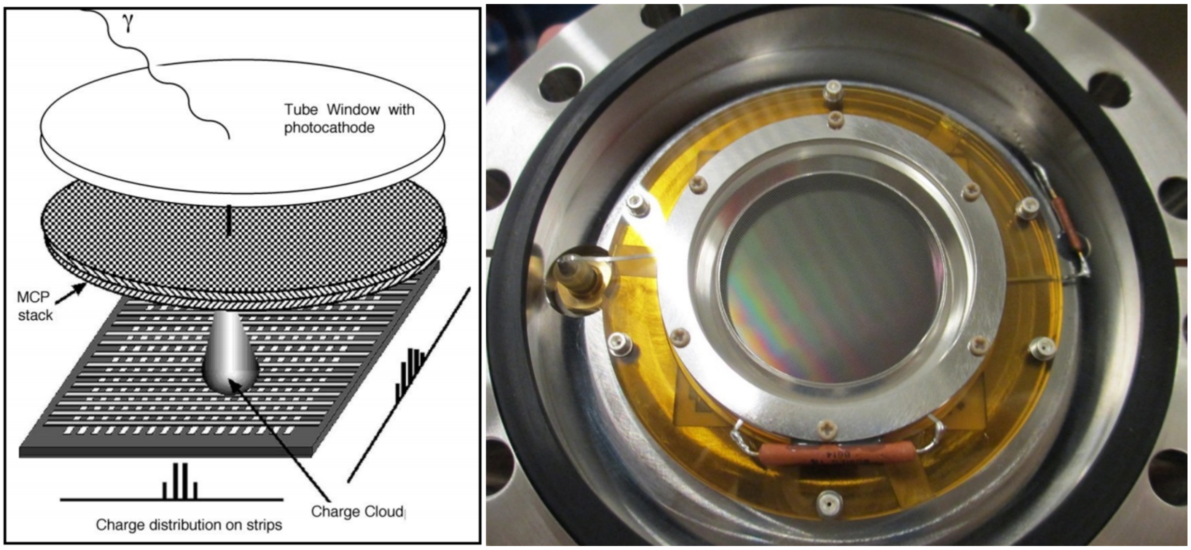

Figure 2.13: *Left:* An schematic image of a CHESS-like cross-strip anode MCP detector, from Vallerga et al. (2010). In the depicted image, the detector uses a window photocathode, while the CHESS detector had the photocathode applied to the surface of the plates. *Right:* The CHESS detector.

MCP spans roughly nine of these anode strips in both directions. The resulting charge measured from each strip is used to centroid the cloud location to an accuracy below the width of a single anode, meeting the desired high spatial resolution. The final measured resolution of the CHESS detector was 25 μm in the dispersion direction and 30 μm in the cross dispersion direction and it was capable of handling global count rates up to 1 MHz. The DQE, which measures the likelihood of a photon being detected, across the CHESS bandpass is plotted in Figure 2.11. To help maintain the throughput of the instrument, the CsI photocathode was reapplied by Sensor Sciences for the final launch.

2.4.2 delta-doped CCD

For CHESS-4, we also collaborated with the NASA Jet Propulsion Laboratory (JPL) and Arizona State University (ASU) to flight qualify a delta-doped high purity p-channel CCD that was expected to exhibit higher DQE than MCPs in the FUV bandpass. JPL fabricated the detector by processing existing fully depleted high purity p-channel CCD wafers that were procured from Lawrence Berkeley National Laboratory. JPL applied their end-to-end post-fabrication back illumination processing before applying the delta-doped layer to the back surface of the CCD. The surface of an Si crystal will have open chemical bonds that O can bind to, forming SiO_2. A potential well forms at the Si-SiO_2 interface that, combined with the short penetration depth of UV photons into Si, can result in trapped charge and a lower overall DQE. By doping the Si layer with a negatively charged ion, this potential well can be mitigated, allowing the photon generated charges to move as intended within the Si substrate (Nikzad et al., 1994, 2017).

The calibrated CCD chip was delivered to ASU, where a focal plane assembly (FPA) was built and optimized for the chip. The entire assembly was housed in an aluminum tube with a conflat flange designed to be mounted to the rear bulkhead of CHESS. The CCD chip, FPA, and controller, as received from ASU in May 2017, are shown in Figure 2.14. We measured the DQE of the CCD in our detector calibration chamber, using a vacuum monochromator and a NIST-calibrated photodiode (Jacquot et al., 2011; Nell et al., 2016). The detector displayed lower than anticipated DQE across CHESS bandpass, which was traced to hydrocarbon contamination from an aluminum cap on the FPA that was not cleaned after machining at ASU (Figure 2.15). Attempts to clean the surface of the chip did not lead to any improvement. The detector performance was insufficient to meet the flight science goals of CHESS-4 and the MCP detector was used instead.

2.5 Instrument Performance

Figure 2.11 summarizes the performance of both optics and the MCP, as measured before the CHESS-3 and CHESS-4 launches. In between flights, both optics were stored in a dry nitrogen environment and we did not observe a noticeable degradation in their reflectivities during that time. Therefore, we only include a single curve for each optic that suitably describes their efficiencies on both launches. We did have the CsI photocathode reapplied to the MCP after CHESS-3. This resulted in a gain of ~10 percentage points in the DQE

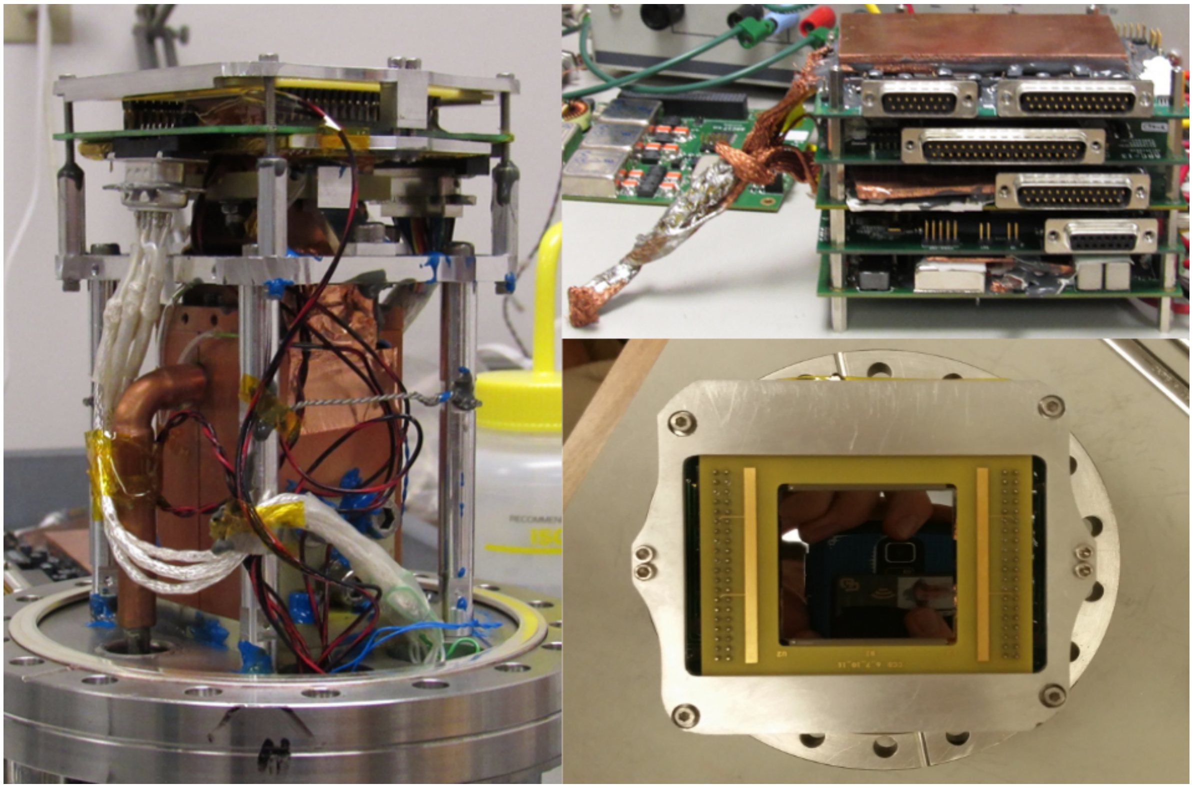

Figure 2.14: The ASU CCD payload components. The CCD focal plane assembly (left), the CCD controller (top right), and the JPL delivered delta doped CCD (bottom right).

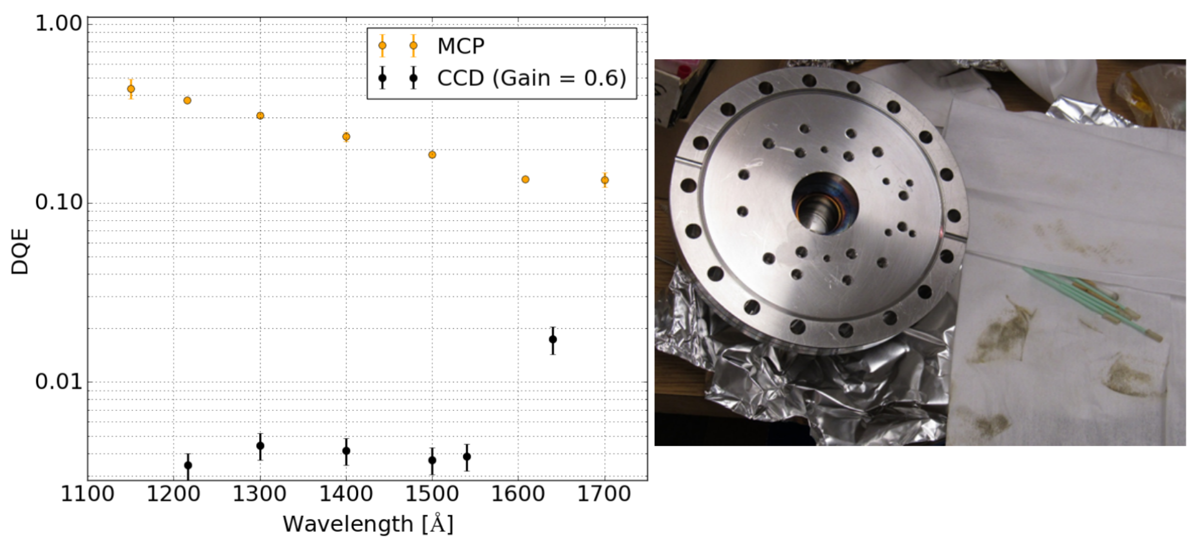

Figure 2.15: *Left:* The DQE of the contaminated delta-doped CCD (black points) and CHESS MCP (orange points). Right: The aluminum cap that was the source of the machining oil.

of the detector. The right plot in Figure 2.11 shows the effective area across the bandpass of each iteration of CHESS. Effective area (A_{eff}) is a way to express total collecting area of the instrument by accounting for the geometric area as well as the efficiencies of all of the hardware. We calculate A_{eff} (in cm^2) for CHESS in the following way:

$$A_{\text{eff}} = 36.9 R_{\text{echelle}} R_{\text{x-disp}} DQE_{\text{MCP}} \tag{22}$$

Where 36.9 [cm^2] is the total open area of the mechanical collimator. R_{echelle} and $R_{\text{x-disp}}$ are the reflectivities of the echelle and cross disperser. We see that, due to the higher efficiency of the Richardson grating and the reapplication of the MCP photocathode, CHESS-4 achieved the largest overall effective area of any of the CHESS flights.

Using these effective area values, along with past observations of β Sco and γ Ara, we calculated expected on-target count rates (not including Lyα airglow) which are shown in Figure 2.16. Both objects had *IUE* observations covering the CHESS bandpass at $\lambda >$ 1150 Å. γ Ara had *Copernicus* U2-channel observations that provided continuous coverage through the remainder of the CHESS bandpass. β Sco lacked the same complete coverage and so we instead filled this region by assuming a uniform flux equal to the flux at 1150 Å. These predicted count rates were used as guides during flight to ensure that the instrument was operating as expected. For example, during the flight of CHESS-2, we were seeing count rates $\sim$5$\times$ below expectations. This discrepancy was eventually traced to an issue in our payload alignment procedure and lead to a re-evaluation of that process.

2.6 CHESS Assembly and Alignment

2.6.1 Alignment and Focusing

The steps taken to align the instrument and focus the echellogram for flight were as follows:

- **Confirm alignment of the collimator:** The mechanical collimator was installed and aligned in the payload prior to CHESS-1 and was never removed. Since the instrument

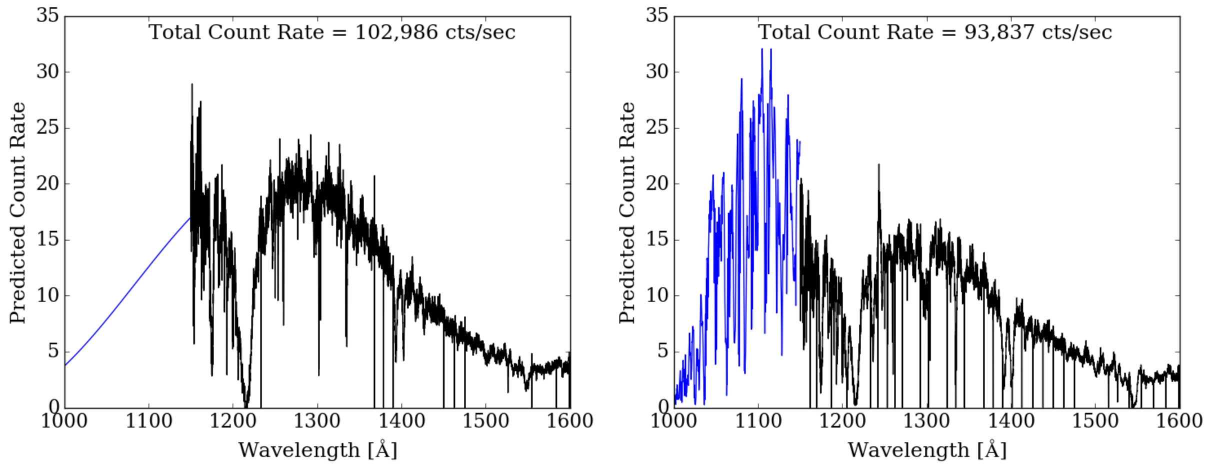

Figure 2.16: *Left:* The predicted count rate of β Sco, as observed by the CHESS instrument. In black are the *IUE* observations. In blue is the curve created assuming a fixed flux times the measured effective area curve for the instrument. *Right:* The same as the left figure, but for CHESS-4. In this case, the blue curve is generated using *Copernicus* U2 observations.

undergoes a variety of dynamic events, from launch to touchdown, our first step was always to confirm that that collimator did not shift and become misaligned from the mechanical axis. To do this, we back-reflected a laser off of a reference mirror that was epoxied to the front-most disk of the space frame, thus aligning the laser to the mechanical axis of the payload. The laser was mounted on a vertically-adjustable stand and a horizontally-adjustable translation stage with a micrometer attached for measuring distances. Once the laser was pointed correctly, it was translated so that it was centered on the corner of a collimator tube. The laser was then translated horizontally across the tube, from corner to corner, providing a measurement of the width of the tube. If the collimator was out of alignment, we would find values smaller than expected. This was never found to be the case and so the collimator was never realigned. Images from these steps can be seen in Figure 2.17.

- **Grating installation:** The CHESS gratings were designed to have parameters that allow for optical wavelength solutions. Grating solutions were modeled in Zemax for green (532 nm) and violet (405 nm) wavelengths and then transposed to CAD models

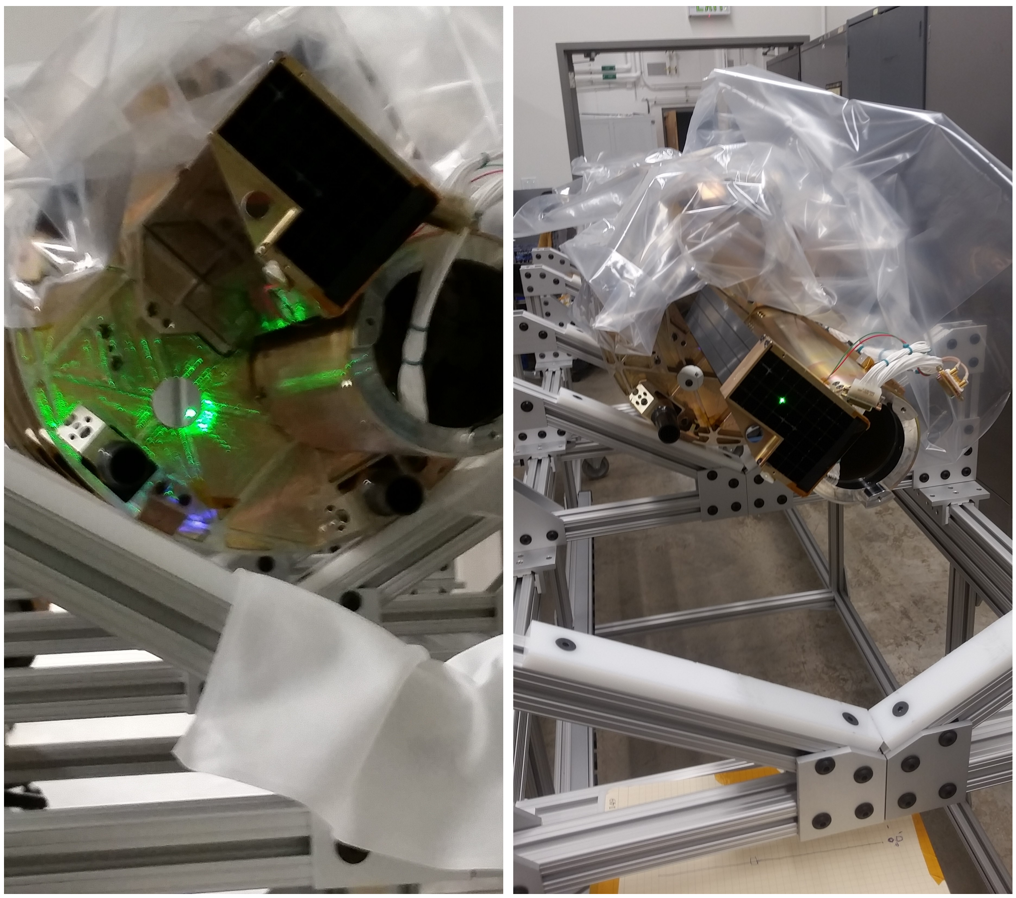

Figure 2.17: *Left:* The laser reflecting off of the epoxied alignment flat. This reflection was used to align the laser to the mechanical axis of the payload. *Right:* The laser aligned to the corner of a collimator tube before it was translated horizontally to confirm collimator alignment.

of the aluminum space frame disks. Print-outs of these expected spot positions along with the aligned laser were then used as guides when installing the echelle and cross disperser. The installation of the echelle used flight ready hardware, while the cross disperser controls the focusing and pointing of the spectrum and so it was initially installed using linear vacuum actuators to control the tip, tilt, and piston motions of the grating (Figure 2.18). The tilt of the cross disperser was set to match the predicted spot positions but no effort was made to focus the system during this step. Finally, the Xybion pick-off mirror was installed on its own tip-tilt mount that attached to the echelle mount. This mirror can be seen in Figure 2.6. It was adjusted until the laser reflection was approximately centered on the cross disperser and hit the lens of the Xybion (Figure 2.19).

- **Vacuum Alignments:** The laser alignments at air provided a good first order placement of the spectrum but finer adjustments and focusing needed to be done using FUV light. This required loading the payload into an external vacuum system, known as the long tank, that allowed for the illumination and operation of the entire payload system while under vacuum (P $\sim 5.0 \times 10^{-6}$ torr). The instrument was loaded into the tank on a tip-tilt table. It was first coarsely aligned using a white light source. The pointing of the payload was adjusted until we could visually confirm that the collimator tubes were uniformly illuminated. The spot produced on the Xybion was then used to finely tune the pointing before installing the MCP and electronics. Once installed, the long tank system was taken to vacuum and the payload was illuminated with FUV light using a hollow-cathode ("arc") lamp, which produces a spectrum of emission lines from a gas that is fed into it. Initially, the gas was a 65/35% mix of hydrogen/argon (H/Ar) but we would also flow room air to obtain additional emission features. The preceding laser alignment steps were generally accurate enough that some portion of the spectrum would be visibile on the MCP and could be used as a guide to drive the cross disperser actuators until a centered spectrum was produced.

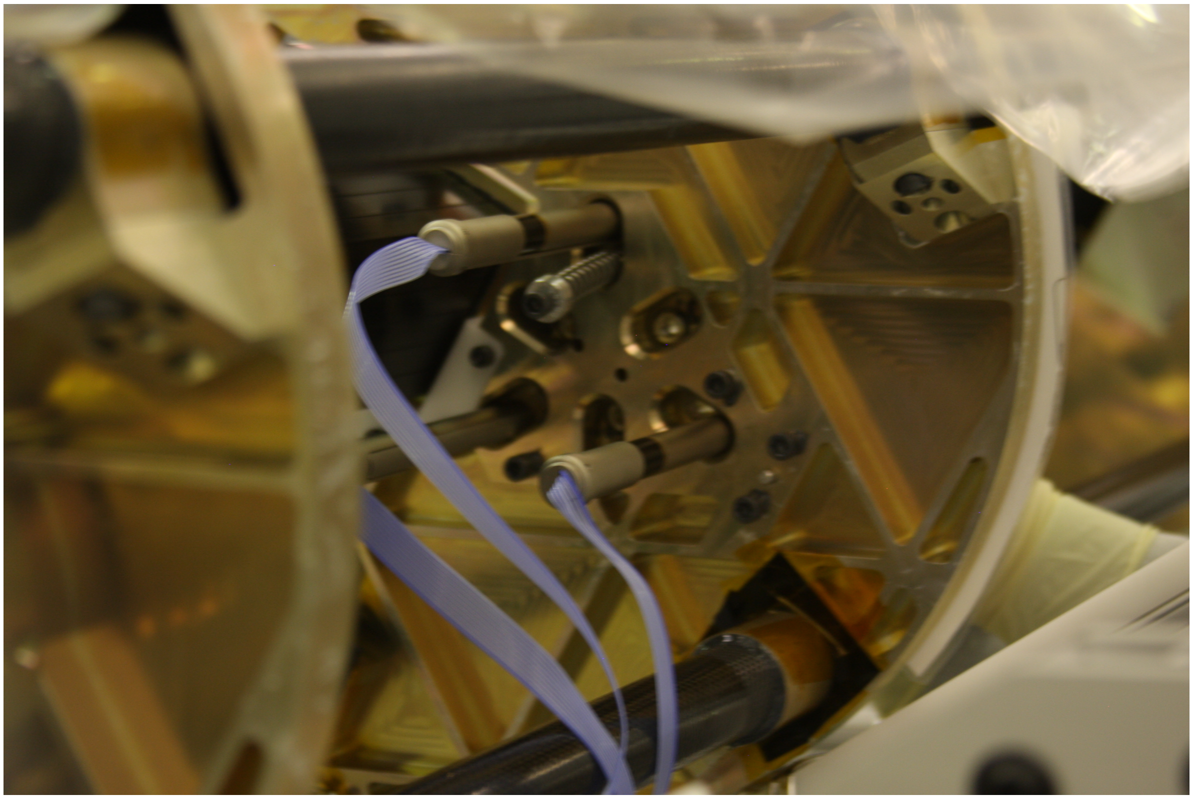

Figure 2.18: A rear view of the vacuum actuators used to control the initial tip, tilt, and piston of the cross disperser. The screw with a spring on it was used to provide resistance to the actuators so that the cross disperser remained rigid. Only one of three of those screws is shown installed in the image.

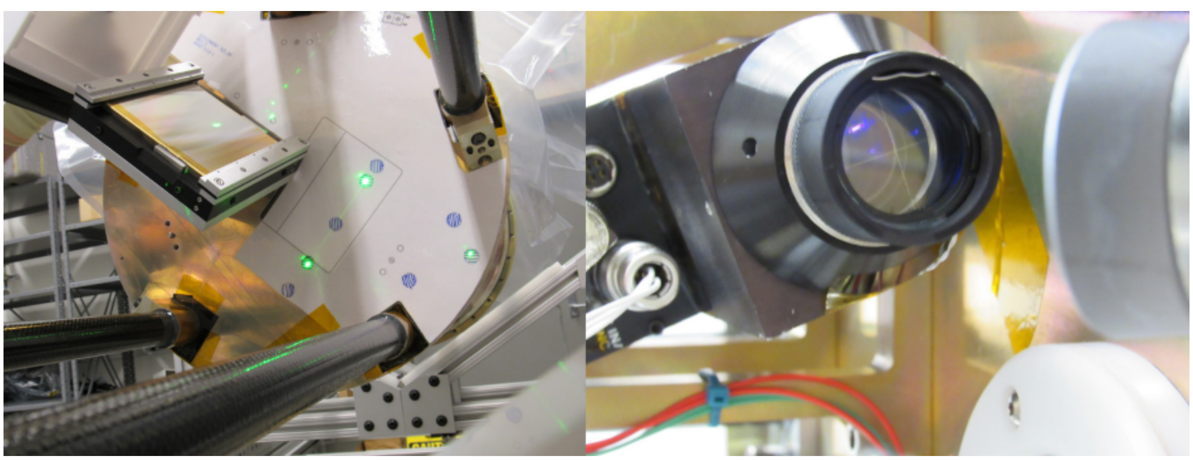

Figure 2.19: *Left:* The CHESS-4 echelle, illumnated with a green laser. Not shown is the second (zeroth-order) bounce off of the cross disperser, which reproduces the expected spot distribution on the space frame print-out. *Right:* The purple laser illuminating the Xybion after the aspect camera optical path completed alignment.

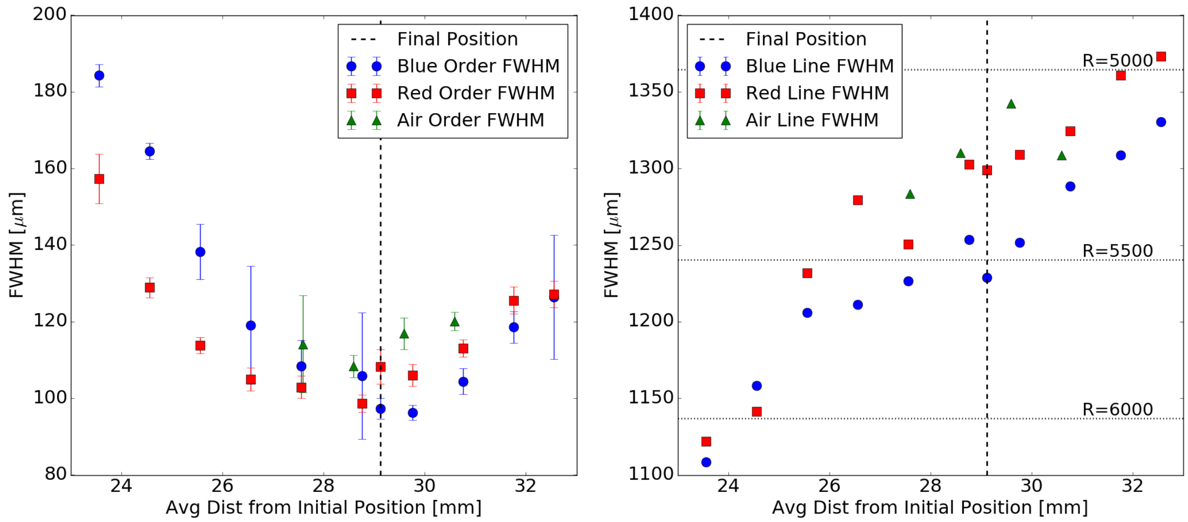

Figure 2.20: Focus curves from CHESS-3, a similar initial result was created for CHESS-4 using the unbent echelle. It is not shown here. *Left:* The FWHM of spectral orders as a function of distance from the initial position of the cross disperser. A larger average distance from the initial position means the cross disperser was closer to the MCP detector. The blue circles show the width of an order on the blue end of the spectrum, red squares show the width of an order on the red end, the green triangles show the width of an order measure when flowing air into the arc lamp. *Right:* FWHMs of spectral features found in the orders used in the left plot. Estimated resolutions are shown as horizontal dotted lines.

- **Focus Curves:** Finally, the spectrum was focused on the detector by pistoning the cross disperser towards the detector and generating a spectrum at fixed steps along the way. For each position, the full width at half maximum (FWHM) of emission features on the red and blue wavelength ends of the spectrum were measured in the dispersion (spectral) and cross dispersion (order) directions. The resulting values were plotted as a function of cross disperser distance, generating the focus curves seen in Figure 2.20. As an additional check, we performed the same measurement while flowing room air into the arc lamp. The final position of the cross disperser was determined by the location of the narrowest order width, not spectral width. While a narrow spectral width would maximize the resolution of the instrument, the resulting overlap between neighboring orders would make the extraction of the one-dimensional (1D) spectrum difficult, if not impossible.

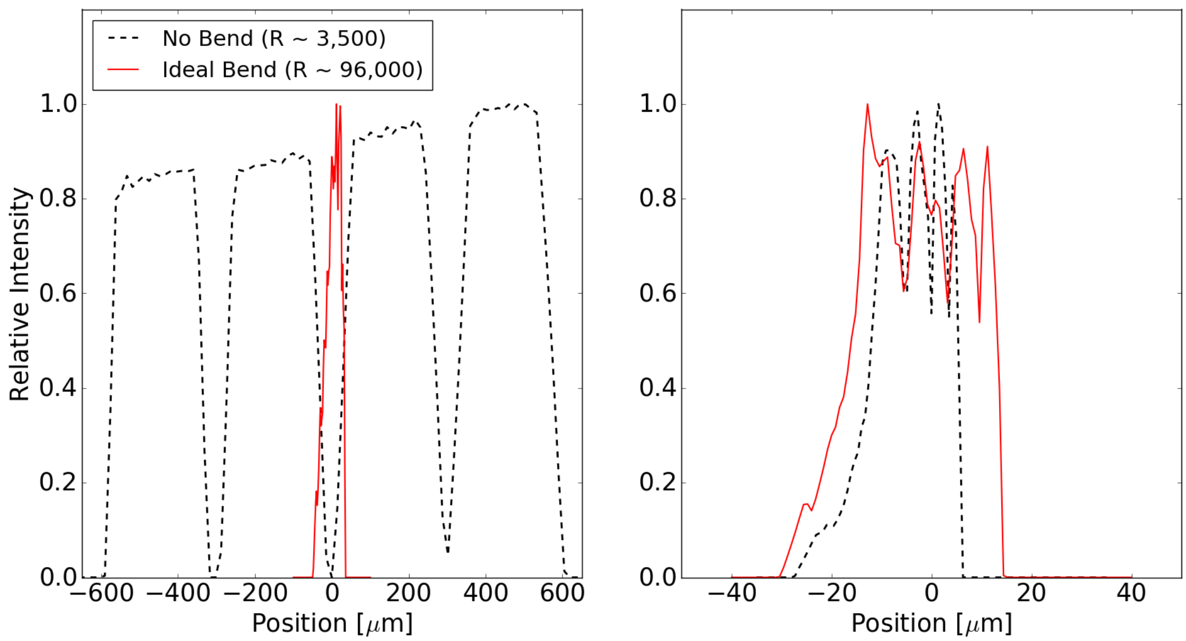

Figure 2.21: *Left:* The spectral LSFs predicted by Zemax of the CHESS instrument for the unbent echelle (black dashed line) and the Zemax optimized curved echelle (red line). *Right:* Same as left, but instead showing the order LSFs.

2.6.2 CHESS-4: Spectral Resolution Enhancement

After the initial alignment of the CHESS-4 payload using the flat echelle, we uninstalled the mount and the optic and began the process of inducing the resolution-enhancing curvature. To determine what shape was needed, we assumed a toroidal curvature and ran a damped least squares optimization within Zemax that minimized the overall spot radius on the detector at three different wavelengths: 1026, 1147, and 1400 Å. These wavelengths were chosen to favor the blue-end of the spectrum, since it contains the H_2 absorption features. Figure 2.21 shows a comparison of the LSFs between the unbent echelle and the Zemax optimized echelle bend, which was found to have R = 2.55×10^5 mm and ρ = -3.49×10^5 mm.

As discussed in §2.3.1, the curvature was induced in the optic by precisely torquing set screws along the surface and bottom edges. A Zygo GPI XP Fizeau Interferometer was used to measure the surface curvature for various combinations of screws and torque specifications, as applied to the previously described flight mount, with the goal of obtaining the best recreation of the Zemax prediction as possible. Torques were applied using a torque wrench that allowed for steps as small as 1 in. oz. Running these tests on the flight optic was not possible due to the sensitivity of its coating as well as the complications inherent to measuring a ruled surface interferometrically. Instead, we used an unruled replica of the echelle that was purchased from Richardson Gratings. With the unruled replica, we were able to measure the curvature across the entirety of the surface of the optic, allowing us to determine what torque specifications were needed to best recreate the results predicted by Zemax. We tested several configurations of set screws including using only set screws on the bottom, only using screws on the top, as well as applying a gradient of torques across the top set screws to match the desired curvature along the edge.

The set screw configuration that achieved the best results had four screws on top, one at each corner of the grating, that were torqued to 25 in. oz., and two set screws in the bottom holes that were torqued to 48 in. oz. The 2D surface profile of this configuration, as measured by the interferometer, is displayed in Figure 2.22. Also shown are two 1D surface profiles, demonstrating the curvature along the the two perpendicular red and blue lines plotted over the 2D profile. The assumption of circular curvatures across the measured optic is not perfect, as demonstrated by the widening of the red profile, but we quote approximate radii of curvature for each profile that can be used as a rough comparison to Zemax.

Using these newly determined torque specifications, we replaced the grating replica with the flight optic and reinstalled it in the payload. While our recreation of the Zemax curvature was close, it was not clear if that would produce the best spectrum once in the payload. Therefore, we ran a final optimization of the curvature using the full spectrum as a reference. The same procedure that was described in §2.6.1 was used to refocus the instrument each time a new torque specification was tested. To gain a better understanding of effect the top and bottom set screws had on the instrument LSF, we stepped through different torques on one set, while keeping the other set fixed. Figure 2.23 shows the focus curves for three

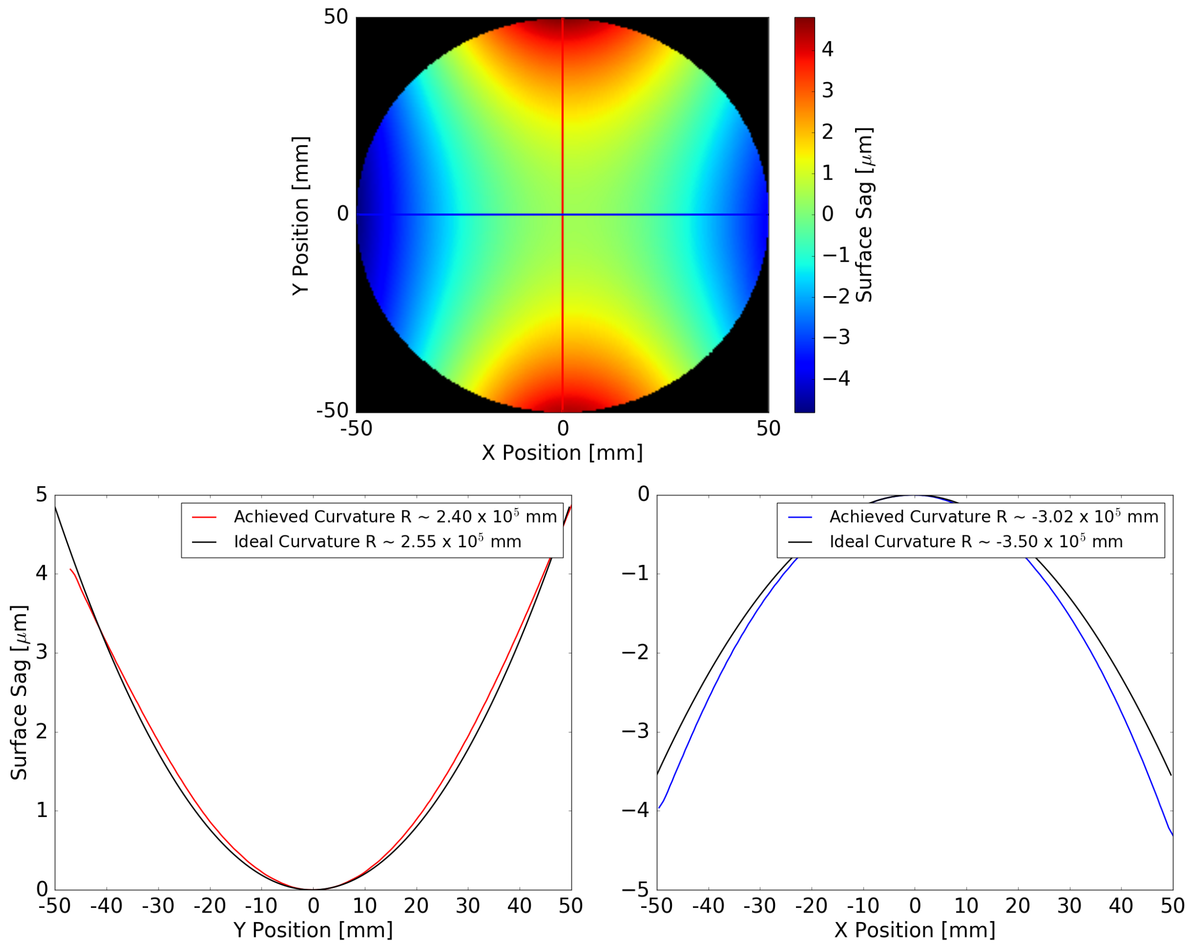

Figure 2.22: *Top:* The 2D surface profile of the unruled replica in the configuration that was the closest to the Zemax optimized result. The red and blue lines trace the paths of the 1D profiles shown in the lower plots. *Left:* The 1D profile running along the red vertical line in the top figure. *Right:* Same as left, but for the blue horizontal line in the top figure.

different torques on the top set screws. We found that, while increasing the amount of torque on the top screws drove the order and spectral focuses towards each other, it also created wider spectral features. This meant that having no torque applied to the top set screws gave the narrowest spectral features at the order focus.

Figure 2.23 also shows the focus curves when different torque values were applied to the bottom set screws. We again found that increasing the torque value drove the two foci together, but this time the larger torque tended to create wider orders. When taking these measurements, the top set screws were installed but loosened before the first measurement. After performing the first measurement with 52 in. oz. of torque on the bottom screws, we found that the top set screws became tight due to the optic pushing up against them. After loosening them and retorquing the bottom screws, we repeated the measurement at 52 in. oz. While this configuration resulted in generally wider orders, it did have the narrowest combined order and spectral feature width. Specifically, at about -7 mm we measured spectral features that were $\sim$150 μm wide while maintaining orders that were $<$130 μm. Since we expected further torquing the bottom set screws would make the orders too wide, we opted to stay with 52 in. oz. on the bottom set screws and no top set screws as our final flight configuration.

After the final position of the cross disperser was determined, the vacuum actuators were removed and the flight hardware was installed. This was done with the instrument aspect camera powered and aligned to a white light source in the long tank. The location of the spot was used as a guide as the actuators were removed to avoid moving the optic from its focused position. Once completed, long exposures using the arc lamp with H/Ar and with air were taken for a complete sampling of H, H_2, N, and O emission lines in the CHESS bandpass. These spectra were used to characterize the 1D extracted spectrum, define the wavelength solutions of the instrument, and determine the LSFs across the bandpass.

Figure 2.24 shows a side-by-side comparison of the CHESS-3 and CHESS-4 pre-flight echellograms. The improvement in the spectral focus is immediately apparent. In addition to

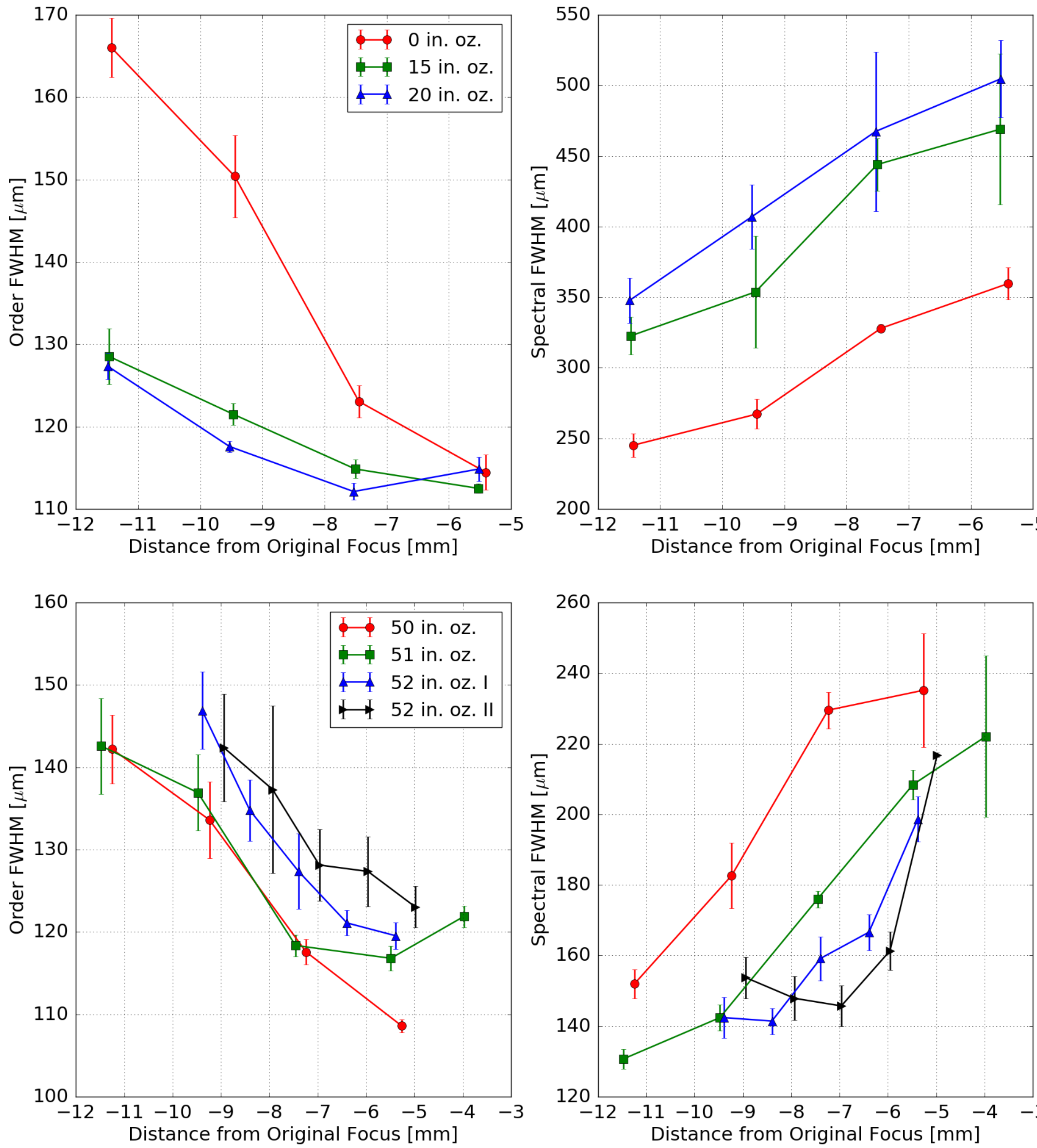

Figure 2.23: Focus curves of orders (left) and spectral features (right) as a function of cross disperser distance from the original focus of the instrument (*i.e.* when the flat echelle was installed). **Top:** The three curves represent the FWHMs measured when different torques were applied to the four set screws on the top of the optic, with the bottom set screws held fixed at 48 in. oz. **Bottom:** The four curves represent the FWHMs measured when different torques were applied to the two set screws on the bottom of the optic, with the top set screws loosened. Once reaching 52 in. oz. (blue triangles), we realized that the top set screws were still tight enough to have an impact on the curvature. After loosening them, we reran the focus curve at 52 in. oz. (black sideways triangles).

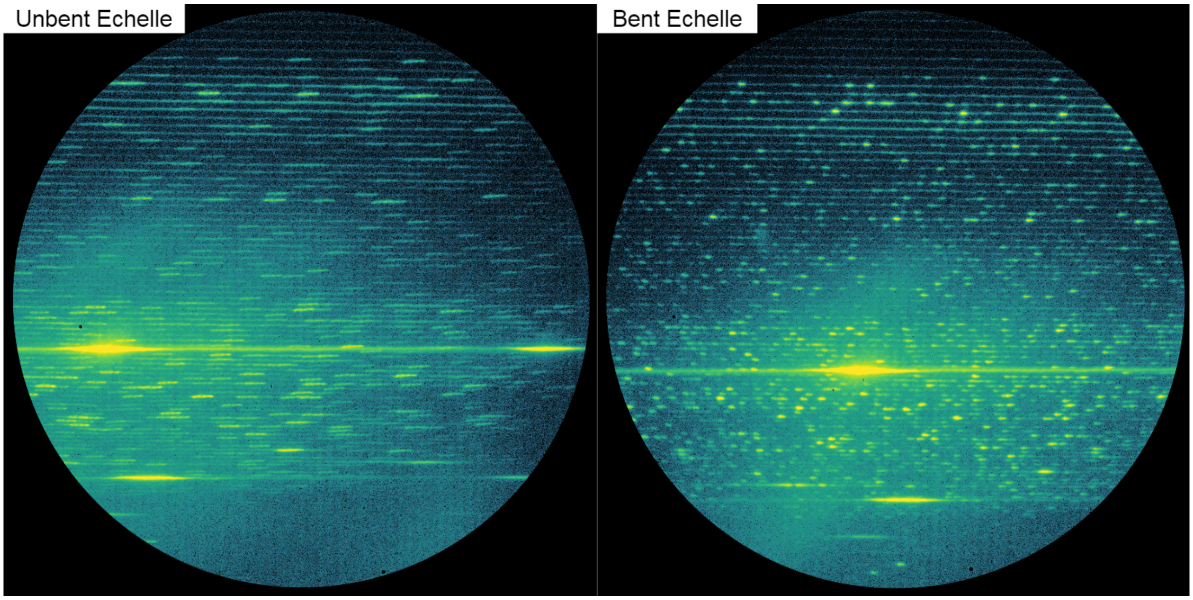

Figure 2.24: Raw images (trimmed for edge effects) of the CHESS-3 (May 2017, unbent echelle) and CHESS-4 (January 2018, bent echelle) echellograms. The brightest feature in both images is HI-Lyα (1215.7 Å). The other bright broad feature is HI-Lyβ (1025.7 Å). HI-Lyγ (972.5 Å) is visible below the Lyβ feature. The large shifts in the spectrum were made so that the peak of the echelle order was better centered on the detector. The narrower spectral features in the CHESS-4 echelleogram are the result of the shaped echelle grating providing additional focusing power to the system.

that, we repositioned the spectrum on the detector so that the peak echelle order was roughly centered. Both echellograms are co-additions of multiple exposures taken under vacuum. Each exposure was defined by how long we could run the full instrument configuration in vacuum without over-heating the electronics section, which typically lasted around 30 minutes. A large amount of scatter, that appears to be centered around Lyα, is seen in the spectra. We expect that this is a symptom of grazing incident reflections down the collimator tubes.

2.6.3 Creating a 1D Spectrum

Extracting the 1D spectra from the echellogram was accomplished through several steps. These steps were identical for CHESS-3 and CHESS-4, except where explicitly noted. The discussion assumes the coordinate system shown in Figure 2.4. First, the echellogram had to be rotated very slightly ($\theta < 1°$) to align the orders horizontally. The location of each order was then determined by summing (collapsing) all photon counts in the direction parallel to the orders (along the x-axis), which created an "order spectrum" with peaks where orders were present and troughs at inter-order pixels.

Once pixel locations and order widths were extracted, we collapsed a given order along the y-axis, creating a 1D spectrum of each order. Across a majority of the spectrum, neighboring orders overlap in wavelength space. Common spectral features between neighbors simplified the stitching together of orders. The grating equation (Equation 18) shows that $\Delta\lambda$ changes as a function of order, meaning that the number of pixels between two wavelengths will be different in neighboring orders. For CHESS-3, our resolution was low enough that we did not need to account for this stretching. While, for the higher resolution of CHESS-4, it was more apparent. In that case we accounted for the offset by scaling each order to be $0.94\times$ the length of its higher order neighbor. The 0.94 scale factor was determined through visual inspection.

We then identified two pairs of orders that contained strong overlapping emission features and used those to calculate a linear equation relating the amount of overlap to the average positions (in pixels) of the two neighboring orders. This equation was applied to the 88 identified orders to create a 1D spectrum in pixel space. Regions where orders overlapped were summed together. The amount of overlap decreased towards the red-end of the spectrum, as a result of the increased dispersion predicted by the grating equation. This, combined with the fact that the MCP is circular in format and thus a smaller fraction of each order was captured on the detector at the red-end of the echellogram, means that we did not fully sample the red-end of the spectrum. Due to the $\Delta\lambda$ scaling in the CHESS-4 data, the pixel values became too large towards the end of the spectrum that subsequent analysis became difficult. We mitigated this effect by taking the $\log_{0.94}$ of the entire 1D position array.

We used the composition of air through the arc lamp to map out well-known atomic lines and their corresponding line centers in our 1D spectrum. These lines were common enough that we could sample most of the CHESS wavelength space from ∼1000−1500 Å. To extend across the entire CHESS bandpass, we used the 1D spectrum generated using the H/Ar arc lamp echellogram to identify H_2 electron-impact lines at $\lambda > 1510$ Å. In total, we mapped the locations of 18 emission features between the air and H/Ar spectra. Using the known wavelengths of each of the emission features, we fit a 6^{th}-order polynomial to convert pixel position to wavelength across our 1D spectrum. The resulting wavelength solution for the pre-flight H/Ar calibration spectrum (from CHESS-4) is shown in Figure 2.25. Figure 2.26 displays a subsection of this spectrum along with a subsection of the pre-flight calibration spectrum from CHESS-3, demonstrating the improvement in the spectral LSFs that we achieved by introducing the shaped echelle.

2.6.4 Spectral Resolving Power Determination

Using these completed 1D spectra, we measured the resolving power of the instrument. To do this, we created a multi-Gaussian fitting routine to capture each emission feature. For CHESS-3, four Gaussians were required to adequately capture the entire feature. For CHESS-4, while the features were much narrower, they still typically required two Gaussians to adequately capture the entire shape. We defined the FWHM of an emission line by calculating the FWHM of each individual Gaussian and then measuring the distance between the center of the left hand peak minus its half width at half maximum (HWHM) to the center of the right hand peak plus its HWHM. The resulting width is used to calculate the resolving power of the spectral feature. Figure 2.27 shows the measured pre-flight R as a function of wavelength for both flights. We achieved an average R of 3,810 ± 152 for CHESS-3 and 13,859 ± 1,562 for CHESS-4. The CHESS-4 measurement was performed on data that were taken after the payload had been shipped to Wallops for preliminary integration. Prior to shipping, we did measure a larger average R of ∼18,000, but the shipping of the payload likely caused the shaped echelle to settle slightly. The R ∼ 14,000 better reflects the flight-like conditions and so we only provide those data here.

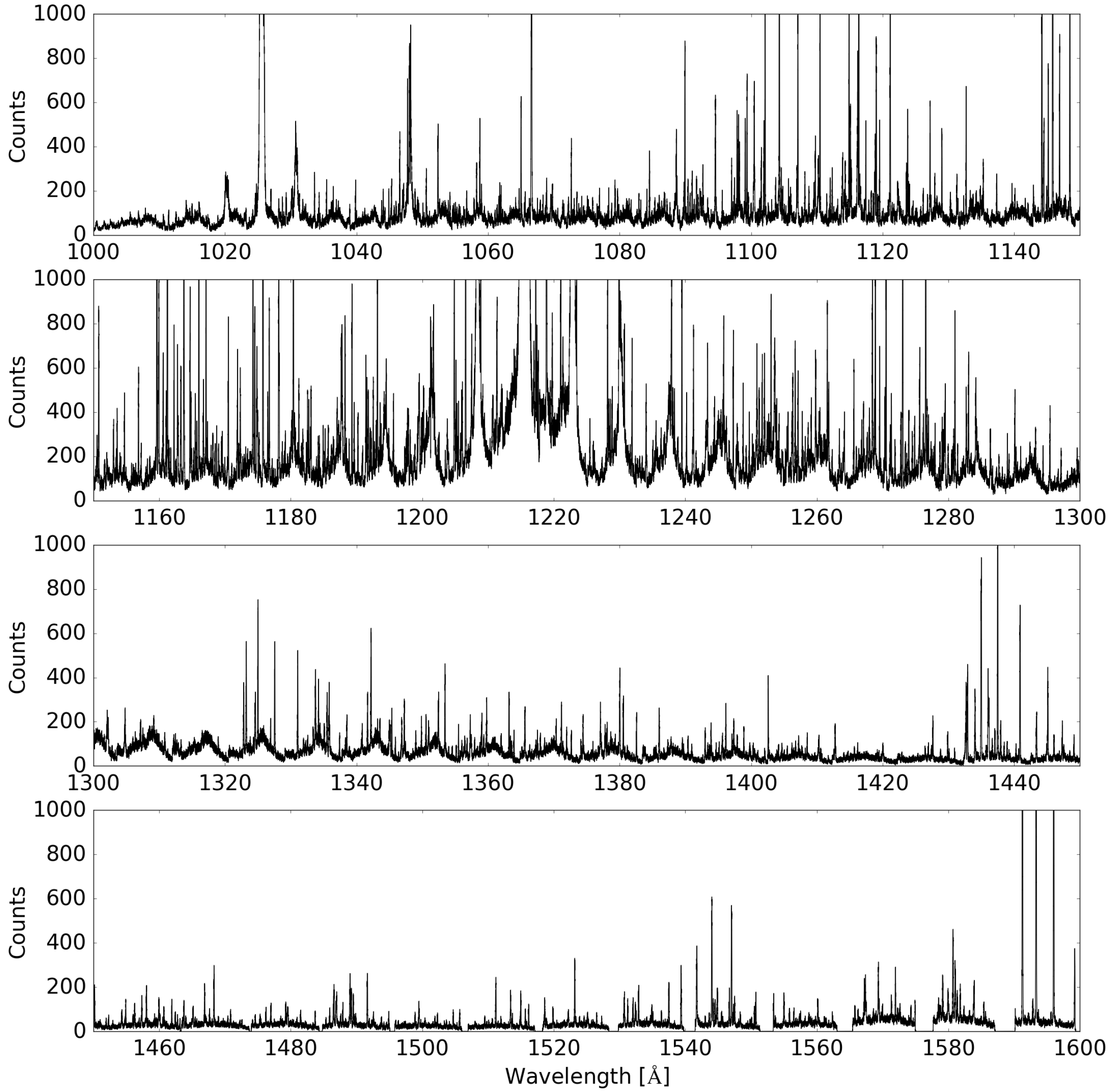

Figure 2.25: Complete first-order wavelength solution for the pre-flight CHESS-4 calibration spectrum, using H/Ar gas. As discussed in §2.6.3, neighboring orders no longer overlap starting around 1500 Å, resulting in gaps in the spectrum.

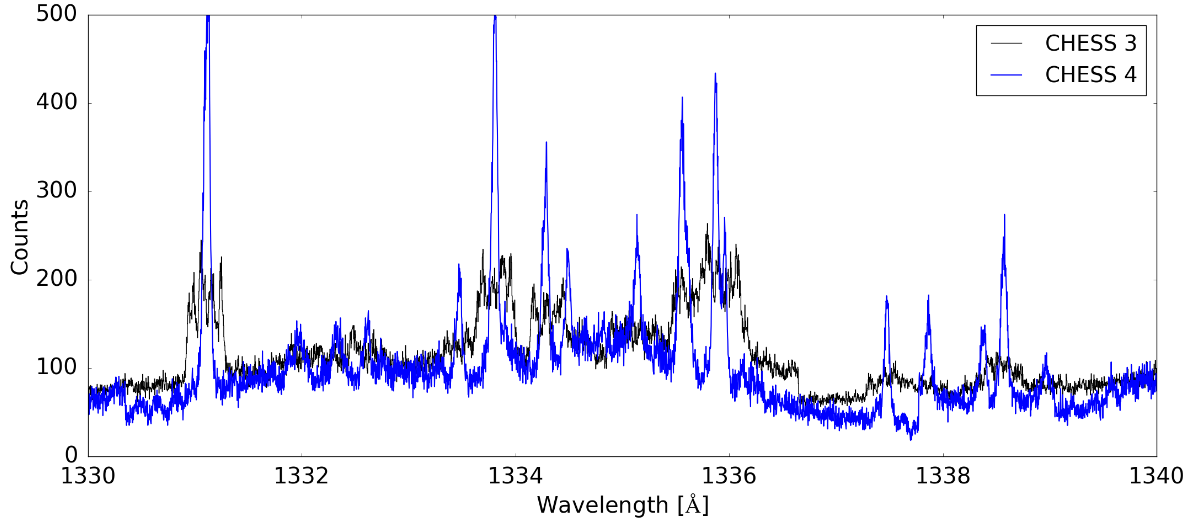

Figure 2.26: A comparison of the CHESS-3 pre-flight spectrum (black) and the CHESS-4 pre-flight spectrum (blue).

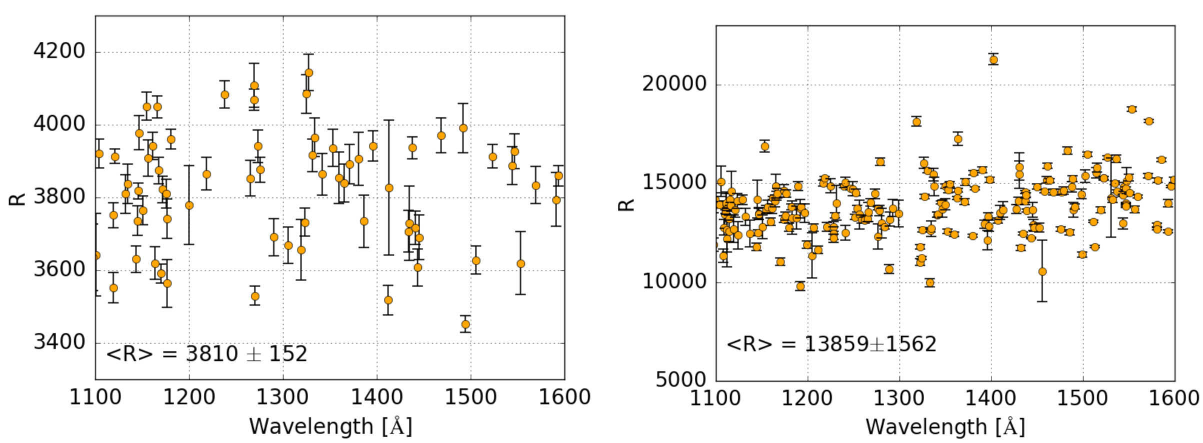

Figure 2.27: The average resolving power for CHESS-3 (Left) and CHESS-4 (Right). Each point comes from a line identified in the H/Ar calibration spectrum. The mean ($\langle R \rangle$) and standard deviation of the distribution is included in the lower left.

2.7 CHESS Flights

2.7.1 CHESS-3 Launch

CHESS-3 was brought to White Sands Missile Range (WSMR) in late May 2017 for field operations in preparation for launch. These operations involve various tests, including vibration, which required a means of tracking alignment shifts before launch. To do this, we fit a modified Bayard-Alpert tube lamp (McCandliss et al., 2000) with a small, collimating mirror and pinhole (100 μm) to the shutter door. This lamp produced an echellogram based off of the gas that was flown into it, similar to the previously described arc-lamp. The resulting spectral features (C, N, O, H, H_2) were used to confirm optical alignment at various stages of integration. An example spectrum is shown in Figure 2.28, in this case when air was used in the lamp. The collimating mirror was an off-axis parabola, which did not perform as well as the long tank, thus producing the large spots seen in the figure. The signal within the spots was strong enough that their position could be centroided as a coarse measurement of payload alignment.

CHESS-3 was launched aboard NASA mission 36.323 UG from White Sands Missile Range (WSMR) on 26 June 2017 at 11:10pm MDT using a two-stage Terrier/Black Brant IX vehicle. The mission was deemed a comprehensive success. A single uplink maneuver was needed to properly align the star to the optical axis, meaning that the instrument was able to integrate for $\sim$360 seconds on-target, with an approximate count rate of 190,000 photons/sec. After the 360 second exposure, we moved to an off-target calibration position where we took a 30 second long exposure to obtain a measurement of the background Lyα and O I airglow that contaminated our on-target spectrum.

From the beginning of the science exposure, we immediately saw photospheric and interstellar absorption features in the echellogram of β^1 Sco, the prominent features being Lyα, O I, and C III, as well as stellar continuum for orders with $\lambda > 1300$ Å. The interstellar features included Si III, N I, Si II, and H_2 complexes. Figure 2.29 shows the flight echello-

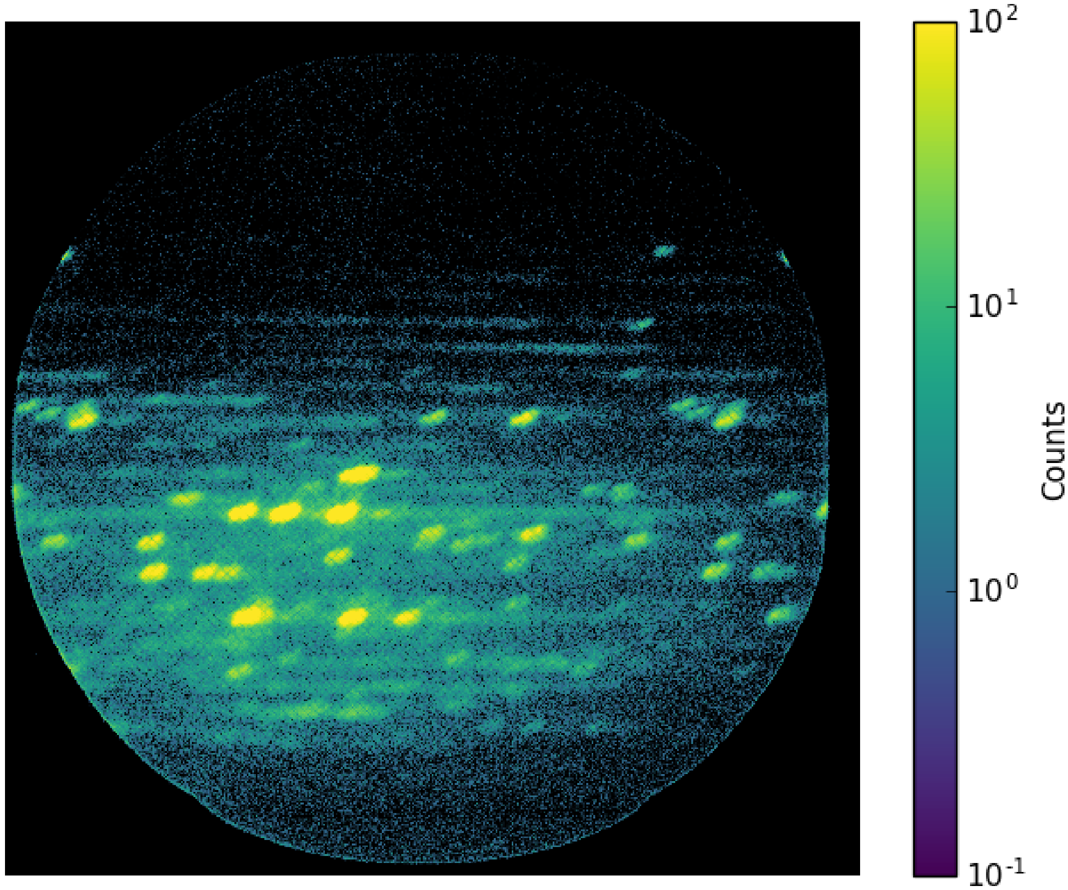

Figure 2.28: An example spectrum produced using the modified Bayard-Alpert tube lamp that was flowing air. Lyα, while present at just about the center of this spectrum, is no longer the brightest feature. Instead, the N triplet at 1199.6, 1200.2, and 1200.7 Å comprise the brightest lines in the spectrum.

gram with the scaled 30 second airglow spectrum subtracted out. The PMT also functioned as designed, showing ∼5500 counts/sec on target and ∼1000 counts/sec on the background target, indicating it could have been useful as an alignment check had the CCD flown.

2.7.2 CHESS-4 Launch

After a similar pre-launch integration phase as CHESS-3, CHESS-4 was launched aboard NASA mission 36.333 UG from the Reagan Test Site on Roi-Namur in the Republic of the Marshall Islands on 17 April 2018 at 4:47 am MHT using a two-stage Terrier/Black Brant IX vehicle. The mission was deemed a comprehensive success. A single uplink maneuver was needed to initially align the star to the optical axis and we were able to integrate for ∼300 seconds on-target, with an approximate count rate of 125,000 photons/sec. We again moved to an off-target calibration position to obtain a ∼40 second long background exposure.

Throughout the science exposure, we saw the star slowly drift across the aspect camera field of view (FOV), indicating that either our pointing was not stable or there was a component moving in our optical system. This motion was confirmed on our detector, where the location of the echelle orders moved as a function of time. The incoming photons are time-tagged and so we were able to correct for this drift post-flight. To do this, we binned the flight data as a function of time, using 5-second wide bins. At each time step, we created an order spectrum (see §2.6.3) that was then cross-correlated with a reference spectrum that was chosen to be a 5-second wide sample from the middle of the exposure. Using the measured offset, the order spectrum was shifted and then added into a new drift-corrected spectrum. This procedure was repeated for every time bin and the final dark-subtracted, drift-corrected spectrum is shown in Figure 2.30.

The payload splashed down approximately 170 miles north of Roi-Namur and all recovery systems functioned as designed. Due to rough seas at the impact site, the recovery ship was unable to immediately remove the payload from the water, instead towing it ∼50 miles to a calmer region where it could be brought aboard. Upon return to Roi-Namur, we found that

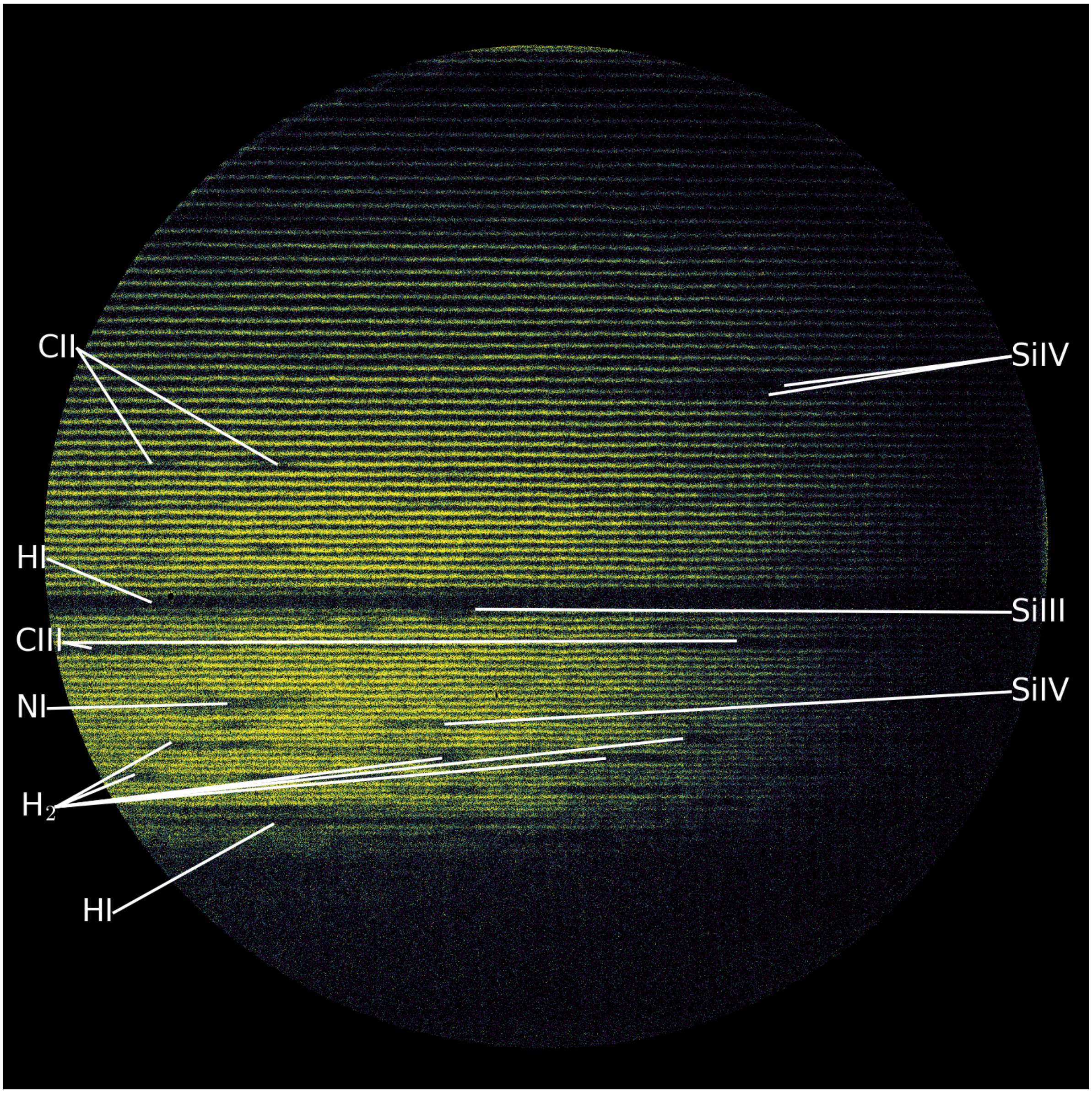

Figure 2.29: The science echellogram of β Sco after an exposure time of ~360 seconds, with the airglow spectrum subtracted out and detector edge effects trimmed. The echelle orders are stacked horizontally in the image, with order spectra easily distinguishable across most of the spectrum. This image has the same dispersion and cross-dispersion orientation as the calibration image (Figure 2.4). Several prominent absorption lines are labeled.

the instrument held at sub-atmospheric pressures and the watertight skins successfully kept the CHESS instrument and electronics section dry. The payload was purged with nitrogen and stored for shipping back to Colorado. Once returned to CU, the payload had leaked up to atmospheric pressure and several portions of it, including the butterfly valve and parts of the MCP electronics, were rusted from the sea water. Nonetheless, we found that the payload was still functioning, with no noticeable signs of degradation of the optics. The only issue was an observed fixed pattern noise being produced by the MCP, which we found was caused by a change in the detector voltage.

2.8 Flight Spectrum Synthesis

2.8.1 Background and Scatter Correction

The analysis of the flight data relied on the extraction routines that were developed using the pre-flight laboratory spectra, with a few additional steps to account for the inherent differences in the data sets. We first created science and background 2D spectra by trimming the time-tagged flight data at the corresponding intervals. A time average of the off-target sky count rate was used as our background level. It was multipled by the length of time we were on target and subtracted from the science spectrum. This step created the spectra shown in Figure 2.29 and 2.30.

Beyond accounting for the dark rate during the flight, it is necessary to correct for the contributions from the various sources of scatter within the system. The largest contributors of this stray light are from the imperfections in the echelle and cross disperser, electron spread from the MCP DQE grid, and scatter off the walls of the collimator tubes. Accounting for scatter in an echelle spectrograph has been a well studied topic, with a number of proposed solutions that vary in complexity and accuracy (see e.g., Bianchi & Bohlin 1984; Cardelli et al. 1990; Landsman & Bowers 1997; Howk & Sembach 2000; Valenti et al. 2003). Due to the limited observing time and resulting low signal-to-noise ratio (S/N) of the sounding rocket data, the implementation of many of these methods for the analysis of the CHESS

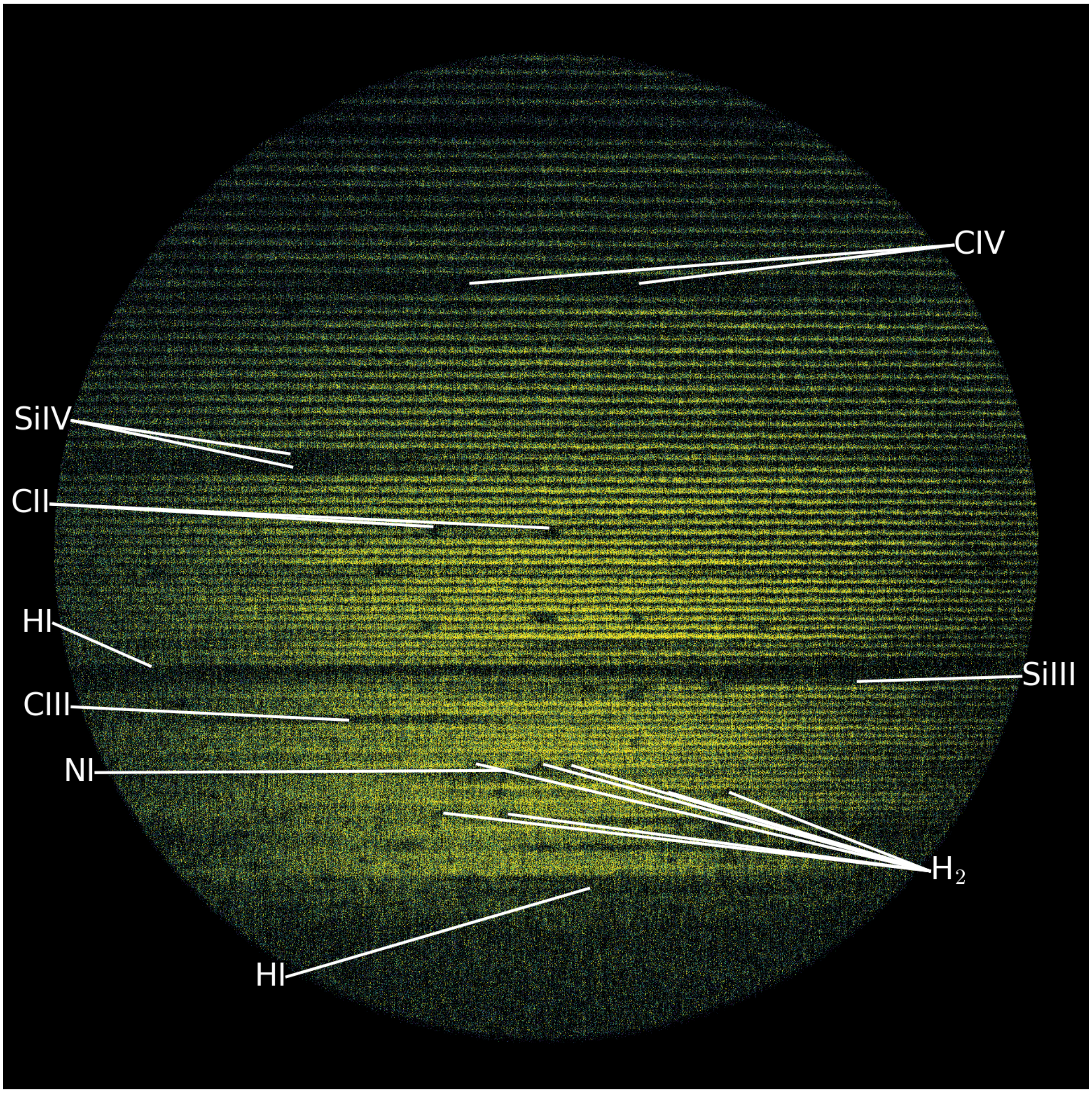

Figure 2.30: The science echellogram of γ Ara after an exposure time of $\sim$300 seconds, with the airglow spectrum subtracted out, detector edge effects trimmed, and the previously described correction to the in-flight drift applied. The echelle orders are stacked horizontally in the image, with order spectra easily distinguishable across most of the spectrum. This image has the same dispersion and cross-dispersion orientation as the calibration image (Figure 2.4). Several prominent absorption lines are labeled.

data was hampered by the magnitude of the statistical variations and the lack of available off-order pixels towards the blue end of the spectrum.

As an example of this, for CHESS-3 we implemented a procedure similar to the one described by Howk & Sembach (2000). For clarity in this discussion, we will use the spectrum orientation shown in Figure 2.4, with the spectral direction running along the y-axis and the order direction running along the x-axis. In the Howk & Sembach (2000) method, the scatter is assumed to be dominantd by local effects (such as PSF broadening) and the amount of scatter in a given order is measured by first subtracting a bulk background term and then fitting a 7^{th}-order polynomial to interpolate from the off-order background across the order itself (i.e. along the y-axis). This was done for every pixel along the x-axis in each order. In our utilization of this procedure, we found that the blue end of the spectrum had regions with as few as two inter-order pixels. This limited the quality of the measurement due to the small sample size and the fact that we could only interpolate using a 1^{st}-order polynomial. We mitigated this issue slightly by smoothing the inter-order regions using a 40-pixel wide box car, which helped reduce the variability.

With these limitations in mind, we attempted the procedure, and the resulting continuum normalized spectrum can be seen plotted in blue in Figure 2.31, where we can tell by eye that the background levels have been overestimated. Specifically, the background subtraction produced (1-0) and (0-0) band H_2 absorption lines that had normalized fluxes approaching zero in the line cores. Values that low would not occur at the expected column density of the sight line, given the R $\sim$ 3,500 of the instrument. This is supported by Valenti et al. (2003), who showed that this 1-D approached tended to overestimate background levels. In light of that result, we expect that the local scatter effects in the CHESS-3 spectrum are not well represented by the linear fall off and the sample size of the inter-order pixels is too small to explore more complex options. In addition to this, we want to avoid the situation of biasing our results towards an answer that we expect. This means that using the final depths of the absorption cores as a guide for the accuracy of our result can be a slippery slope. We do

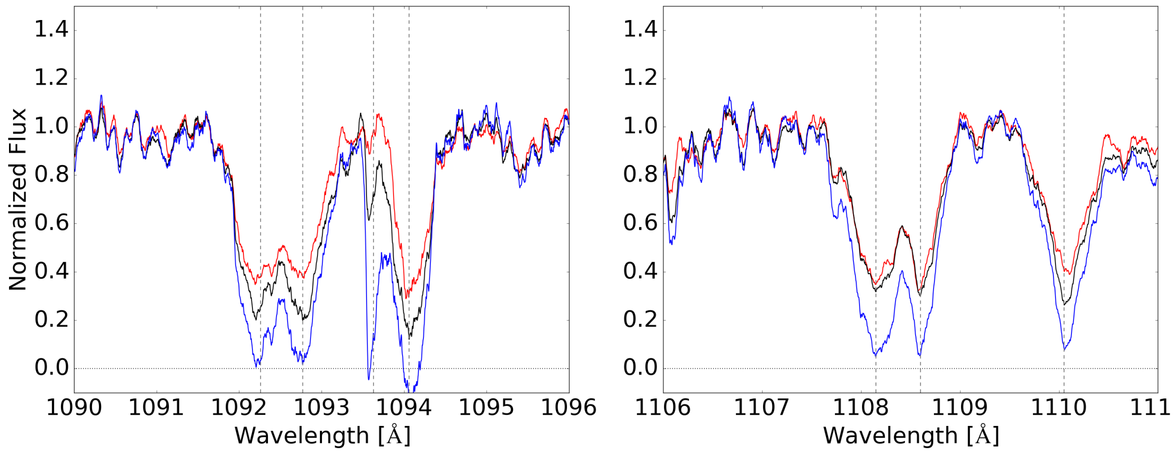

Figure 2.31: Continuum normalized spectra of β Sco (1-0) and (0-0) band H_2 absorption lines, using different background subtraction methods. In red is the spectrum with only the dark rate subtracted. In black is the spectrum when the Lyα absorption level of the background is subtracted. In blue is the spectrum using the Howk & Sembach (2000)-style interpolation across the background. Vertical dashed lines are plotted at notable H_2 absorption features.

not want to start the analysis under the assumption that past observations were correct and test background subtraction methods that get us as close to those results as possible.

Instead of iterating on fits to the inter-order pixels, we opted for a more global solution by measuring the amount of light in an absorption region that is expected to contain zero counts and using that as the amount of scatter contained in any given order. The region we choose for this calculation was Lyα, since its absorption trough spans the entirety of the x-axis. We created a 1D background spectrum by averaging the central five pixels (along y) of the Lyα order together at each x position and then smoothing the profile using a 20-pixel wide box car. The resulting spectrum was subtracted from each individual row of each order before the 1D spectrum was generated. We expect that this background subtraction measurement would, if anything, underestimate the true background level, given that the neighboring orders around Lyα are dimmer (so there would be a smaller local scatter contribution from them) and that the order itself is dim (so there would be less internal scatter). A subsection of the Lyα-background subtracted spectrum is shown in Figure 2.31. The line depths appeared, by eye, to make sense physically so we opted to move forward with this analysis.

This solution was complicated in the CHESS-4 case due to the smearing of orders on the blue-end of the spectrum. Unlike in CHESS-3, the contribution to the scatter from the neighboring orders was not as negligible of an effect and so only subtracting the Lyα absorption trough resulted in a spectrum with lines that were too shallow. To account for this additional term, we used a process similar to the one we initially attempted for CHESS-3, but this time we relied on the shape of the neighboring orders to determine the amount of scatter. We first identified a strongly absorbed feature on the blue-end of the 2D spectrum and extracted the 1D order plot in the region around that line. We then fit the edges of the neighboring orders down into the heavily absorbed order, giving us the shape of the order fall-off without contamination from the order of interest. We fit the edge of each of the neighboring orders with a line, which was chosen because a more complex functional form was unable to be determined from the quality of the data. The resulting lines are used as "template profiles" to correct for scatter at each pixel along the x-axis of each order, scaling the templates by the ratio of peak counts in the new neighboring order to peak counts in the template order. Figure 2.33 shows these template lines plotted over the orders that were used to construct them as well as what they look like when scaled to a new set of orders.

2.8.2 Profile Fitting

Once the scatter was accounted for, each echelle order was extracted following the process described in 2.6.3. While our goal is to find N(H_2), our procedure works by modeling τ, therefore we must divide by the solar continuum (see Equation 12) before we can perform the analysis. To do this, we manually went through each echelle order and hand selected points that appeared to be free of any absorption. We then used a spline interpolation to generate a smooth curve that spanned the entire order. An example of this is shown in Figure 2.32. Since all of the H_2 absorption features are located within $\lambda < 1150$ Å, we only fit orders that were within that wavelength limit. Following the creation of the continuum, the remainder of the 1D spectrum construction process was followed, using the

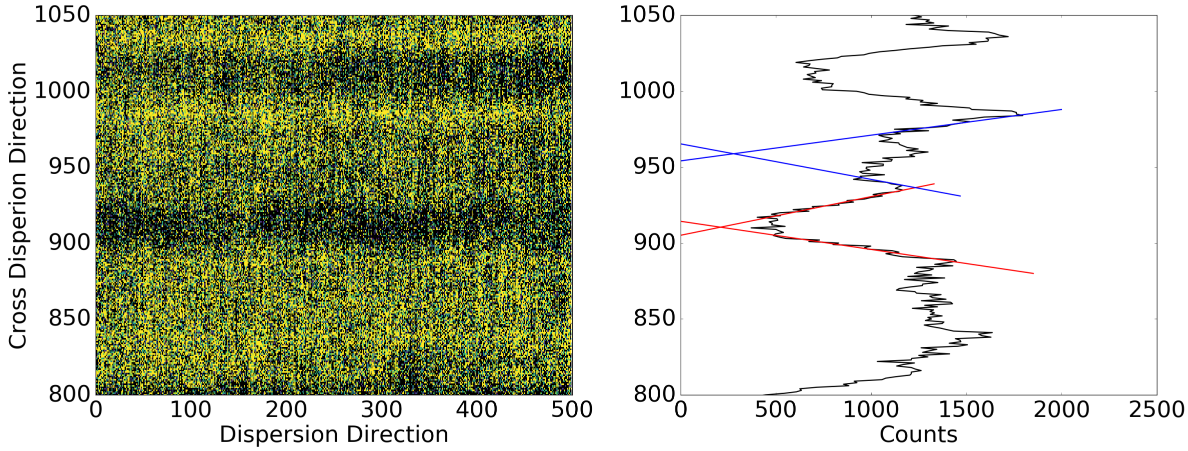

Figure 2.32: A demonstration of the neighboring order contamination correction that was applied to the CHESS-4 γ Ara data. *Left:* The subsection of the 2D spectrum used to create the order plot shown on the right. The absorption feature used to generate the template lines is located at y $\sim$ 910. *Right:* The order plot used to generate the template lines, which are shown in red on the orders they were derived from. In blue are the same lines, scaled and translated to fit those new orders, demonstrating their use in measuring the amount of light contributed to an order by its neighbors.

pre-flight spectrum-calculated order overlap and wavelengths solutions, to build the final science spectra. These spectra can be seen in Figure 2.34 for CHESS-3 and Figure 2.35 for CHESS-4. Once completed, the spectrum was normalized using the constructed continuum.

Modeling of the H_2 absorption features was done using the *H2ools* optical depth templates (McCandliss, 2003). These templates are calculated for integer values of b = 2–20 km s^{-1}, J$''$ = 0–15, v$'$ = 0–18 (for the Lyman band), and v$''$ = 0–3 and they are useful for N(H_2) $\lesssim 10^{21}$ cm^2. We expect $b > 12$ km s^{-1} to be unphysically large for the sightlines analyzed in this work so, to minimize the possible parameter space, we set an upper limit on b at that value. To allow for non-integer b values, we performed a weighted average of the templates above and below the non-interger value, where the weight was determined using 1 - $\mid b_{\rm int}$ - $b_{\rm non-int} \mid$.

The column densities for J$''$ > 7 were expected to be smaller than the uncertainities in the observations and so we only modeled, at most, up to N(J$''$ = 7). This decision is supported by our measured uncertainites in even the J$''$ = 6 and 7 column densities (see,

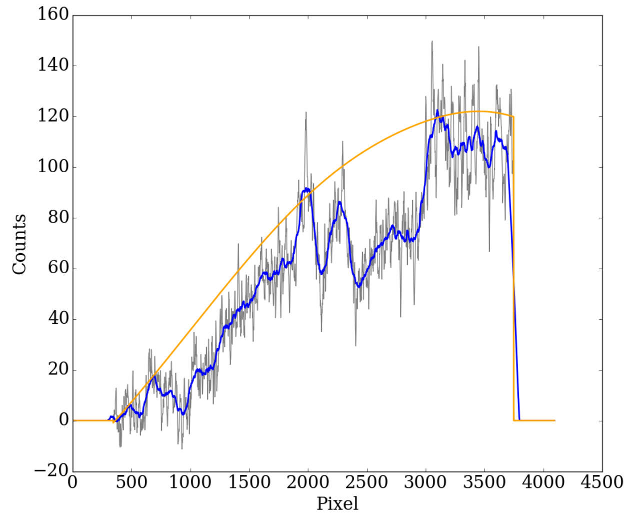

Figure 2.33: An example order from the CHESS-3 flight data, showing the raw data smoothed by an 8-pixel wide boxcar in gray. The same data are shown smoothed by a 100-pixel wide boxcar is shown in blue. Finally, the spline interpolated continuum from the order is plotted in orange.

e.g. Figure 3.2 in §3.1.1). To avoid contamination from the Werner transitions, we restrict our fitting routine to the (0-0) to (4-0) Lyman bands. This restriction is imposed by limiting the bandpass to $\lambda\lambda$ 1046–1120 Å, in general. For γ Ara, where we expect a rovibrationally excited population of H_2 along the sightline, we would also look for transitions in the (0-1) to (4-1) bands. Our preliminary analysis did not find any signs of these features, although we note that the S/N may have contributed to the lack of a detection.

Our code accepted an initial guess for N(J$''$ = 0–7) and b and, using the SciPy curve_fit routine, performed a least squares minimization between our observed spectrum and a convolution of the *H2ools* templates and our expected instrument profile. For CHESS-3, we used an R = 3,800 Guassian for the instrument profile. For CHESS-4 this was updated to R = 13,900. Known stellar and ISM absorption features can contaminate the spectrum and are especially problematic when near the H_2 features. We masked the more predominant of these features before performing the analysis, using Pellerin et al. (2002) as a guide to identify the lines. The resulting N(J$''$) values were fed back into the template and instrument convolution to generate a model spectrum. The column densities were further used to

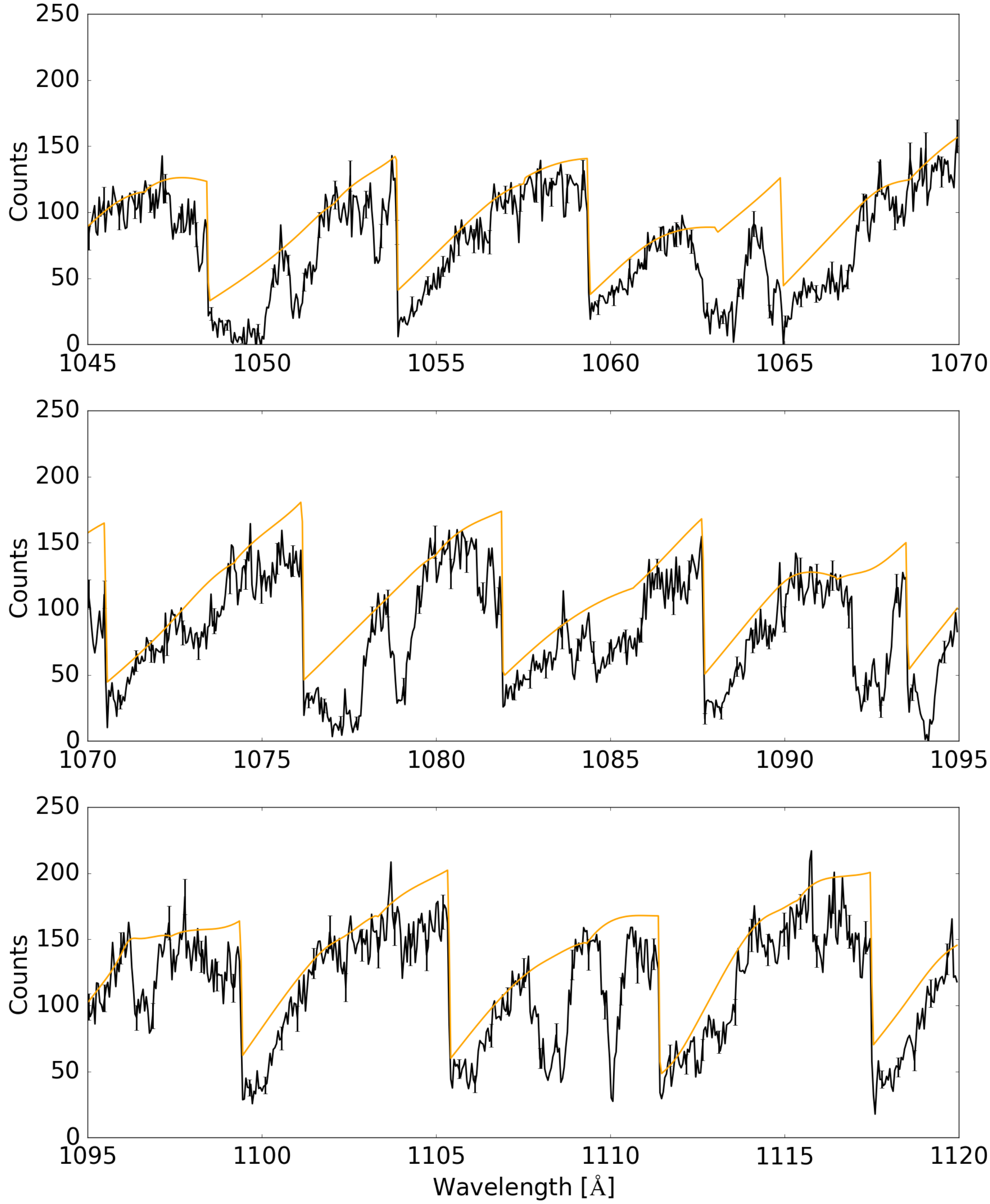

Figure 2.34: The background subtracted 1D flight spectrum of β Sco, plotted in black. Our constructed continuum is overplotted in orange.

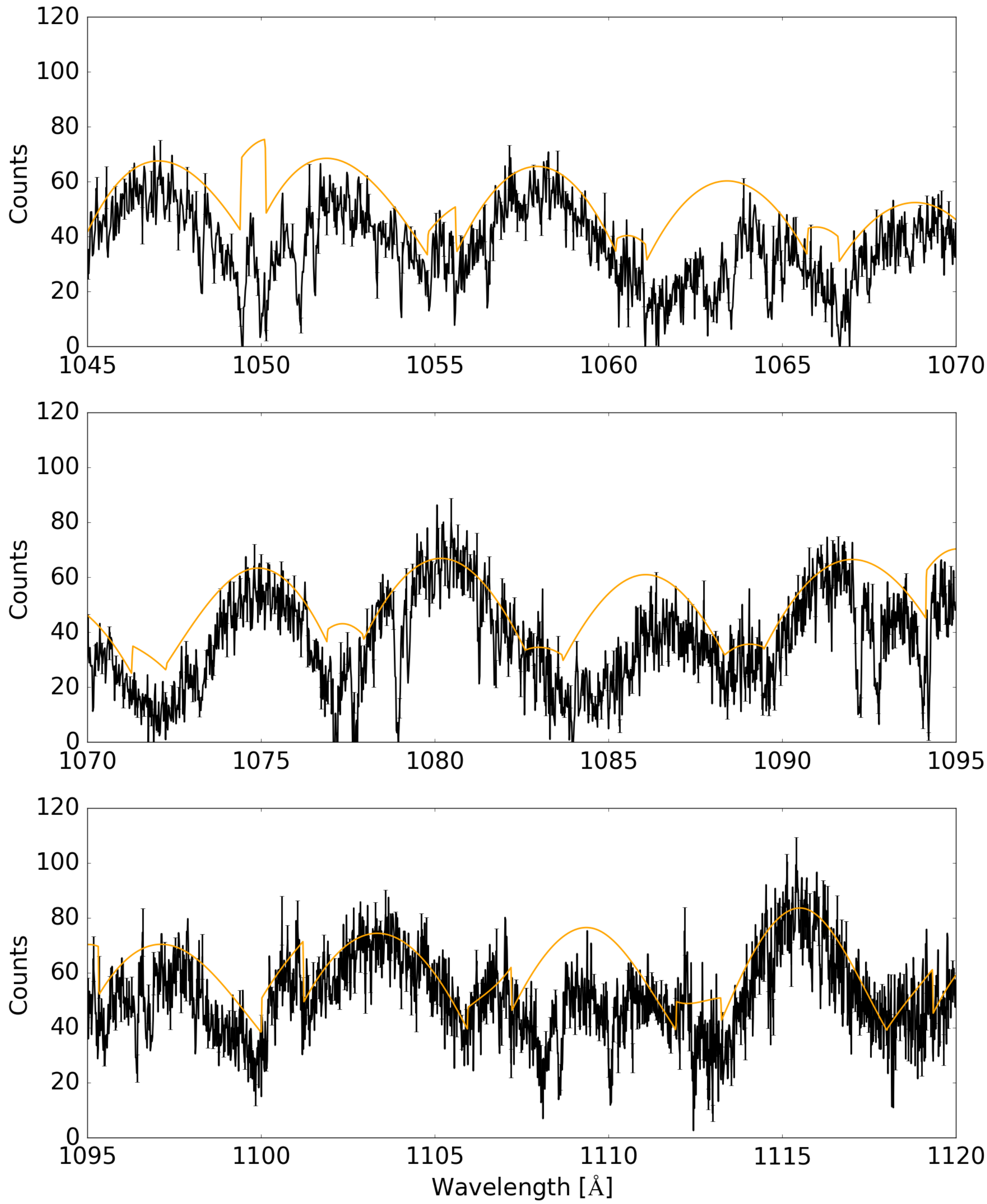

Figure 2.35: The background subtracted 1D flight spectrum of γ Ara, plotted in black. Our constructed continuum is overplotted in orange. The larger deviations from the spectrum (e.g. near 1050, 1063 and 1085 Å) occur at locations of known absorption features that required us to estimate the continuum level to adequately capture the absorption.

calculated T_{01} and T_{exc} along the sightline.

3 Science

3.1 β Sco

3.1.1 CHESS result

Figure 3.1 shows the continuum normalized flight spectrum of β Sco over the bandpass of interest for H_2 absorption features. Overplotted in orange is the model absorption profile that was found by fitting the H_2 features. The final spectrum has been binned down to d$\lambda \sim 0.06$ Å per bin, which is about 5 bins per resolution element. A summary of the fit parameters are listed in Table 6.

There are several different error contributions to the column density that, for clarity, we will name separately. The first error is the photometric uncertainty, which we will refer to as $\sigma_{\rm phot}$. The fitting routine, which accounts for $\sigma_{\rm phot}$, returns uncertainties in the resulting modeled values. We will refer to this error as $\sigma_{\rm fit}$. Finally, there is an error associated with our continuum placement. While we try to construct the continuum by bisecting the flux measurements in unabsorbed portions of the spectrum, the physical continuum level could really be within $\pm$ $1\sigma_{\rm phot}$. To quantify the effect of this uncertainty, we repeat the fitting procedure on the spectra that are produced when the continuum is moved $\pm$ $1\sigma_{\rm phot}$. The average $1\sigma_{\rm phot}$ level was determined by calculating the standard deviation of a representative unabsorbed portion of the spectrum, and was found to be ~0.1 in normalized flux units. $\sigma_{\rm cont}$ is then equal to the differences in the measured column densities and b values found at the raised and lowered continuum positions. $\sigma_{\rm cont}$ is a conservative estimate of the error in b and N because it maximizes the uncertainty in the continuum. It is statistically unlikely (ignoring unidentified systematics) that our continuum placement was consistently $1\sigma_{\rm phot}$ high/low across the entire bandpass and, therefore, seeing what values are produced in those

b [km s^{-1}]	$\log_{10}$N(H_2) [$\log_{10}$ cm^{-2}]	$\log_{10}$N(0) [$\log_{10}$ cm^{-2}]	$\log_{10}$N(1) [$\log_{10}$ cm^{-2}]	$\log_{10}$N(2) [$\log_{10}$ cm^{-2}]	$\log_{10}$N(3) [$\log_{10}$ cm^{-2}]
$\leq$2	$19.71^{+0.17}_{-0.16}$	$19.50^{+0.17}_{-0.15}$	$19.17^{+0.07}_{-0.08}$	$18.12^{+0.11}_{-0.27}$	$18.37^{+0.43}_{-2.10}$

$\log_{10}$N(4) [$\log_{10}$ cm^{-2}]	$\log_{10}$N(5) [$\log_{10}$ cm^{-2}]	$\log_{10}$N(6) [$\log_{10}$ cm^{-2}]	$\log_{10}$N(7) [$\log_{10}$ cm^{-2}]	T_{01} [K]	T_{exc} [K]
$17.81^{+0.52}_{-2.53}$	$17.60^{+0.14}_{-1.12}$	$16.78^{+0.87}_{-6.78}$	$17.19^{+0.45}_{-7.19}$	57 $\pm$ 11	607 $\pm$ 400

Table 6: CHESS-3 β Sco fit results

limits gives the largest possible change in b and N. In practice, we indeed found that σ_{cont} was the largest of the measured uncertainties and so we use those values as our quoted errors. The errors on T_{01} and T_{exc} were also found by differencing the values found at $\pm$ 1σ_{cont} and adopting the largest value.

Figure 3.2 shows the excitation diagram for our modeled spectrum. The column densities reproduce well the expected two temperature populations discussed in §1.6, with a low temperature T_{01} = 57 $\pm$ 11 K calculated using N(J'' = 0–1) and a higher temperature T_{exc} = 600 $\pm$ 100 K. Additional uncertainties on N($J'' \gtrsim 3$) and T_{exc} that are not reflected in our error calculation come from the limitations placed on b in our fitting routine. The first issue comes from the boundaries imposed by the *H2ools* templates, which span b = 2–12 km s^{-1}. The b value produced by our fitting routine equaled 2 km s^{-1} indicating that the true b value could be lower. This would impact the higher J'' column densities that lie close to or on the flat portion of the curve of growth, since a lower b favors larger N(J''). The second issue is that our model assumes a single b value for all J'' states. Previous observations have shown evidence in support of an increasing b with J'' (Spitzer & Cochran, 1973; Jenkins & Peimbert, 1997; Lacour et al., 2005), although the trend has not been seen along all sightlines (Jenkins et al., 2000). Therefore, a systematic error in our N(J'') measurements could exist for the larger J'' levels.

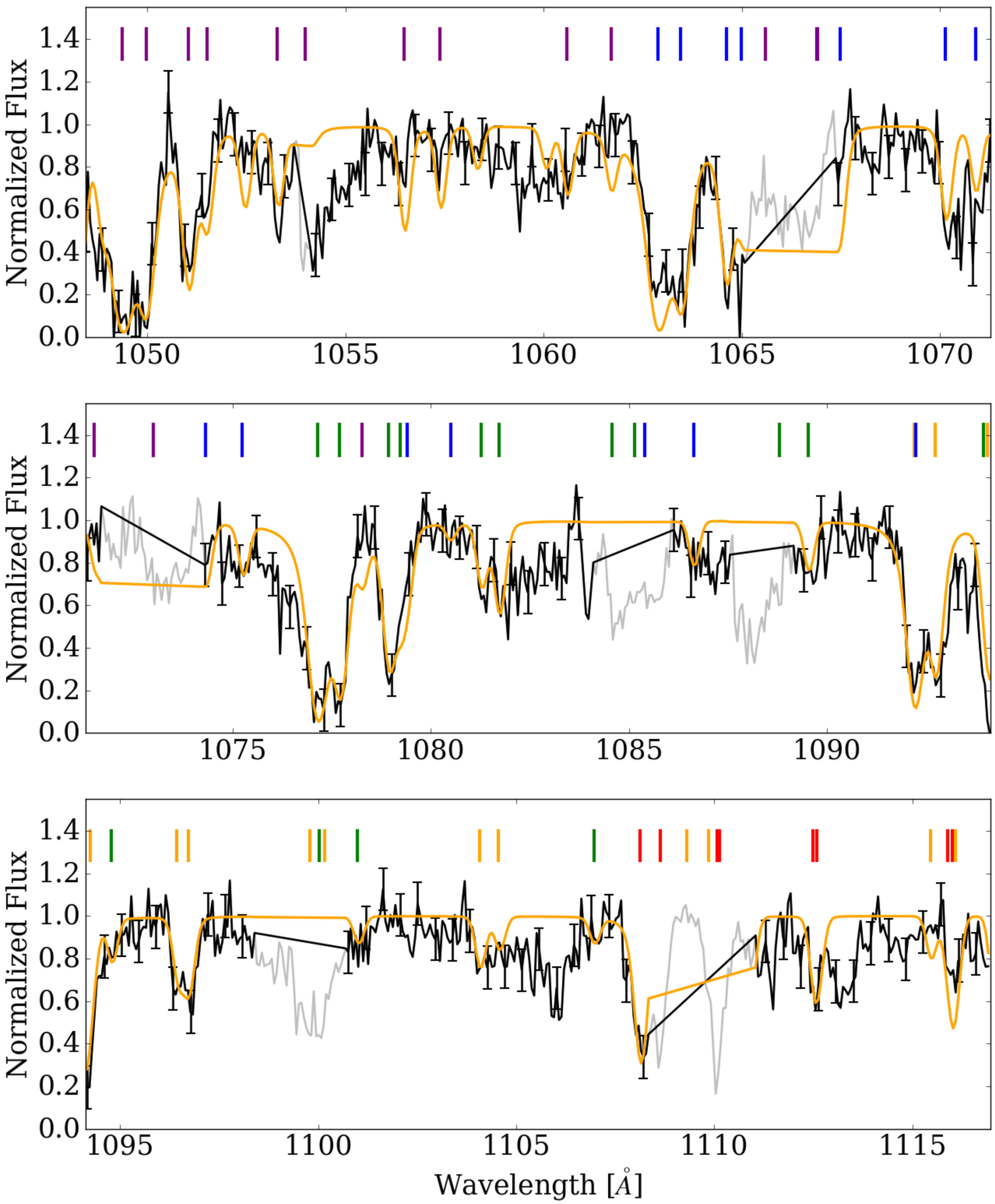

Figure 3.1: The extracted 1D flight spectrum for β Sco, plotted in black, with our model overplotted in orange. Regions of the spectrum that were masked are plotted in gray. The vertical ticks indicate the positions of the H_2 absorption features, up to $J'' = 7$, from the following vibration bands: v'-v'' = 0-0 (red), 1-0 (orange), 2-0 (green), 3-0 (blue), and 4-0 (purple).

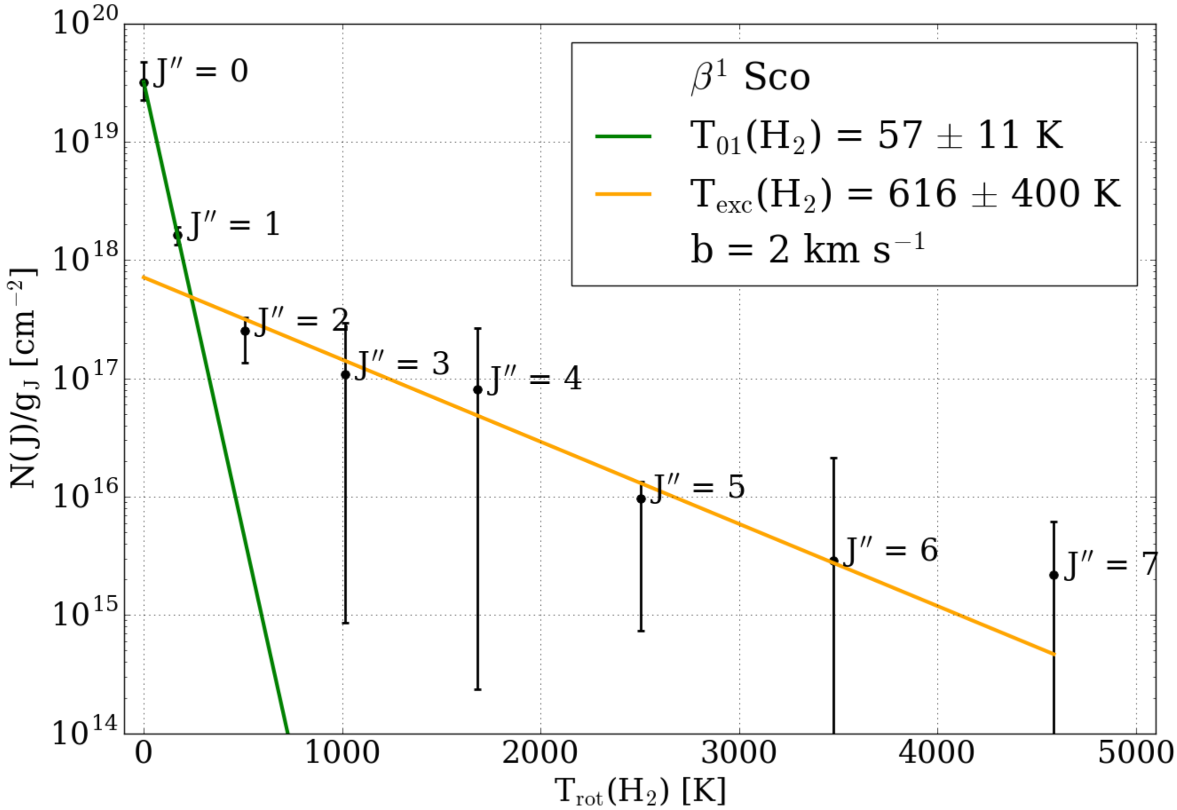

Figure 3.2: H_2 excitation diagram derived from our spectral profile fitting of β Sco using rotational levels J″ = 0–7. Our calculated T_{01} and T_{exc} are listed in the legend. Their corresponding lines are plotted in green (for T_{01}) and orange (for T_{exc}).

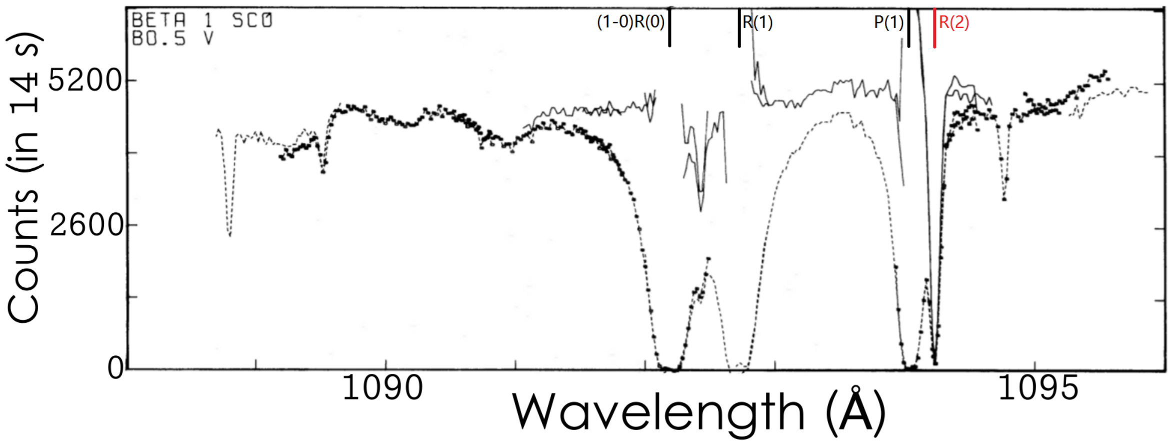

Figure 3.3: β Sco spectrum from Savage et al. (1977). Data that are free of stray light contamination is plotted as data points over the dashed line. For data with stray-light contamination (i.e. where the U2 mirror could not block the vent hole), only a dashed line is plotted. The best fit reconstruction is shown as a solid line. Axis labels and H_2 lines of interest have been edited by N. Kruczek to improve clarity.

3.1.2 Comparison to Savage et al. (1977)

Savage et al. (1977) (S77; hereafter) used the U1 channel of the *Copernicus* satellite (§1.7.2) to measure N(0) and N(1) along the line of sight to β Sco. After correcting for wavelength offsets and scatter, they derived the column densities by dividing the observed spectrum by predicted line shapes that were functions of column density. The best fit was determined by the column densities that best canceled out the absorption features. Their resulting fit for β Sco is shown in Figure 3.3, where they measured $\log_{10}$N(0) = 19.46 and $\log_{10}$N(1) = 19.58 with a log error of $\pm$0.06 for each value. This result agrees well with our CHESS analysis for N(0) but our N(1) values disagree by $\sim$0.4 dex.

Apart from the host of uncertainties inherent to both data sets, a potential source for this discrepancy comes from the fact that S77 only used three lines: (1-0)R(0), (1-0)R(1), and (1-0)P(1), to make their measurement. While they state that one must acknowledge the existence of the (1-0)R(2) line, which partially overlaps with P(1), it is unclear what, if any, measures were taken to account for it. This means that their results may have favored larger N(1) values, since a larger column density would better account for some of the absorption produced by the R(2) line. To explore this further, we reproduce the analysis of S77 but use the CHESS fitting routine to model the column densities and compare the results when R(2) is and is not included.

A number of initial steps were taken to recreate the β Sco spectrum seen in Figure 3.3. Two separate scans generated a bulk of the spectrum, with a third that just covered the $\lambda <$ 1090 Å portion. This third scan was not used in a significant capacity within this analysis, and so we will not discuss it here. For the two primary scans, one (Scan A; hereafter) covered two separate wavelength regions; $\lambda\lambda$1090.10–1092.45 and $\lambda\lambda$1093.83–1095.13 Å, and the second (Scan B; hereafter) covered the central $\lambda\lambda$1091.93–1094.6 Å. These two scans were necessary to fully sample the absorption features of interest since, to observe the central portion of Scan B, the instrument was aligned in such a way that a vent hole allowed stray light to reach the detector, introducing another background source (Rogerson et al., 1973).

Unlike the CHESS data, the higher resolution of *Copernicus* produces H_2 absorption features that are expected to reach zero. Using that fact, the zero count level of each scan was determined using the cores of the R(0) and R(1) lines, following the procedure of S77. The wavelength zero points of the two scans were separately adjusted so that they were aligned at the line centers of each absorption feature. The zero count level of Scan B was further adjusted so that the continuum levels at $\lambda >$ 1093.83 Å agreed between the two scans. The above procedure was tweaked in an effort to produce a spectrum that was as close to Figure 3.3 as possible. Our resulting recreation is shown in Figure 3.4. The complete spectrum was generated by averaging any overlapping regions between the two scans, and the continuum was created using a linear fit between the regions of peak counts on either side of the absorption features.

The continuum normalized spectrum of β Sco was fit using the CHESS analysis code. The instrument profile used in the convolution was a Gaussian with a FWHM of 0.051 Å (Drake et al., 1976). S77 mentions using a "flat-top Gaussian", but insufficient detail is provided on the width of the flat portion. Given the stellar source profile shown in Figure 1

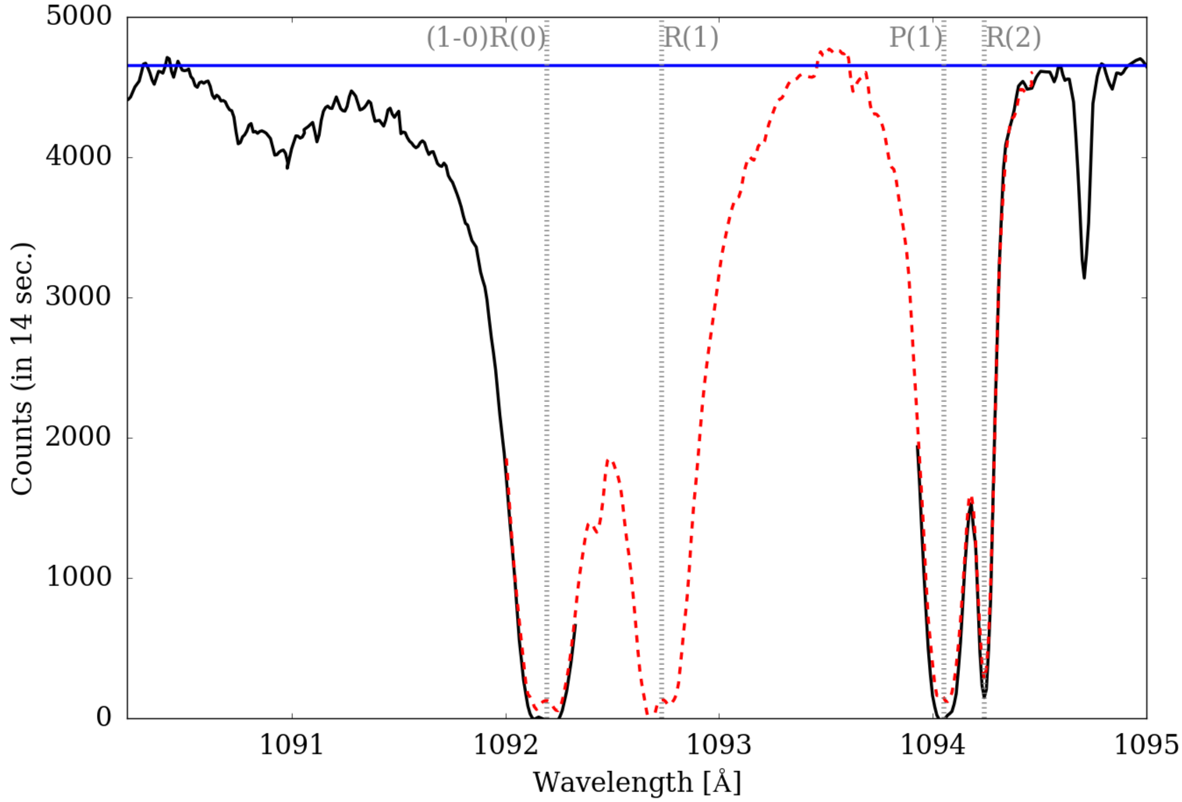

Figure 3.4: The background and wavelength solution corrected scans of β Sco produced from the *Copernicus* data. The solid black line is Scan A, which does not cover the stray light region of the instrument. The red dashed line is Scan B, which originally contains an additional contribution from stray light. Corrections to the spectra were made to bring them into general agreement with the spectrum produced by Savage et al. (1977) (see Figure 3.3). The blue line is the continuum level used for this work.

Source	$\log_{10}$N(H_2) [$\log_{10}$ cm^{-2}]	$\log_{10}$N(0) [$\log_{10}$ cm^{-2}]	$\log_{10}$N(1) [$\log_{10}$ cm^{-2}]	$\log_{10}$N(2) [$\log_{10}$ cm^{-2}]	T_{01} [K]
Savage+ 77	19.83	19.46 ± 0.06	19.58 ± 0.06	–	88
Copr. no R(2)[a]	$19.84^{+0.04}_{-0.04}$	$19.48^{+0.04}_{-0.03}$	$19.59^{+0.03}_{-0.05}$	–	87 ± 8
Copr. w/ R(2)[a]	$19.79^{+0.05}_{-0.04}$	$19.52^{+0.03}_{-0.04}$	$19.47^{+0.04}_{-0.05}$	$16.43^{+0.89}_{-0.31}$	74 ± 6
CHESS-3 to $J'' = 1$	$19.80^{+0.22}_{-0.19}$	$19.58^{+0.26}_{-0.21}$	$19.39^{+0.14}_{-0.16}$	–	64 ± 6
CHESS-3 to $J'' = 2$	$19.77^{+0.22}_{-0.18}$	$19.62^{+0.26}_{-0.22}$	$19.17^{+0.03}_{-0.08}$	$18.44^{+0.32}_{-0.42}$	52 ± 7
CHESS-3 to $J'' = 7$	$19.71^{+0.17}_{-0.16}$	$19.50^{+0.17}_{-0.15}$	$19.17^{+0.07}_{-0.08}$	$18.12^{+0.11}_{-0.27}$	57 ± 11

Note: Column density errors were calculated using $\sigma_{\rm cont}$.
[a] Fits to the *Copernicus* data using the CHESS analysis code.

Table 7: A summary of β Sco H_2 analyses

of Drake et al. (1976), this flat portion is smaller than the pixel dλ of the data set, so we do not expect excluding it will significantly impacts our results.

Figure 3.5 shows two resulting models of the β Sco *Copernicus* spectrum, one where we fit the same lines as S77 and another where we include the (1-0)R(2) line. In both cases, the models do not agree well with the center region from 1093.1–1093.9 Å. This is in the center of the stray light region, so we suspect that we are not fully accounting for the background throughout it. The purpose of this exercise was to recreate the S77 results, not ensure that we are properly measuring the column densities within it. For that reason, no effort was made to correct for the levels here since, upon examination of Figure 3.3, it does not appear that S77 corrected it either.

Table 7 provides a summary of the various β Sco measurements performed in this work as well as from S77. We see that our initial recreation of the *Copernicus* measurement agrees well with their result, without accounting for the R(2) line in any capacity. We also observe the predicted decrease (by 0.12 dex; $\sim$30%) in the $J'' = 1$ column density once the R(2) line is included in the analysis. The $J'' = 0$ column density also increases by 0.04 dex, which is not surprising given that the R(0) and R(1) lines overlap.

We quantify the magnitude of this change by measuring the percent change ($\Delta_{\%}$) in N(0)

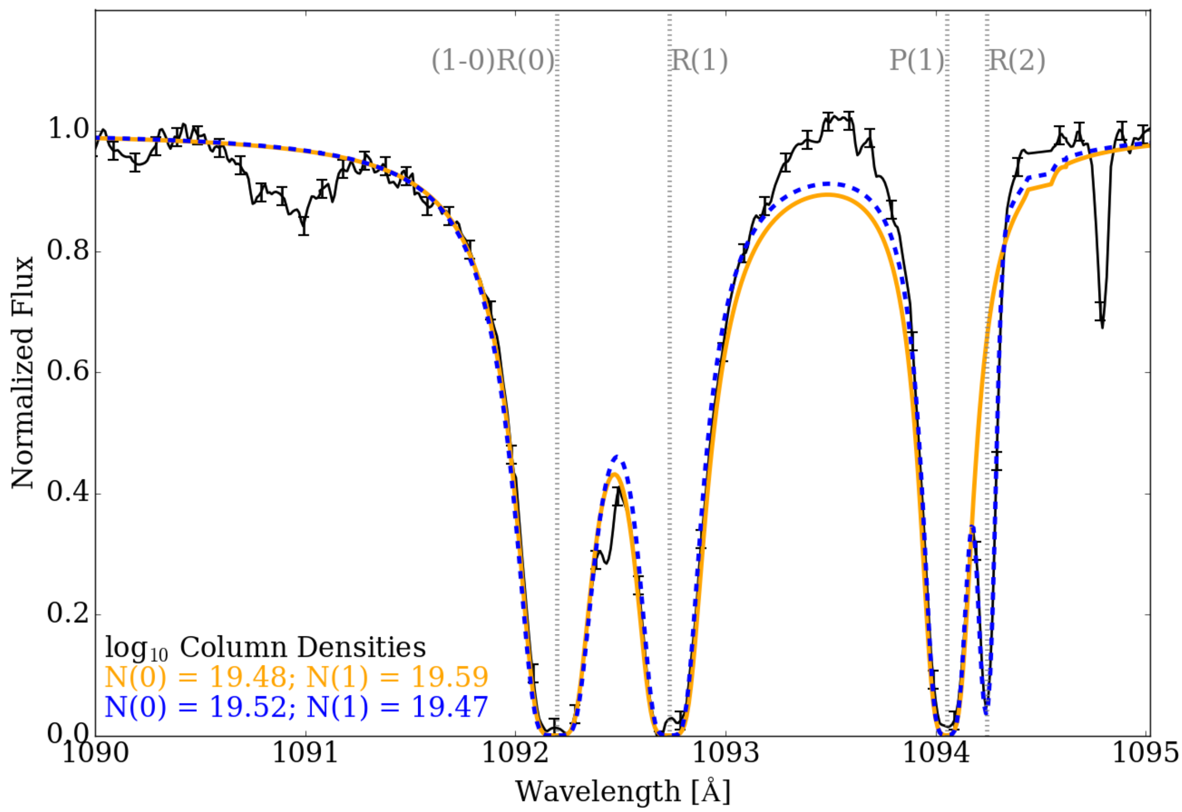

Figure 3.5: The model results for the β Sco *Copernicus* data using the CHESS analysis routine. The model produced using only the R(0), R(1), and P(1) lines is shown in orange. The model when R(2) is also included is plotted as a blue dashed line. The resulting column densities are shown in the lower left.

and N(1) between the fit with $J'' = 2$ and without. We define $\Delta_{\%}$ as:

$$\Delta_{\%}\mathrm{N}(\mathrm{J}'') = 100 \times \frac{\mathrm{N}(\mathrm{J}'')_x - \mathrm{N}(\mathrm{J}'')_{x-1}}{\mathrm{N}(\mathrm{J}'')_x} \tag{23}$$

Where $\mathrm{N}(\mathrm{J}'')_x$ is the column density of rotational level J'' when x levels are included in the fit and $\mathrm{N}(\mathrm{J}'')_{x-1}$ is the same but for the case that x-1 levels are included. Using this equation and our measured column densities from the *Copernicus* data, we find $\Delta_{\%}\mathrm{N}(0) = 8.0 \pm 3.6\%$ and $\Delta_{\%}\mathrm{N}(1) = -32.3 \pm 2.5\%$.

The errors on $\Delta_{\%}$ are calculated through standard propagation of error techniques but in this case we use σ_{fit} as the error for the column densities, not σ_{cont}. This is because σ_{cont} captures the error in our continuum placement, which would have a similar impact on the column density measurements with and without $\mathrm{J}'' = 2$ and so the error would be degenerate between the two measurements. $\mathrm{N}(\mathrm{J}'')_x$ and $\mathrm{N}(\mathrm{J}'')_{x-1}$ result from fits to identical data, the only difference being the number of J'' levels included their models. This means that there also exists a degeneracy in σ_{fit} between the two models. As we have seen, the column density for a given J'' will rely on the column densities of the other J'' levels that are considered, which complicates attempts to disentangle the error degeneracy between the two models. To avoid overconstraining our resulting errors by making assumptions about the amount of degeneracy, we choose to adopt the σ_{fit} values and treat them as a worst-case estimate of the error.

Even with this additional correction to the S77 N(1) value, our measurements still disagree. The difference in $\log_{10}\mathrm{N}(2)$ of almost 2 dex indicates that line blending between P(1) and R(2) could still be occurring. This is supported by the good agreement between our $\mathrm{N}(\mathrm{H}_2)$ and N(0) values as well as the fact that the excitation diagram for a low N(2) value, on the order of the $10^{16.50}$ cm^{-2} that we measured using the *Copernicus* data, would look nonphysical, given the sizes of N(0) and N(1).

3.2 γ Ara

3.2.1 CHESS results

Figure 3.6 shows the continuum normalized flight spectrum of γ Ara over the bandpass of interest for H_2 absorption features and Table 8 lists a summary of the resulting fit parameters. Overplotted in orange is the modeled H_2 absorption profile. The spectrum was produced using the same methods described in §3.1.1. In this case it has been binned down to d$\lambda \sim$ 0.04 Å per bin, which is about 2 bins per resolution element. Figure 3.7 shows the excitation diagram for our modeled spectrum.

The spectrum was heavily impacted by stellar and ISM absorption features. The effect, in this case, was larger than it was for β Sco due to the wind-broadening of the stellar lines and γ Ara's larger distance. Attempts to fit these feature along with the continuum did not improve the effect they had on the spectrum, so we instead opted to mask them. This included S IV 1062 Å, Ar I 1066 Å, S IV 1072 Å, 1073, and the N II complexes around 1084, 1085 Å. We additionally found a currently unidentified absorption complex around the low J$''$ (0-0) vibrational band absorption lines and so we trimmed the long wavelength end of the spectrum at 1105 Å. There is an additional unidentified absorption feature on the short wavelength side of (2-0)R(0), near 1076 Å, that we observe in our data as well as the *Copernicus* data (§3.2.2). It lies close to the CO (E-X) transitions at 1076 Å, which Morton & Hu (1975) claimed to detect. If the origin of the feature was CO, we would expect to see also see the (B-X) transitions near 1088 Å. That region of our spectrum is contaminated by other effects so we cannot confirm its presence. In addition to this, the low N(H_2) of the sightline makes the existence of CO along it unlikely.

Due to a combination of factors (the star is more distant, our pointing drifted during flight, and we had higher resolution), the S/N of the γ Ara data is lower than that of β Sco and this is reflected in the resulting fits. In particular, our modeled N(3) seems relatively high compared to N(2), and that larger value could be influencing the smaller modeled column

b [km s^{-1}]	$\log_{10}$N(H$_2$) [$\log_{10}$ cm^{-2}]	$\log_{10}$N(0) [$\log_{10}$ cm^{-2}]	$\log_{10}$N(1) [$\log_{10}$ cm^{-2}]	$\log_{10}$N(2) [$\log_{10}$ cm^{-2}]	$\log_{10}$N(3) [$\log_{10}$ cm^{-2}]
3.0 ± 1.0	$19.39^{+0.20}_{-0.19}$	$19.03^{+0.16}_{-0.17}$	$19.07^{+0.15}_{-0.18}$	$17.69^{+0.41}_{-0.16}$	$18.2^{+0.48}_{-0.59}$
$\log_{10}$N(4) [$\log_{10}$ cm^{-2}]	$\log_{10}$N(5) [$\log_{10}$ cm^{-2}]	$\log_{10}$N(6) [$\log_{10}$ cm^{-2}]	$\log_{10}$N(7) [$\log_{10}$ cm^{-2}]	T$_{01}$ [K]	T$_{\rm exc}$ [K]
$15.04^{+1.87}_{-0.63}$	$13.61^{+3.20}_{-12.53}$	$14.09^{+2.71}_{-14.09}$	$12.77^{+3.64}_{-12.77}$	82 ± 2	114 ± 114

Table 8: CHESS-4 γ Ara fit results

densities at higher J$''$ states. As such, we feel confident comparing our modeled N(0) and N(1) values to the results of S77, but we do not expect that our higher J$''$ column densities or T$_{\rm exc}$ measurement provide a meaningful constraint to the γ Ara sightline.

3.2.2 Comparison to Savage et al. (1977)

S77 also used the *Copernicus* satellite to measure the H$_2$ column densities along the line of sight to γ Ara. In this case, the U2 channel was used. This channel has lower resolution but the scan it produced is complete over a bandpass $\lambda\lambda$ 1040–1120 Å. They analyze the same vibrational bands, (0-0) to (4-0), that we covered in the CHESS analysis. They treated each band separately, obtaining a modeled N(0) and N(1) in each case using the R(0), R(1), and P(1) features. They then averaged their results to obtain values of $\log_{10}$N(0) = 18.93 ± 0.23 and $\log_{10}$N(1) = 18.94 ± 0.23. Our CHESS results and those of S77 are in better agreement in this case, differing by about 0.1 dex (∼20%), which is well within the error bars of both measurements. Nonetheless, that agreement is assuming that the inclusion of R(2) would not impact the S77 result, which was not the case for β Sco and disagrees with expectations. To test this, we again attempt to recreate the analysis of S77.

The procedure for U2 data is similar to that of U1, but involves a few additional steps. Unlike the β Sco case, S77 did not publish a plot of their final background corrected γ Ara spectrum and so we lack a similar point of comparison when attempting to recreate their

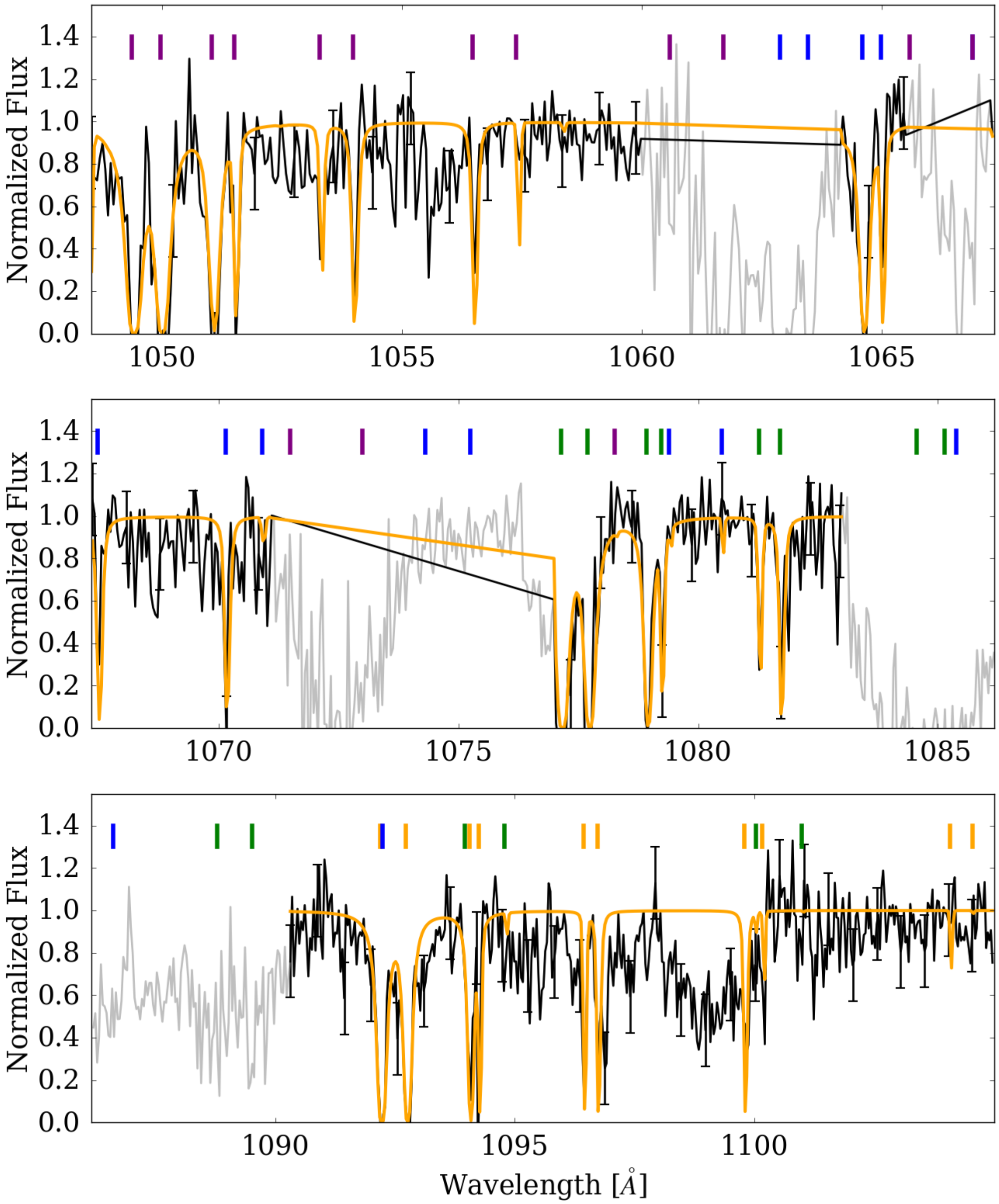

Figure 3.6: The extracted 1D flight spectrum for γ Ara, plotted in black, with our model overplotted in orange. Regions of the spectrum that were masked are plotted in gray. The vertical ticks indicate the positions of the H_2 absorption features, up to $J'' = 7$, from the following vibration bands: v′-v″ = 0-0 (red), 1-0 (orange), 2-0 (green), 3-0 (blue), and 4-0 (purple).

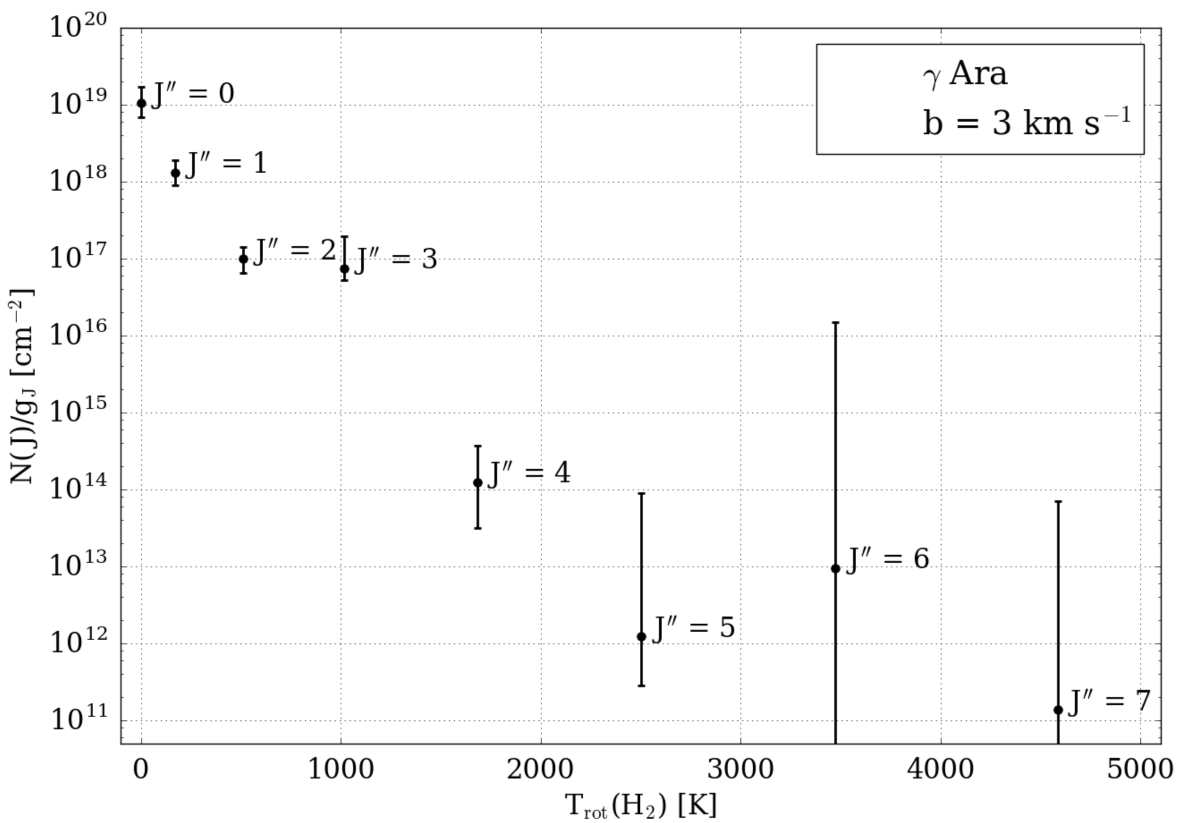

Figure 3.7: H_2 excitation diagram derived from our spectral profile fitting of γ Ara using rotational levels J$'' = 0$–7.

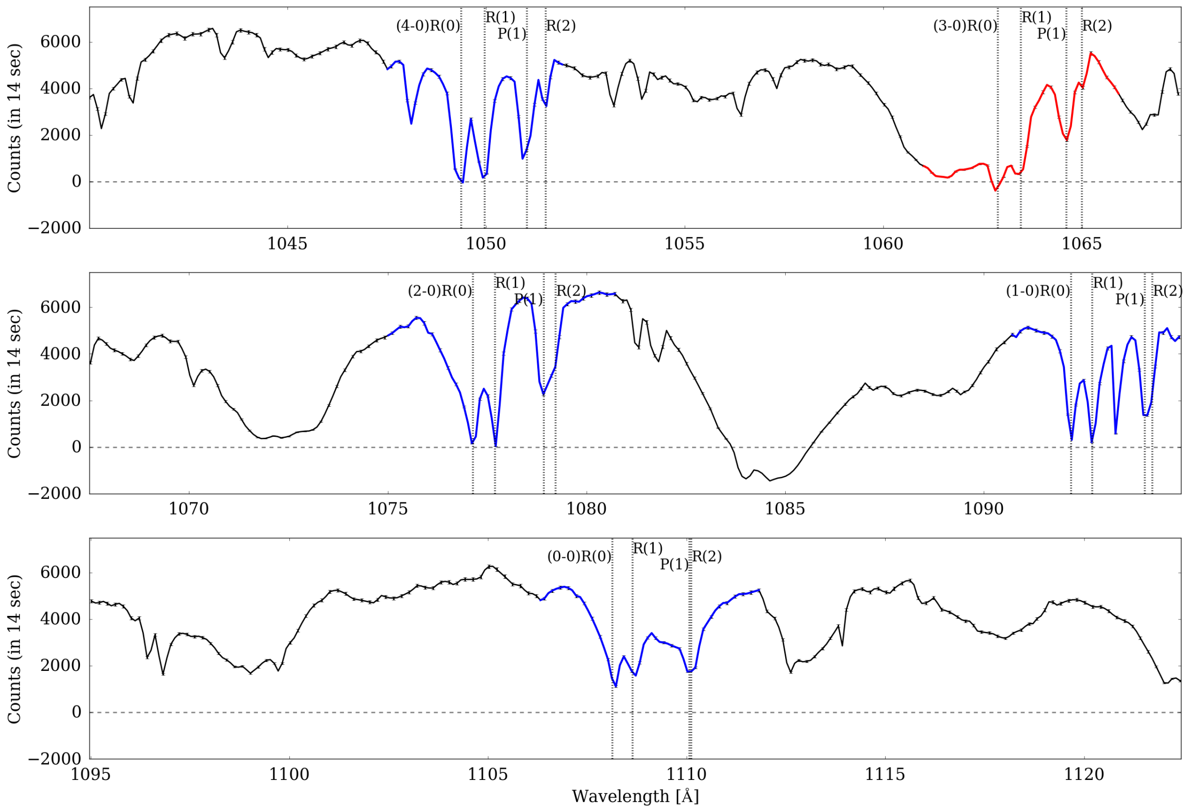

Figure 3.8: The γ Ara *Copernicus* spectrum over the bandpass of interest. The counts on the y-axis have been corrected for scatter and stray light, and then adjusted so that the core of the Lyα absorption feature had zero counts. The blue regions indicate portions of different H_2 vibrational bands that were used in analysis, as indicated by the labeled H_2 lines of interest. The red region highlights the (3-0) band, which was not included in the fitting routine.

results. First, stray and scattered light were subtracted from the raw spectrum following the procedure described by Bohlin (1975), which accounts for grating scatter and stray light, with the stray light level being determined by the count rate ∼20 Å blueward of a wavelength. The resulting background-corrected spectrum is shown in Figure 3.8. S77 rejected vibrational bands that had any issues with stellar blending, but they did not specify which objects contained rejections. Upon initial inspection, we suspect that at least the (3-0) band was rejected for γ Ara due to its blending with the S IV feature at 1062.7 Å. We have highlighted this band in red in Figure 3.8 and do not include it in our subsequent analysis.

We further adjusted the zero points of the wavelength and counts individually in the four remaining bands. Each band was then fit with a continuum that was created by a spline interpolation of several points on either side and across the absorption features. The continua were used to normalize the spectra before the column densities were modeled using the CHESS analysis code. The instrument profile in this case was described as a trapezoid with FWHM = 0.2 Å (Savage et al., 1977). No additional detail on the shape of the trapezoid was given and we were unable to find additional sources that provided more information. Instead, we found that the origin and shape of the U1 profile resulted from the convolution of the instrument and exit slits (Jenkins, 1975; Drake et al., 1976). Following that, we convolved the two box car functions that were the width of the entrance and exit slits of the U2 channel (24 and 96 μm, respectively), and then scaled the resulting function so that it had a FWHM of 0.2 Å. There are additional corrections that should be made to the perfect trapezoidal shape due to effects such as the slight variation in the diffraction angle for different wavelengths off the grating. This results in light entering the slit at slightly different angles. The magnitude of these effects are assumed to be small (on the order of 3% of the total width in the U1 case) and, given that the dλ = 0.1 Å of the U2 data is comparably large, we choose to ignore any influence from them.

Figure 3.9 shows the resulting fits for the four vibrational bands studied in the γ Ara *Copernicus* spectrum. As was done in §3.1.2, we performed one fit using the same lines as S77 and another where we include the R(2) line in each band. Like we saw in the CHESS spectrum, the (2-0) and (0-0) bands have additional absorption on the blue-ward side of the R(0) feature. In the (2-0) case, we were able to exclude this region from the analysis and still generate a reasonable looking result. In the (0-0) case, the additional source of absorption causes the fitting routine to measure significantly larger column densities. As a demonstration of this, the curve for the case where N(0) and N(1) = $10^{18.95}$ cm^{-2} has been included in Figure 3.9. It shows that, even though the line cores are at roughly the correct depths in the *Copernicus* data, the entirety of spectrum falls below the expected values. For this reason, it was excluded from further analysis and we instead just averaged the results from the three remaining bands.

Source	$\log_{10}$N(H_2) [$\log_{10}$ cm^{-2}]	$\log_{10}$N(0) [$\log_{10}$ cm^{-2}]	$\log_{10}$N(1) [$\log_{10}$ cm^{-2}]	$\log_{10}$N(2) [$\log_{10}$ cm^{-2}]	T_{01} [K]
Savage+ 77	19.24	18.93 ± 0.23	18.94 ± 0.23	–	79
No R(2)[a]	19.31 ± 0.01	18.93 ± 0.06	19.07 ± 0.03	–	92.3 ± 10.5
w/ R(2)[a]	19.29 ± 0.02	18.95 ± 0.04	19.00 ± 0.01	17.6 ± 0.35	81.5 ± 3.4
CHESS-4 to J″ = 1	$19.38^{+0.22}_{-0.18}$	$19.03^{+0.16}_{-0.18}$	$19.13^{+0.26}_{-0.19}$	–	77 ± 33
CHESS-4 to J″ = 2	$19.36^{+0.14}_{-0.17}$	$19.02^{+0.04}_{-0.16}$	$19.08^{+0.19}_{-0.19}$	$17.75^{+0.46}_{-0.23}$	81 ± 24
CHESS-4 to J″ = 7	$19.39^{+0.20}_{-0.19}$	$19.03^{+0.16}_{-0.17}$	$19.07^{+0.15}_{-0.18}$	$17.69^{+0.41}_{-0.16}$	82 ± 2

Note: Column density errors were calculated using σ_{cont}.
[a] Fits to the *Copernicus* data using the CHESS analysis code.

Table 9: A summary of γ Ara H_2 analyses

Table 9 provides a summary of the various γ Ara measurements performed in this work, as well as that of S77. Our initial recreation of the *Copernicus* γ Ara measurement agrees reasonably well with their result, although our $\log_{10}$N(1) measurement is 0.13 dex larger that difference is within their error bars. Including the R(2) lines in the fits again produces a lower N(1) value, in this case resulting in $\Delta_{\%}$N(0) = 4.5 ± 17.0% and N(1) = -17.5 ± 6.2%. The column densities produced using the CHESS-4 data are all at least a 0.1 dex larger than the corresponding S77 values, but these differences are within the error bars in each case.

3.3 Quantifying Percent Change

3.3.1 The Extended Data Set

While the β Sco analysis made a compelling argument in favor of a systematic error in the S77 column densities, the results were less conclusive for γ Ara. The existence of such an offset could have an impact on the measured average T_{01} of that data set, leading to a change in the value that has been the primary point of comparison for H_2-based measurements of the diffuse ISM. The effect that a $\Delta_{\%}$ in N(0) and N(1) can have on T_{01} is demonstrated in Table 10, where the top row lists potential $\Delta_{\%}$N(0) values, increasing from 0 to 25%, and the left-most column lists potential $\Delta_{\%}$N(1) values, decreasing from 0 to -50%. The remainder

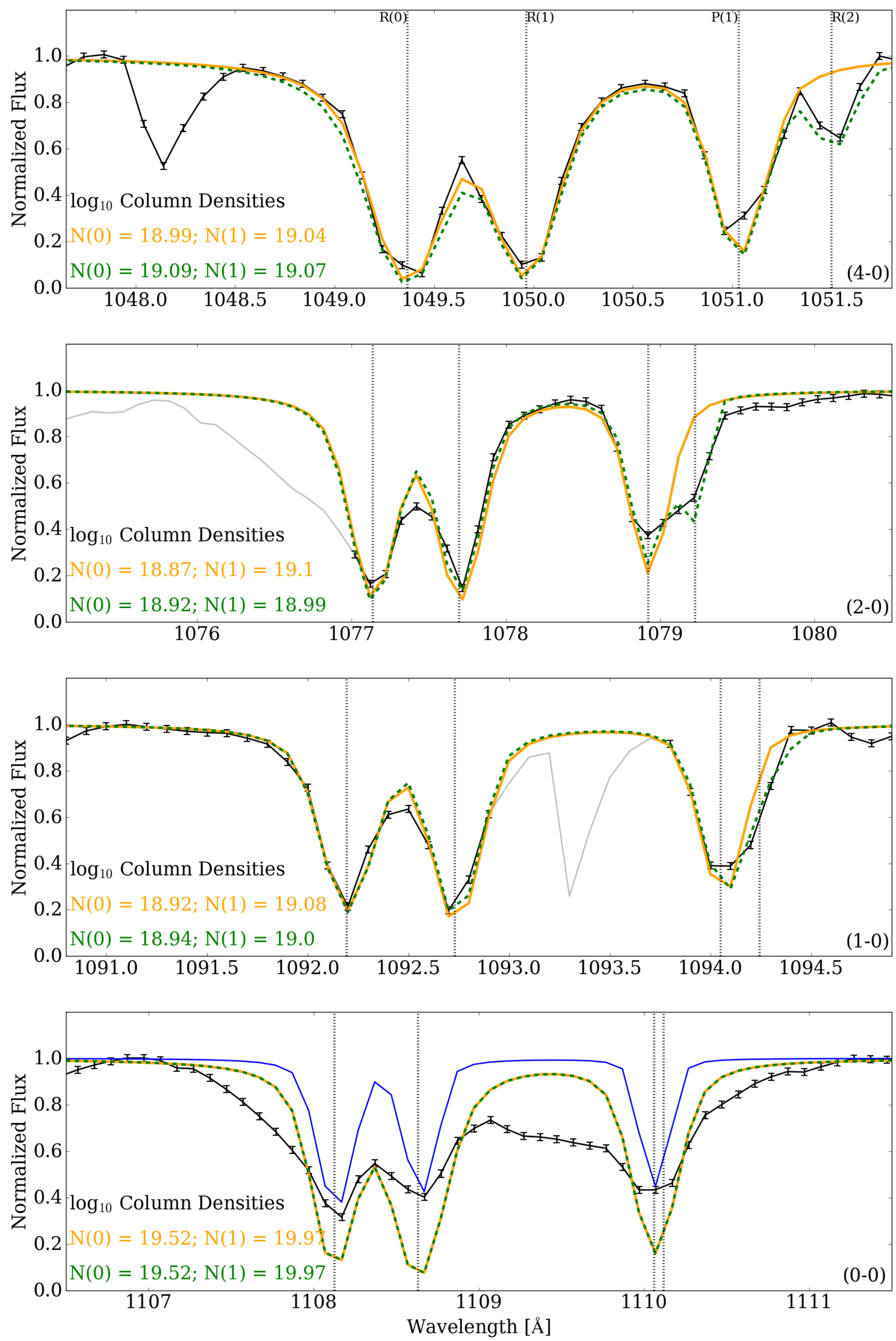

Figure 3.9: Fits to the γ Ara *Copernicus* data using the CHESS flight data analysis code. The spectrum is plotted in black, with regions that were excluded from the analysis plotted in gray. Each figure shows the fits for a single vibrational band, indicated by the designation in the lower right. The orange line shows the fit when the R(2) line is excluded and the green line shows when it is included. The column densities are listed in the lower left of each figure. The blue line in the bottommost figure shows the absorption profile for the case that $\log_{10}\mathrm{N}(0) = \log_{10}\mathrm{N}(1) = 18.95$.

		$\Delta_{\%}$N(0)					
	[%]	0	5	10	15	20	25
$\Delta_{\%}$N(1)	0	77.0	75.2	73.4	71.6	69.7	67.9
	-10	73.7	72.1	70.4	68.7	67.0	65.3
	-20	70.9	69.4	67.9	66.3	64.7	63.1
	-30	68.6	67.1	65.7	64.2	62.7	61.2
	-40	66.5	65.2	63.8	62.4	61.0	59.6
	-50	64.7	63.4	62.1	60.8	59.5	58.2

Note: Temperatures are in units K.

Table 10: The impact of the $\Delta_{\%}$N(0) and $\Delta_{\%}$N(1) on the average T_{01} of Savage et al. (1977)

of the grid shows the resulting average T_{01} of the S77 sample that would be measured if the given $\Delta_{\%}$N(0) and N(1) are applied to each object. As a check, when no change is applied, we reproduce the T_{01} = 77 K that is quoted by S77. If, as an example, we apply the measured $\Delta_{\%}$ of β Sco (8% for N(0) and -32% for N(1)) we see that average temperature of the sample would be reduced to ∼66 K.

To further explore this effect, we perform to sightlines beyond those observed by CHESS to better constrain the magnitude of the $\Delta_{\%}$ in the column densities of the S77 data set. This could be done by running an analysis on the entire S77 catalog, similar to what was done for β Sco and γ Ara, but that process would be difficult given the quality of the data, particularly for objects with U2 observations, and the lack of information on the final background subtracted spectra that were used by S77. In addition to this, the *Copernicus* U1 data are, in general, limited to the (1-0) Lyman absorption band. While we can obtain a measurement of $\Delta_{\%}$ in this region by including the single R(2) line, the resulting constraint on N(1) is limited compared to the multiple J$''$ = 1 and 2 lines available over a wider bandpass. The better option would be to study not just the influence of a single J$''$ = 2 line, but rather several J$''$ = 2 lines and even higher J$''$ levels. Once those levels are included, a similar interplay between column densities likely arises from neighboring lines in the same vibrational band (e.g. P(1) and R(2)) and from lines in different vibrational bands that are coincident (e.g. (1-0)P(1) and (3-0)P(5)). Quantifying the interplay between various J$''$

levels is thus useful not only in the context of a correction to the S77 results but also for H_2 studies as a whole, since it provides a metric for determining the appropriate number of J'' levels to consider for a given column density.

To tackle these problems, we generate a data set comprised of observations from *Copernicus* and *FUSE*. We select the highest quality *Copernicus* objects from S77 in order to reanalyze these sightlines. These objects are then used as a point of comparison to the selected *FUSE* objects, which sample a broader range in column density and have a larger bandpass. Assuming the two groups produce comparable $\Delta_{\%}$ measurements, we can combine them to generate a trend in $\Delta_{\%}$ as a function of $N(H_2)$ that can be used to revise the diffuse ISM temperatures derived by S77.

For the extended *Copernicus* sample, objects were selected based off of their quoted error in N(0) and N(1), which we found acted as a proxy for the quality of the spectra. The final selection of objects had $\log_{10}N(H_2)$ ranging from 19.49–20.28 and were all observed using the U1 channel. Information on the nine selected targets can be found in Table 11. Analysis of each sightline followed the same procedure as that of β Sco, described in §3.1.2. Unlike β Sco, 8 of the 9 objects lacked a published background-corrected spectrum in the S77 paper. In those cases, we iterated on the placement of the continuum until we were able to achieve the same results as S77, within their quoted error. We again focused on recreating their measurements and not on an independent determination of the column densities. A summary of our modeled column densities for these objects can be seen in Table 13.

To create the *FUSE* sample, we used Wakker (2006), Gillmon et al. (2006), Rachford et al. (2009), and Burgh et al. (2010) to select a total of 13 objects with archival *FUSE* observations that span a range in $\log_{10}N(H_2)$ of 14.5–20.69. This upper limit agrees well with that of the S77 sample, which has a maximum $\log_{10}N(H_2)$ of 20.67. In all cases, objects were first selected for column density and then S/N. We attempted to only select sightlines that showed signs of a single H_2 absorption component. For the highest column density objects, we additionally selected for sightlines that had low CO/H_2 ratios to ensure that we

Name	$\log_{10}$N(H_2) [$\log_{10}$ cm^{-2}]	$\log_{10}$N(0) [$\log_{10}$ cm^{-2}]	$\log_{10}$N(1) [$\log_{10}$ cm^{-2}]	error [dex]
HD 149757	20.65	20.51	20.10	0.08
HD 167264	20.28	19.98	19.98	0.10
HD 112244	20.14	19.80	19.88	0.11
HD 144470	20.05	19.78	19.72	0.11
HD 188209	20.01	19.72	19.70	0.11
HD 145502	19.89	19.52	19.65	0.15
HD 113904B	19.83	19.41	19.62	0.11
HD 135591	19.77	19.53	19.40	0.11
HD 164402	19.49	19.04	19.30	0.18

Table 11: Published H_2 column densities of selected *Copernicus* objects from Savage et al. (1977)

were not creating a data set that contained both translucent and diffuse sightlines (Snow & McCall, 2006), minimizing the effects of potential differences in T_{01} between those two populations. A summary of the selected objects that were used for analysis can be seen in Table 12.

The pre-processing of the *FUSE* objects roughly followed that of Wakker (2006). All observations, with the exception of HD 186994, used the LWRS channel. For HD 186994, data from the HIRS channel was used. All available observations for a given object were first co-added by channel and then binned by 3–4 pixels to avoid oversampling the data. This resulted in ∼0.04 Å wide pixels, which is about 1 bin per resolution element. The two LiF channels alone provided enough coverage of the bandpass that we chose to only use those for our analysis. This left a ∼7 Å gap in the spectrum centered near 1085 Å. We aligned each of the LiF channels individually using a linear equation to calculate the shift, with a separate shift being applied on either side of the 1085 Å gap. The equation was determined by comparing observed H_2 absorption line centers to the laboratory wavelength and fitting the result. We found that a linear profile lead to shift corrections that, on average, placed absorption features to within 1×10^{-2} Å of the expected line center. The largest offsets

Name	$\log_{10}$N(H_2) I [$\log_{10}$ cm^{-2}]	$\log_{10}$N(H_2) II[a] [$\log_{10}$ cm^{-2}]	Source[a]
HD 157857	20.69 ± 0.09	–	1
HD 102065	20.53 ± 0.10	20.50 ± 0.06	1,2
HD 152590	20.51 ± 0.09	–	1
HD 99857	20.25 ± 0.10	–	1
HD 218915	20.16 ± 0.10	–	1
HD 104705	20.00 ± 0.10	–	1
NGC 7469	$19.76^{+0.05}_{-0.04}$	$19.67^{+0.10}_{-0.10}$	3,4
HD 186994	19.59 ± 0.04	–	2
Mrk 335	$19.07^{+0.07}_{-0.07}$	$18.83^{+0.80}_{-0.80}$	3,4
PG 0844+349	$18.56^{+0.09}_{-0.09}$	$18.22^{+0.18}_{-0.28}$	3,4
NGC 1068[b]	$18.07^{+0.30}_{-0.43}$	$18.13^{+0.13}_{-0.17}$	3,4
NGC 4151	$16.60^{+0.54}_{-0.16}$	$16.70^{+0.93}_{-0.31}$	3,4
PKS 0405-12	$16.01^{+0.28}_{-0.14}$	$15.44^{+0.18}_{-0.12}$	3,4

[a] Multiple sources are listed for objects with more than one independently measured column density. The sources are: (1) Burgh et al. (2010); (2) Rachford et al. (2009); (3) Wakker (2006); (4) Gillmon et al. (2006).
[b] Wakker (2006) measured a second H_2 absorption component shifted -63 km s^{-1} from the primary absorption at an upper limit $\log_{10}$N(H_2) = 14.82. We did not include this component in our analysis routine.

Table 12: Published H_2 column densities of selected *FUSE* objects

we found after applying the corrections were $\sim 2.5 \times 10^{-2}$ Å, which is within the width of a single pixel. Once each channel was individually aligned, the two were averaged together to generate the final flux spectrum.

A continuum for each spectrum was constructed by combining at least five splines, ranging in wavelength from 10–40 Å, with the length of an individual section being determined by the variability in the slope of the continuum. Similar to the creation of the CHESS continuum, regions of the spectrum that did not contain any absorption features were selected by hand and those points were used to generate the spline. In rare cases where the shape of the continuum was masked by a large absorption features, a polynomial fit was used instead. Peak fluxes above the absorption features were estimated in an effort to correctly level the continuum across the gap. An example of this is shown in Figure 3.10 for NGC 7469, which has a broad O VI emission feature (Kriss et al., 2003) that is coincident with the low-J$''$ (4-0) absorption lines around 1050 Å. In that case, a 2nd-order polynomial was used to generate the continuum across the gap.

Once normalized, the spectra were fit using the CHESS analysis code and an R = 15,000 Gaussian (Wakker, 2006) for the instrument profile. We found that our fit results were initially being skewed by the comparatively small error bars in the troughs of the absorption features. To remedy this, we set the values of any error bar smaller than the average error equal to the average standard deviation of a section of unabsorbed continuum. Like in the procedure used for the CHESS observations, non-H_2 absorption features were masked. This occasionally resulted in the masking of one or more low-J$''$ lines of interest, but all objects that were used in our final analysis had at least three bands of R(0), R(1), and P(1) absorption features included in the fitting routine. Example fits using J$''$ = 0–1 and J$''$ = 0–2 are shown in Figure 3.11 for NGC 7469.

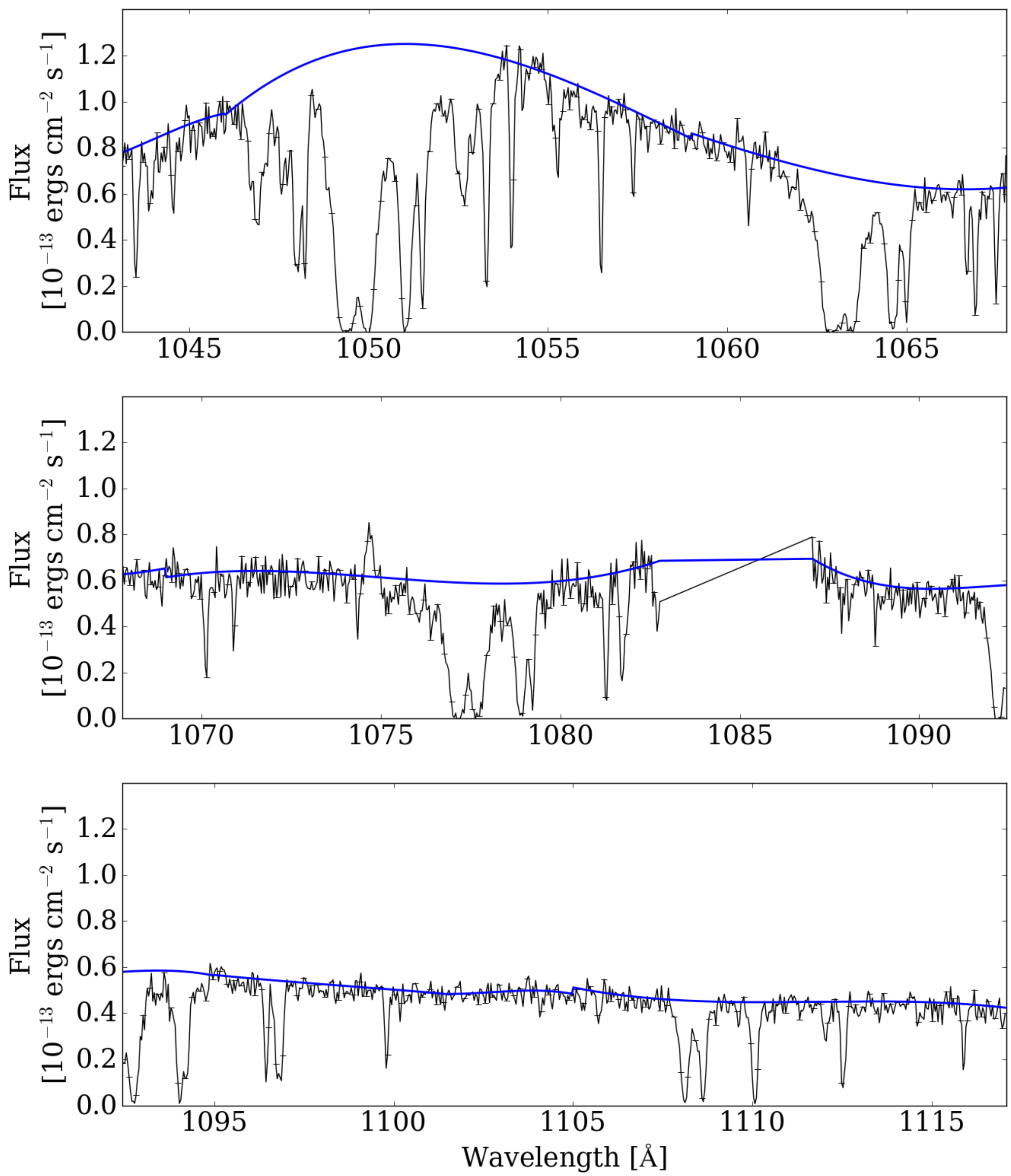

Figure 3.10: The raw *FUSE* spectrum of NGC 7469 (black) with the continuum overplotted in blue.

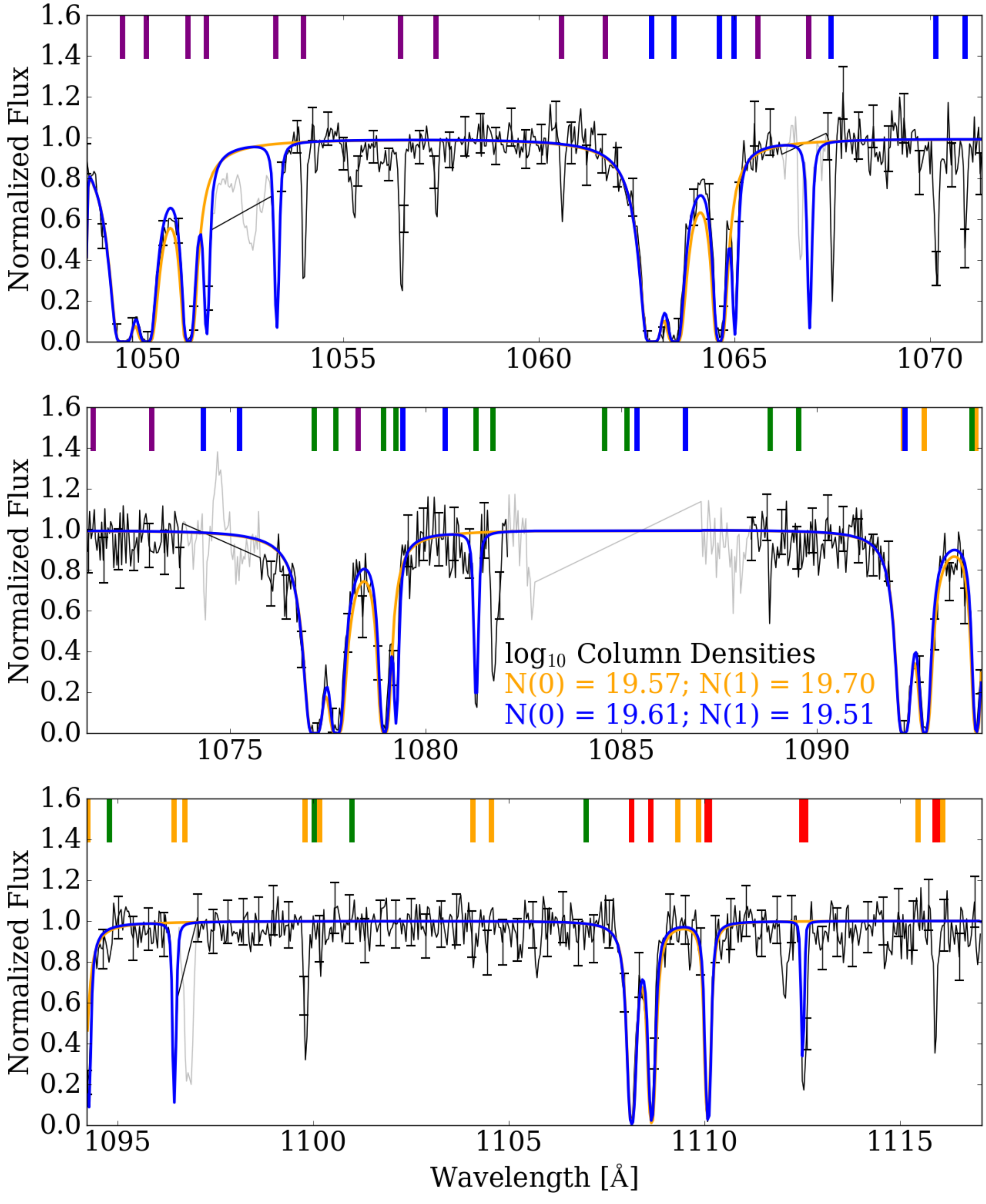

Figure 3.11: The continuum-normalized *FUSE* spectrum of NGC 7469, fit using the J″ = 0–1 (in orange) and J″ = 0–2 (in blue) absorption features. The resulting J″ = 0 and 1 column densities are listed in the gap at 1085 Å. The vertical ticks indicate the positions of the H_2 absorption features, up to J″ = 7, from the following vibration bands: v′-v″ = 0-0 (red), 1-0 (orange), 2-0 (green), 3-0 (blue), and 4-0 (purple).

Name	$\log_{10}N(H_2)$ [$\log_{10}$ cm^{-2}]	$\log_{10}N(0)$ [$\log_{10}$ cm^{-2}]	$\log_{10}N(1)$ [$\log_{10}$ cm^{-2}]	$\log_{10}N(2)$ [$\log_{10}$ cm^{-2}]	$\log_{10}N(3)$ [$\log_{10}$ cm^{-2}]	$\log_{10}N(4)$ [$\log_{10}$ cm^{-2}]	b[a] [km s^{-1}]	T_{01} [K]
				Copernicus				
HD 149757	$20.62^{+0.04}_{-0.03}$	$20.49^{+0.04}_{-0.03}$	$20.01^{+0.02}_{-0.02}$	$18.41^{+0.03}_{-0.03}$	–	–	$\leq$2.0	52 ± 1
HD 167264	$20.31^{+0.09}_{-0.08}$	$20.02^{+0.09}_{-0.08}$	$19.99^{+0.09}_{-0.07}$	$18.05^{+1.67}_{-0.44}$	–	–	5.5 ± 3.2	75 ± 1
HD 112244	$20.12^{+0.10}_{-0.11}$	$19.85^{+0.09}_{-0.10}$	$19.79^{+0.11}_{-0.08}$	$17.95^{+0.66}_{-0.87}$	–	–	8.6 ± 6.6	73 ± 1
HD 144470	$19.98^{+0.02}_{-0.02}$	$19.80^{+0.01}_{-0.01}$	$19.50^{+0.03}_{-0.03}$	$16.09^{+0.18}_{-0.18}$	–	–	10.0± 0.2	59 ± 1
HD 188209	$19.99^{+0.13}_{-0.13}$	$19.77^{+0.12}_{-0.14}$	$19.57^{+0.12}_{-0.08}$	$18.31^{+1.04}_{-0.44}$	–	–	6.1 ± 4.1	64 ± 3
HD 145502	$19.91^{+0.05}_{-0.05}$	$19.60^{+0.03}_{-0.03}$	$19.61^{+0.07}_{-0.06}$	$17.61^{+0.59}_{-0.44}$	–	–	4.8 ± 1.1	78 ± 3
HD 113904B	$19.79^{+0.07}_{-0.06}$	$19.44^{+0.05}_{-0.04}$	$19.53^{+0.09}_{-0.07}$	$16.13^{+0.17}_{-0.38}$	–	–	9.0 ± 1.5	86 ± 4
HD 135591	$19.75^{+0.03}_{-0.03}$	$19.54^{+0.02}_{-0.02}$	$19.33^{+0.05}_{-0.04}$	$15.89^{+0.13}_{-0.27}$	–	–	7.1 ± 1.1	64 ± 2
HD 164402	$19.51^{+0.06}_{-0.05}$	$19.11^{+0.05}_{-0.04}$	$19.28^{+0.07}_{-0.04}$	$17.11^{+1.13}_{-0.63}$	–	–	3.7 ± 1.0	94 ± 3
				FUSE				
HD 157857	$20.69^{+0.03}_{-0.03}$	$20.33^{+0.03}_{-0.03}$	$20.42^{+0.03}_{-0.03}$	$19.02^{+0.02}_{-0.03}$	$18.53^{+0.04}_{-0.04}$	$16.99^{+0.06}_{-0.06}$	$\leq$2.0	85 ± 1
HD 102065	$20.54^{+0.04}_{-0.04}$	$20.28^{+0.04}_{-0.04}$	$20.18^{+0.04}_{-0.04}$	$18.64^{+0.05}_{-0.06}$	$17.71^{+0.12}_{-0.13}$	$15.66^{+0.17}_{-0.28}$	3.0 ± 0.1	70 ± 1
HD 152590	$20.60^{+0.06}_{-0.06}$	$20.42^{+0.07}_{-0.07}$	$20.11^{+0.03}_{-0.03}$	$18.69^{+0.06}_{-0.06}$	$18.16^{+0.09}_{-0.10}$	$15.50^{+0.13}_{-0.16}$	3.8 ± 0.2	59 ± 2
HD 99857	$20.30^{+0.06}_{-0.06}$	$19.99^{+0.08}_{-0.07}$	$19.99^{+0.04}_{-0.05}$	$18.49^{+0.14}_{-0.05}$	$18.21^{+0.20}_{-0.11}$	$14.99^{+0.67}_{-0.12}$	4.9 ± 1.8	78 ± 3
HD 218915	$20.19^{+0.03}_{-0.03}$	$19.92^{+0.03}_{-0.03}$	$19.81^{+0.01}_{-0.01}$	$18.64^{+0.03}_{-0.04}$	$18.53^{+0.05}_{-0.05}$	$17.73^{+0.11}_{-0.14}$	3.6 ± 0.2	70 ± 1
HD 104705	$20.07^{+0.01}_{-0.01}$	$19.72^{+0.02}_{-0.02}$	$19.77^{+0.01}_{-0.01}$	$18.58^{+0.02}_{-0.02}$	$18.36^{+0.03}_{-0.03}$	$15.01^{+0.04}_{-0.03}$	4.0 ± 0.1	81 ± 1
NGC 7469	$19.87^{+0.05}_{-0.05}$	$19.60^{+0.05}_{-0.05}$	$19.51^{+0.04}_{-0.05}$	$18.33^{+0.06}_{-0.07}$	$17.78^{+0.15}_{-0.14}$	$15.30^{+0.05}_{-0.23}$	2.5 ± 0.2	71 ± 1
HD 186994	$19.75^{+0.10}_{-0.11}$	$19.32^{+0.11}_{-0.11}$	$19.50^{+0.09}_{-0.09}$	$18.13^{+0.21}_{-0.38}$	$18.14^{+0.22}_{-0.37}$	$15.58^{+0.25}_{-0.33}$	5.0 ± 0.3	96 ± 2
Mrk 335	$19.11^{+0.06}_{-0.06}$	$18.70^{+0.05}_{-0.05}$	$18.90^{+0.07}_{-0.07}$	$16.24^{+0.03}_{-0.04}$	$16.08^{+0.07}_{-0.10}$	$14.29^{+0.15}_{-0.20}$	5.4 ± 0.1	99 ± 2
PG 0844+349	$18.62^{+0.19}_{-0.07}$	$18.04^{+0.17}_{-0.02}$	$18.49^{+0.13}_{-0.09}$	$15.74^{+1.98}_{-0.21}$	$15.15^{+2.29}_{-0.11}$	$14.24^{+0.15}_{-0.74}$	4.5 ± 2.5	148 ± 20
NGC 1068[b]	$18.36^{+0.22}_{-0.19}$	$18.08^{+0.09}_{-0.12}$	$18.02^{+0.21}_{-0.29}$	$16.39^{+1.13}_{-0.36}$	$16.26^{+1.21}_{-1.06}$	$13.86^{+0.34}_{-3.29}$	3.0 ± 1.0	73 ± 11
NGC 4151	$18.17^{+0.10}_{-0.46}$	$17.48^{+0.12}_{-0.50}$	$18.07^{+0.09}_{-0.45}$	$16.36^{+0.12}_{-0.52}$	$15.36^{+0.25}_{-0.17}$	$13.45^{+0.41}_{-4.42}$	4.0 ± 0.1	203 ± 27
PKS 0405-12	$16.04^{+0.05}_{-0.01}$	$15.24^{+0.05}_{-0.01}$	$15.84^{+0.04}_{-0.03}$	$15.19^{+0.07}_{-0.02}$	$14.83^{+0.07}_{-0.07}$	$13.66^{+0.37}_{-4.99}$	7.2 ± 0.9	208 ± 28

[a] Fits that returned the lowest possible b = 2 km s^{-1} are quoted as upper limits.

[b] Fit using an R = 6,600 Gaussian kernel, following Wakker (2006).

Table 13: Measured $N(H_2)$ using the CHESS analysis pipeline

3.3.2 Percent Change Measurements

The resulting $\Delta_{\%}$N(0) and N(1) for the extended data set are listed in Table 14 and shown in Figure 3.12. In all cases, the quoted values are comparing the fit results when $J'' = 2$ is and is not included. We see that the measured $\Delta_{\%}$ agree well between the *Copernicus* and *FUSE* objects. We also find the expected trend of $\Delta_{\%}$ increasing in magnitude with column density, with the value becoming more positive for N(0) and more negative for N(1). For $N(H_2) \lesssim 10^{18}$ cm^{-2}, N(0) does not appear to be greatly impacted by the inclusion of $J'' = 2$. The same cannot be said for N(1), which maintains a $\Delta_{\%} \sim 10\%$ down to the lowest column densities measured in this work. While in both cases the error bars in this $N(H_2)$ region are large, we caution that their values are likely overestimated (§3.1.2) and note that they agree with expectations. Mainly, the P(1) and R(2) lines are in close proximity to one another, particularly in the high vibrational bands. For example, the two lines are 0.06 Å apart in the (4-0) band, while the FWHM of their individual absorption features are on the order of 0.10 Å for the low $N(H_2)$ objects. This is compared to the 0.50 Å separation between R(0) and R(1) in the same band. This means that N(0) is able to decouple from the relationship between N(1) and N(2), allowing the $\Delta_{\%}$N(0) to decay to zero while N(1) continues to be impacted by inclusion of $J'' = 2$.

To quantify the evolution of $\Delta_{\%}$ with $N(H_2)$ we fit the two trends using second-order polynomials in $\log_{10}N(H_2)$ space. The resulting curves are plotted in Figure 3.12 along with the corresponding 95% confidence intervals on the predicted values. The equations for these curves were found to be:

$$\Delta_{\%}N(0) = -0.145(\log_{10}N(0))^2 + 7.750\log_{10}N(0) - 89.358 \tag{24}$$

$$\Delta_{\%}N(1) = -0.420(\log_{10}N(1))^2 + 10.187\log_{10}N(1) - 61.475 \tag{25}$$

While the accuracy of our trends may not be high enough to provide meaningful updates on the level of an individual object, the corrections should provide a good estimate to the

Name	$\log_{10}$N(0) ($J''_{max} = 1$) [$\log_{10}$ cm^{-2}]	$\log_{10}$N(0) ($J''_{max} = 2$) [$\log_{10}$ cm^{-2}]	$\Delta_{\%}$N(0) [%]	$\log_{10}$N(1) ($J''_{max} = 1$) [$\log_{10}$ cm^{-2}]	$\log_{10}$N(1) ($J''_{max} = 2$) [$\log_{10}$ cm^{-2}]	$\Delta_{\%}$N(0) [%]
			Copernicus			
HD 149757	20.47 ± <0.01	20.49 ± <0.01	4.7 ± 0.3	20.10 ± <0.01	20.01 ± <0.01	-18.7 ± 0.4
HD 167264	20.00 ± 0.02	20.02 ± 0.02	6.2 ± 6.7	20.06 ± 0.02	19.99 ± 0.02	-14.9 ± 7.2
HD 112244	19.80 ± 0.02	19.85 ± 0.02	10.3 ± 6.6	19.91 ± 0.02	19.79 ± 0.02	-24.9 ± 8.2
HD 144470	19.75 ± 0.02	19.80 ± 0.02	11.5 ± 6.4	19.67 ± 0.02	19.50 ± 0.03	-32.8 ± 13.0
HD 188209	19.71 ± 0.02	19.77 ± 0.02	13.0 ± 6.2	19.74 ± 0.02	19.57 ± 0.02	-32.5 ± 9.8
HD 145502	19.56 ± 0.03	19.60 ± 0.02	10.2 ± 7.4	19.72 ± 0.02	19.61 ± 0.02	-22.6 ± 8.7
HD 113904B	19.39 ± 0.03	19.44 ± 0.02	12.0 ± 7.5	19.65 ± 0.02	19.53 ± 0.02	-24.2 ± 9.2
HD 135591	19.51 ± 0.02	19.54 ± 0.02	6.3 ± 6.8	19.45 ± 0.02	19.33 ± 0.03	-24.4 ± 10.8
HD 164402	19.09 ± 0.03	19.11 ± 0.03	5.7 ± 8.6	19.37 ± 0.02	19.28 ± 0.02	-18.6 ± 9.1
β Sco	19.48 ± 0.01	19.52 ± 0.01	8.0 ± 3.6	19.59 ± 0.01	19.47 ± 0.01	-32.3 ± 2.5
γ Ara	18.93 ± 0.06	18.95 ± 0.04	4.5 ± 17.4	19.07 ± 0.03	19.00 ± 0.01	-17.5 ± 6.2
			FUSE			
HD 157857	20.34 ± 0.01	20.38 ± <0.01	9.5 ± 1.6	20.62 ± <0.01	20.44 ± <0.01	-34.1 ± 2.0
HD 102065	20.28 ± 0.01	20.30 ± 0.01	3.6 ± 1.9	20.30 ± 0.01	20.19 ± 0.01	-22.7 ± 2.6
HD 152590	20.48 ± 0.01	20.49 ± 0.01	1.8 ± 1.8	20.29 ± 0.01	20.13 ± 0.01	-31.9 ± 3.4
HD 99857	19.99 ± 0.01	20.02 ± 0.01	7.5 ± 4.0	20.15 ± 0.01	20.00 ± 0.01	-28.7 ± 5.1
HD 218915	19.95 ± <0.01	19.99 ± <0.01	9.9 ± 1.3	20.02 ± <0.01	19.82 ± <0.01	-37.6 ± 2.2
HD 104705	19.71 ± <0.01	19.75 ± <0.01	10.4 ± 1.0	19.95 ± <0.01	19.77 ± <0.01	-33.5 ± 1.2
NGC 7469	19.57 ± 0.02	19.61 ± 0.01	9.5 ± 4.4	19.70 ± 0.01	19.51 ± 0.01	-34.9 ± 5.9
HD 186994	19.33 ± 0.02	19.37 ± 0.02	10.3 ± 6.4	19.67 ± 0.01	19.52 ± 0.02	-29.7 ± 6.7
Mrk 335	18.68 ± 0.02	18.70 ± 0.02	6.5 ± 6.6	18.99 ± 0.02	18.91 ± 0.02	-17.7 ± 6.3
PG 0844+349	18.04 ± 0.08	18.04 ± 0.07	0.7 ± 24.5	18.56 ± 0.04	18.5 ± 0.04	-13.0 ± 14.8
NGC 1068	18.09 ± 0.04	18.09 ± 0.04	-0.7 ± 13.4	18.07 ± 0.06	17.99 ± 0.07	-16.4 ± 24.9
NGC 4151	17.48 ± 0.06	17.48 ± 0.06	-0.1 ± 19.1	18.11 ± 0.03	18.08 ± 0.03	-8.1 ± 10.0
PKS 0405-12	15.25 ± 0.04	15.25 ± 0.04	0.0 ± 14.1	15.88 ± 0.04	15.84 ± 0.04	-8.8 ± 13.8

Note: Quoted errors on column densities are $\sigma_{\rm fit}$.

Table 14: Percent change in N(0) and N(1) with the inclusion of $J'' = 2$

average properties of the S77 sample, mainly T_{01}. When applying our fits to the N(0) and N(1) values of S77, we calculate a new $T_{01} = 68 \pm 13$ K. This value is 9 K ($\sim$ 12%) lower than that of S77, but still within the ± 17 K error bars of their measurement. This updated value is in strong agreement with Rachford et al. (2002, 2009), who measured values of 67 and 68 K, respectively, and still consistent with the values measured by other works such as Burgh et al. (2007) ($T_{01} = 74 \pm 24$ K) or Sheffer et al. (2008) ($T_{01} = 76 \pm 17$ K).

This analysis still only considered the inclusion of the $J'' = 2$ lines. As previously mentioned, this effect is not expected to be limited to just the low-J'' levels. Given the relative

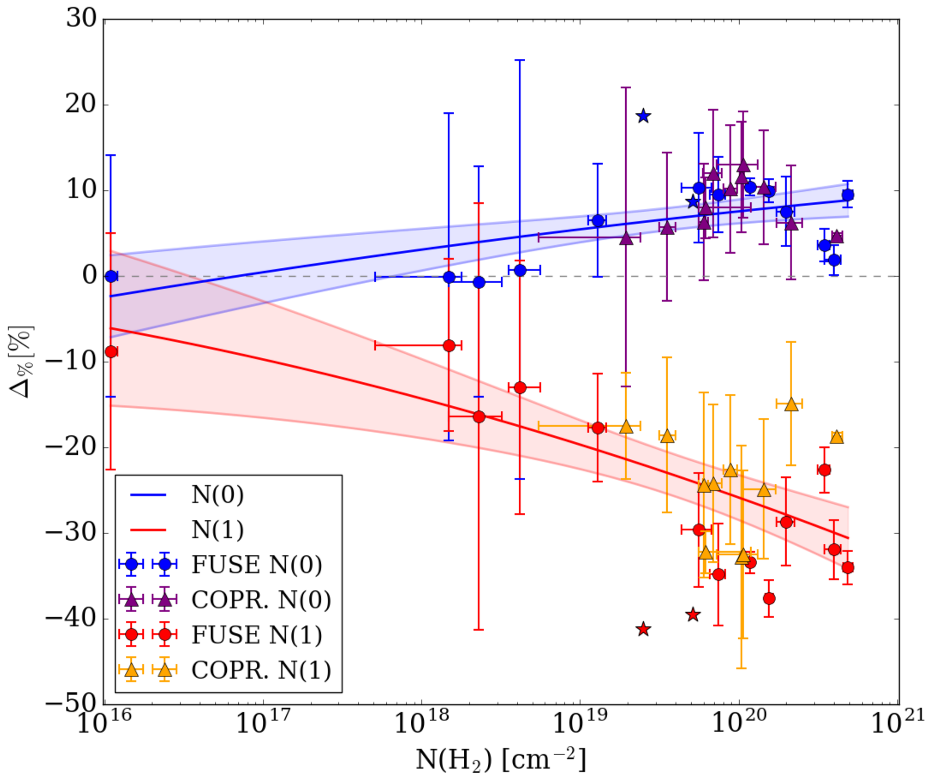

Figure 3.12: The $\Delta_{\%}$N(0) (blue circles for *FUSE*, purple triangles for *Copernicus*) and N(1) (red circles for *FUSE*, orange triangles for *Copernicus*) when the $J'' = 2$ level is included in the model, as a function of total H_2 column density. Second order polynomials have been fit to each distribution and are plotted, along with the surrounding 95% confidence intervals, as a blue line for N(0) and a red line for N(1). The $\Delta_{\%}$ as measured using the CHESS observations are plotted as blue and red stars. They are not included in the fitting routine.

sizes of the higher J'' column densities though, we do not expect their impact on the lower J'' levels to be as significant as it was in the $J'' = 2$ case. The larger bandpass of *FUSE* provides an opportunity to test this by measuring the evolution of $\Delta_{\%}$ as more J'' levels are included. This result is shown in Figure 3.13 where we plot the $\Delta_{\%}N(0–4)$ for seven objects, spanning $\log_{10}N(H_2) = 16.05–20.69$, as subsequent J'' levels are included. When performing these measurements, we started by fitting up to $J'' = 7$ in order to obtain a measurement on b with as many lines as possible. We then fixed that b value when re-running the analysis on the spectra with $J'' < 7$.

We see that, for $\log_{10}N(H_2) \lesssim 19.75$, including $J'' > 2$ in the fitting routine does not appear to significantly impact the $J'' = 0$ and 1 column densities. In the higher column density cases of HD 157857 and HD 186994, we see a small $\Delta_{\%}N(0)$ as we introduce $J'' =$ 3, 4, and/or 5. The values of those changes are on the order of 5%, which is equivalent to a change in temperature of $\lesssim 2$ K, assuming $N(0) \approx N(1)$. For this reason, including higher rotational levels would likely be important for detailed calculations of higher column density sightlines, but we do not expect that it would significantly impact our updated S77 calculation since an offset on the level of 2 K is well within our uncertainty.

4 Summary and Future Work

From the molecular transitions of H_2, CO, and CH, that trace the dense, cold medium, to the atomic transitions of highly ionized species, like O VI, that trace the HIM, FUV observations of the ISM provide crucial details that are pertinent to a wide range of astrophysical phenomena. The array of past space-based and rocket-borne instruments have made great contributions to these topics, using a variety of novel concepts that covered the high signal vs. high resolution trade space that drives UV observatories. The CHESS sounding rocket was designed to contribute to this endeavor by leveraging its high resolution and large bandpass to observe individual diffuse and translucent clouds along the sightlines of bright

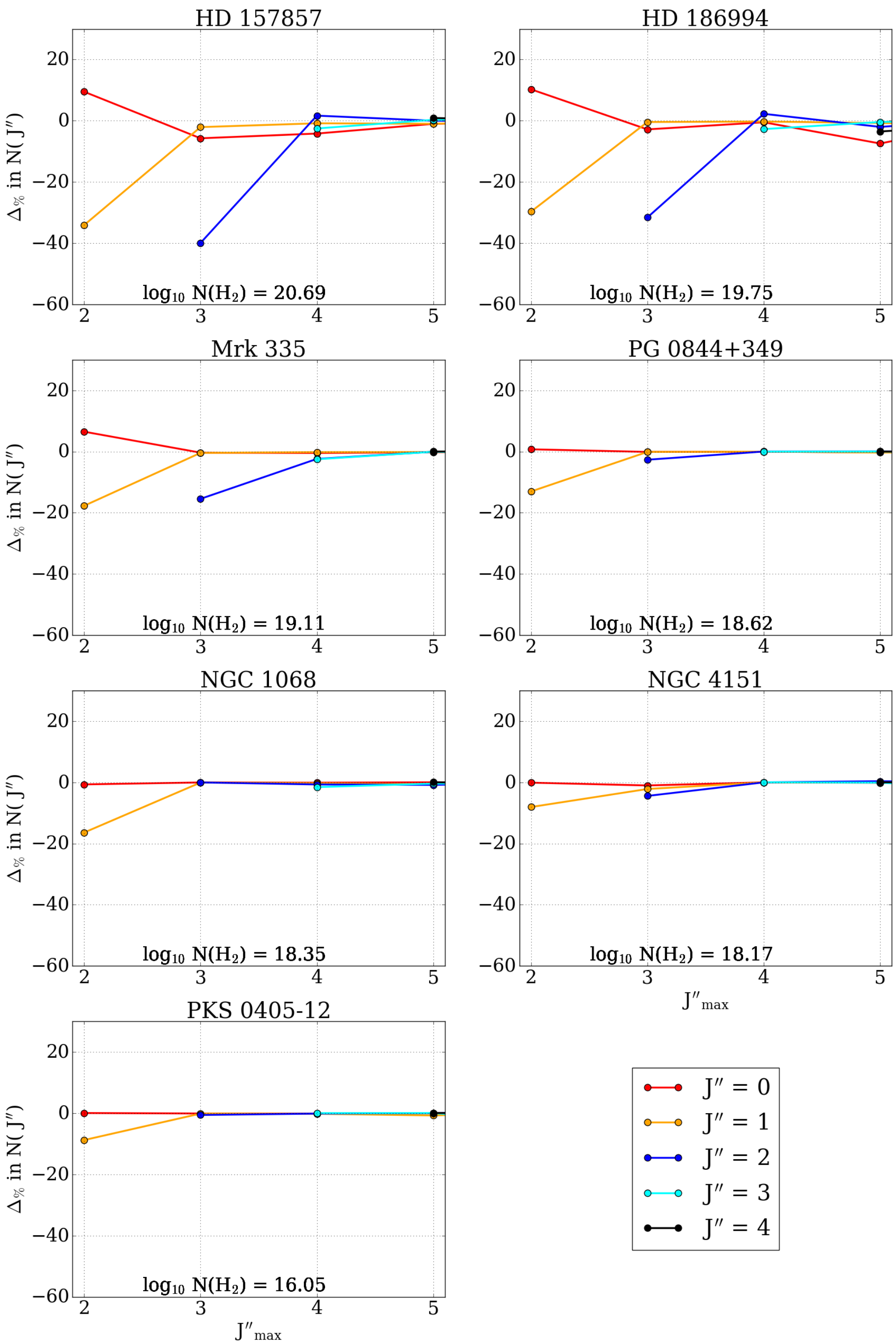

Figure 3.13: The $\Delta_{\%}$ in the column density of a J″ level as higher levels are included in the fitting routine, for the seven additional *FUSE* objects. The x-axis is the maximum J″ level included in a fit (e.g. $J''_{\text{max}} = 2$ had levels 0–2 included). The y-axis is the percent change, as defined by Equation 23.

Figure 4.1: The recoveries of CHESS-1 through 4.

stars. Across its four launches (Figure 4.1), CHESS further worked to flight certify emerging UV technologies, including a large format cross-strip MCP and gratings that were fabricated using new processes.

Preliminary attempts at fabricating an echelle using litographic and ion-etching techniques resulted in gratings that were too inefficient for use. While we ultimately used off-the-shelf echelle gratings, CHESS-2, CHESS-3, and CHESS-4 were still able to fulfill the basic science goals of the instrument. The inclusion of a curved echelle on CHESS-4 was also the first use of such a grating for space astronomy. Continued development of such a concept could improve spectrograph performance since the extra degrees of freedom allow for further aberration control.

We plan to continue the work of qualifying new grating technologies and ruling techniques.

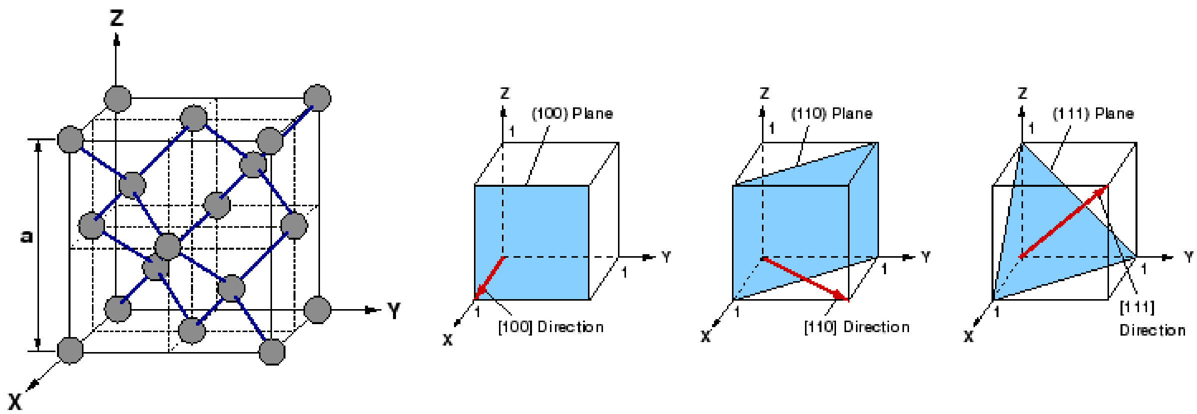

Figure 4.2: From Wittmann (2007). *Left:* The crystalline structure of Si. *Right:* The orientation of the three classes of crystal planes.

In particular, we have begun testing FUV gratings that are fabricated using a potassium hydroxide (KOH) etching technique to rule grooves into bulk silicon. This method is commonplace within the semi-conductor industry and has been utilized by the Nanofabrication Lab at Penn State University (PSU) to make blazed X-ray gratings (McEntaffer et al., 2013; McCoy et al., 2016). Silicon has a cubic crystalline structure, with three classes of crystal planes: $\langle 100\rangle$, $\langle 110\rangle$, and $\langle 111\rangle$ (Figure 4.2). KOH etches the Si by breaking apart the atomic bonds. Due to the number of exposed bonds in each plane, KOH etches through the $\langle 111\rangle$ plane at a much slower rate compared to the other two (see, e.g. Oosterbroek et al. 2000). This effect can be utilized to create blazed grating facets.

Similar to the lithographic and e-beam processes, a mask is first applied to the surface of a Si substrate, defining the groove locations. Any region that is not masked will be etched by the KOH along the $\langle 111\rangle$ plane. As a test, we ruled nine 25 mm x 25 mm echelle samples into a simple off-the-shelf 6-inch silicon wafer. The dopant and resistivity of the silicon do not significantly impact the final efficiency of the grating and so sourcing the silicon needed for this process can be simple, depending primarily on the desired blaze angle. For this work, we used the most commonly available silicon orientation, which had symmetric $\langle 111\rangle$ planes running diagonally though the silicon at 54.7° relative to the surface. Gratings ruled in this substrate have identical facets at blaze angles of 54.7° on each side of the grooves

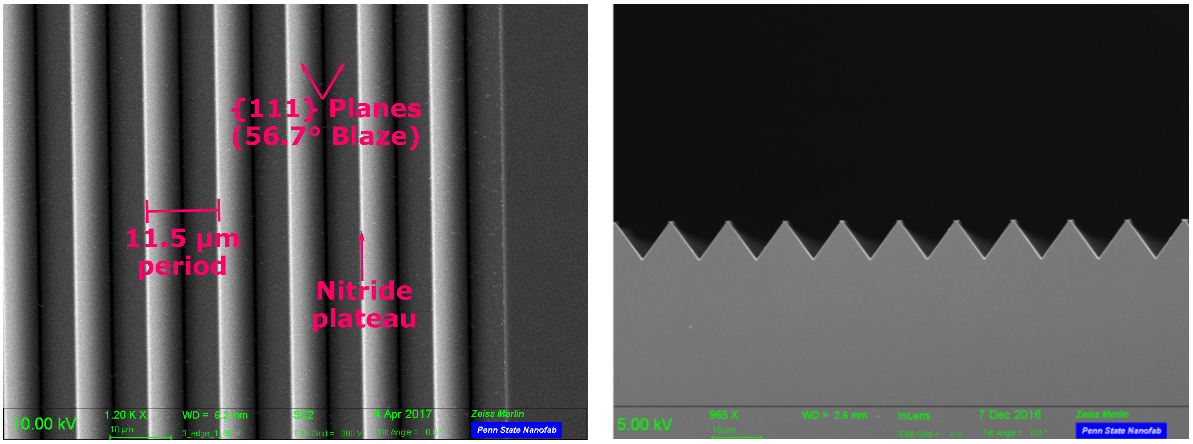

Figure 4.3: *Left:* Top view of a UV grating in Si from the PSU test samples. Labeled for reference are the period, blazed facets, and a nitride plateau that is a remanent of the mask. *Right:* Side view of a sample showing the resulting triangular groove profile.

once etched. This angle can be further customized by purchasing wafers that are cut at the desired angle relative to the ⟨111⟩ plane, in which case the facets are no longer symmetric. An example etched sample from our test is shown in Figure 4.3.

Theoretically, the grating facets should be smooth down to the atomic level, giving them efficiencies and scatter performance that exceed that of either mechanically- or holographically-ruled gratings (McEntaffer et al., 2013). The etched pattern is also determined by a laser-written mask that can record groove profiles at positional accuracies on the order of a few percent the width of the facet themselves. This allows for the recording of complex grating solutions, like those created by holographic processes. A comparison of the average peak order efficiency of the fabricated samples to that of the CHESS and STIS echelles are shown in Figure 4.4. We plan now to fabricate a replica of the CHESS echelle to compare its performance once installed in the instrument. We also plan on attempting the process on curved substrates.

Due to a fabrication error in the CHESS cross disperser, the instrument was unable to achieve its designed R $\gtrsim$ 100,000. Nonetheless, CHESS-2, -3, and -4 were all able to provide updated measurements of the H_2 along the sightlines of objects that had not been observed at $\lambda < 1150$ Å since *Copernicus*. For CHESS-3, we found N(H_2) and N(0) that agreed well with

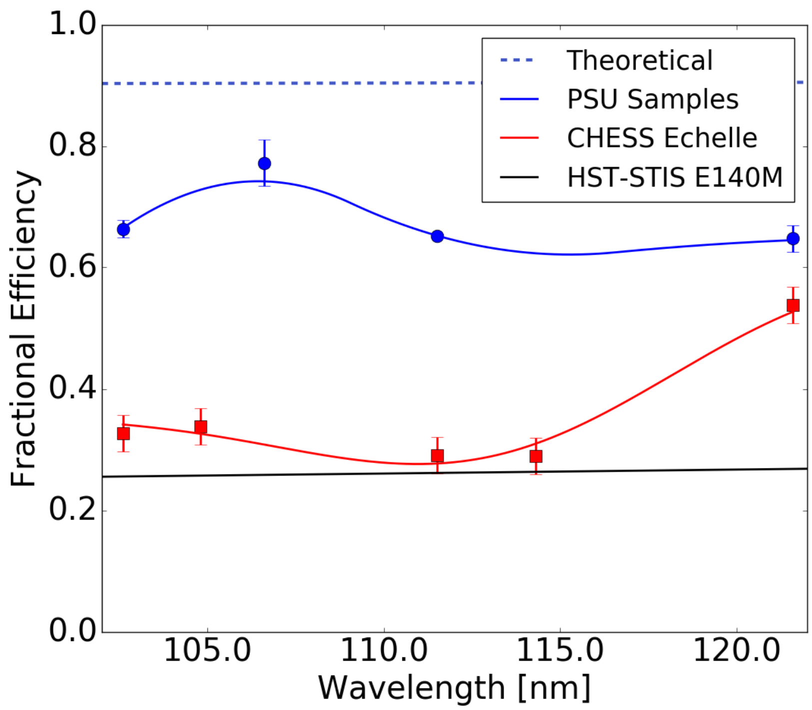

Figure 4.4: The average efficiency of the PSU samples (blue circles) and the CHESS flight echelle (red squares). The theoretical efficiency of the PSU gratings is plotted as a blue dashed line. The efficiency of the *HST*-STIS echelle, from Content et al. (1996), is plotted as a black line.

that of S77, but our N(1) results differed by ∼0.4 dex. This discrepancy lead to a reevaluation of the S77 results. In particular, we found that they did not include the (1-0)R(2) line in their analysis and this likely lead to a larger inferred N(1) value overall. This conclusion was supported by our CHESS-4 observations (although, with a larger uncertainty). To further explore this trend, we generated an extended data set comprised of *FUSE* and *Copernicus* observations and modeled their H_2 column densities following our CHESS procedure. We found that N(0) and N(1) were both impacted by the inclusion of the $J'' = 2$ level in the model. The magnitude of this effect further scaled with N(H_2) (Figure 3.12). By applying our measured trend to the values produced by S77, we find an updated average T_{01} of 68 ± 13 K for their sample of diffuse sightlines. We further caution against imposing limits on J'' when modeling H_2 absorption lines, since we find a similar interdependence between N(J'') levels up to at least $J'' = 5$ (Figure 3.13).

With the end of the CHESS instrument cycle, *HST*-COS is the only operational FUV instrument capable of continuing observations of the ISM at $\lambda < 1150$ Å. But, as noted in §1.7.2, those observations are limited to highly-reddened slightlines. Therefore, while *HST*-STIS continues to be capable of resolving CO lines, the incompatibility between STIS and COS sightlines means combined studies of CO and H_2 in diffuse and translucent clouds will not possible in the near term. While we were able to supply the updated H_2 observations along several sightlines, topics such as the depletions of metals and origin of the high J'' states of H_2 remain unanswered.

Continued progress on these topics relies on the development of high throughput and high resolution instruments. Currently, two large observatories are under study as potential *HST*-like, multi-instrument observing platforms. The first is the *Large UV/Optical/IR Surveyor* (*LUVOIR*), which has two potential designs. Architecture A has a 15-m primary and houses four instruments. Architecture B has an 8-m primary and houses three instruments (Bolcar et al., 2018). UV spectroscopy in both architectures is covered by two instruments. The first is the *LUVOIR* Ultraviolet Multi-Object Spectrograph (LUMOS), which is a multi-channel instrument, offering spectroscopy and imaging across the various optical paths. Of interest is the medium resolution FUV channel, which is designed to achieve R = 30,000–63,000 over a bandpass of 1000-3200 Å with an effective area >4.0$\times$ 10^4 cm^2 over most of that band (France et al., 2017). There is also a planned CHESS-like echelle channel, designed for R > 100,000. The second instrument is POLLUX, a high-resolution spectropolarimeter that is designed to achieve R $\sim$ 120,000 in its FUV channel (Muslimov et al., 2018). The polarization sensitivity of the instrument will open new avenues for study of the diffuse to translucent ISM. For example, the role of magnetic turbulence within clouds could be characterized (Yan & Lazarian, 2012; Bouret et al., 2018), which could feed into the energetics driving the high J'' states.

The second observatory under study is the *Habitable Exoplanet Observatory* (*HabEx*), which is baselined for a 4-m monolithic primary (although a 6.5-m version has also been considered) and houses four instruments. One of those instruments is a multi-object UV spectrograph that operates at R = 60,000 across 10 bands that span λ = 1150–3000 Å. The lower limit of 1150 Å is set by the planned MgF_2 coatings (Gaudi et al., 2018).

Several of the technological requirements cited by these missions look familiar, since CHESS has played a roll in their development. This includes holographic gratings, large format and high rate MCPs, and delta-doped detectors. While the ultimate science goals of CHESS were not achieved, it still played an important role in the on-going lineage of FUV observatories. *LUVOIR* and *HabEx*, if selected, are not slated to launch until at least 2035. This means it will likely be more than 15 years until high-signal, medium-to-high resolution observations of H_2 will again by possible. Until that time, the fundamental questions of the ISM may continue to remain a mystery (Indebetouw et al., 2001).

5 Bibliography

Abt, H. A. 1981, ApJS, 45, 437

Angel, D. W., Hunter, W. R., Tousey, R., & Hass, G. 1961, J. Opt. Soc. Am., 51, 913

Baxter, A. J., Wilson, B. G., & Green, D. W. 1969, ApJ, 155, L145

Beasley, M., Boone, C., Cunningham, N., Green, J., & Wilkinson, E. 2004, Appl. Opt., 43, 4633

Beasley, M., Burgh, E., & France, K. 2010, in Proc. SPIE, Vol. 7732, Space Telescopes and Instrumentation 2010: Ultraviolet to Gamma Ray, 773206

Benedict, M. 2011, Introduction to the physics of atoms, molecules, and photons, `http://titan.physx.u-szeged.hu/~dpiroska/atmolfiz/molecular_structure_and_spectra.html`, accessed: 2018-09-24

Bianchi, L., & Bohlin, R. C. 1984, A&A, 134, 31

Black, J. H., & Dalgarno, A. 1976, ApJ, 203, 132

—. 1977, ApJS, 34, 405

Boggess, A., Carr, F. A., Evans, D. C., et al. 1978, Nature, 275, 372

Bohlin, R. C. 1975, ApJ, 200, 402

Bohlin, R. C., Jenkins, E. B., Spitzer, Jr., L., et al. 1983, ApJS, 51, 277

Bolatto, A. D., Wolfire, M., & Leroy, A. K. 2013, ARA&A, 51, 207

Bolcar, M., Crooke, J., Hylan, J., et al. 2018, The large UV/optical/infrared surveyor (LUVOIR): decadal mission study update, doi:10.1117/12.2313350

Bouret, J.-C., Neiner, C., Gómez de Castro, A. I., et al. 2018, in Society of Photo-Optical Instrumentation Engineers (SPIE) Conference Series, Vol. 10699, Space Telescopes and Instrumentation 2018: Ultraviolet to Gamma Ray, 106993B

Brandt, J. C., Heap, S. R., Beaver, E. A., et al. 1994, PASP, 106, 890

Burgh, E. B., France, K., & Jenkins, E. B. 2010, ApJ, 708, 334

Burgh, E. B., France, K., & McCandliss, S. R. 2007, ApJ

Burstein, P., Borken, R. J., Kraushaar, W. L., & Sanders, W. T. 1977, ApJ, 213, 405

Buss, Jr., R. H., Allen, M., McCandliss, S., et al. 1994, ApJ, 430, 630

Bykov, S. V., Sharma, B., & Asher, S. A. 2013, Appl. Spectrosc., 67, 873

Cardelli, J., & Boehm-Vitense, E. 1982, ApJ, 262, 213

Cardelli, J. A., Ebbets, D. C., & Savage, B. D. 1990, ApJ, 365, 789

Cardelli, J. A., Savage, B. D., Bruhweiler, F. C., et al. 1991, ApJ, 377, L57

Carruthers, G. R. 1970, ApJ, 161, L81

Caselli, P., Walmsley, C. M., Terzieva, R., & Herbst, E. 1998, ApJ, 499, 234

Clark, B. G. 1965, ApJ, 142, 1398

Content, D. A., Boucarut, R. A., Bowers, C., et al. 1996, in Proc. SPIE, Vol. 2807, Space Telescopes and Instruments IV, ed. P. Y. Bely & J. B. Breckinridge, 267–278

Crocker, J. H. 1993, Opt. Photon. News, 4, 22

Crutcher, R. M. 1985, ApJ, 288, 604

Dalgarno, A., Black, J. H., & Weisheit, J. C. 1973, Astrophys. Lett., 14, 77

Dalgarno, A., & McCray, R. A. 1972, ARA&A, 10, 375

Davidsen, A. F., & Fountain, G. H. 1985, Johns Hopkins APL Technical Digest, 6, 28

Davidsen, A. F., Long, K. S., Durrance, S. T., et al. 1992, ApJ, 392, 264

Dickey, J. M., & Lockman, F. J. 1990, ARA&A, 28, 215

Dickman, R. L. 1975, ApJ, 202, 50

Draine, B. T. 2011, Physics of the Interstellar and Intergalactic Medium

Drake, J. F., Jenkins, E. B., Bertaux, J. L., Festou, M., & Keller, H. U. 1976, ApJ, 209, 302

Federman, S. R., Glassgold, A. E., Jenkins, E. B., & Shaya, E. J. 1980, ApJ, 242, 545

Ferrière, K. M. 2001, Reviews of Modern Physics, 73, 1031

Field, G. B., Goldsmith, D. W., & Habing, H. J. 1969, ApJ, 155, L149

Field, G. B., Somerville, W. B., & Dressler, K. 1966, ARA&A, 4, 207

Fleming, B., McCandliss, S., Kaiser, M., et al. 2011, Fabrication and calibration of FORTIS, doi:10.1117/12.894080

Fleming, B., Quijada, M., Hennessy, J., et al. 2017, Appl. Opt., 56, doi:10.1364/ao.56.009941

France, K., Hoadley, K., Fleming, B. T., et al. 2016, Journal of Astronomical Instrumentation, 5, 1640001

France, K., Nell, N., Kane, R., et al. 2013, ApJ, 772, L9

France, K., Fleming, B., West, G., et al. 2017, in Society of Photo-Optical Instrumentation Engineers (SPIE) Conference Series, Vol. 10397, Society of Photo-Optical Instrumentation Engineers (SPIE) Conference Series, 1039713

Gaudi, B. S., Seager, S., Mennesson, B., et al. 2018, arXiv e-prints, arXiv:1809.09674

Gerin, M., Neufeld, D. A., & Goicoechea, J. R. 2016, ARA&A, 54, 181

Gillmon, K., Shull, J. M., Tumlinson, J., & Danforth, C. 2006, ApJ, 636, 891

Green, J. C., Wilkinson, E., & Morse, J. A. 2003, in Future EUV/UV and Visible Space Astrophysics Missions and Instrumentation.

Green, J. C., Froning, C. S., Osterman, S., et al. 2012, ApJ, 744, 60

Grewing, M., Boksenberg, A., Seaton, M. J., et al. 1978, Nature, 275, 394

Gry, C., Boulanger, F., Nehmé, C., et al. 2002, A&A, 391, 675

Guélin, M. 1974, Free Electrons Outside H ii Regions, ed. F. J. Kerr & S. C. Simonson (Dordrecht: Springer Netherlands), 51–63

Hagen, J. P., Lilley, A. E., & McClain, E. F. 1955, ApJ, 122, 361

Hagen, J. P., & McClain, E. F. 1954, ApJ, 120, 368

Hagen, J. P., McClain, E. F., & Hepburn, N. 1954, AJ, 59, 323

Hass, G. 1955, J. Opt. Soc. Am., 45, 945

Heap, S. R., Brandt, J. C., Randall, C. E., et al. 1995, PASP, 107, 871

Hennessy, J., Jewell, A. D., Moore, C. S., et al. 2018, in Society of Photo-Optical Instrumentation Engineers (SPIE) Conference Series, Vol. 10699, Society of Photo-Optical Instrumentation Engineers (SPIE) Conference Series, 1069902

Hennessy, J., Moore, C. S., Balasubramanian, K., et al. 2017, in Society of Photo-Optical Instrumentation Engineers (SPIE) Conference Series, Vol. 10401, Society of Photo-Optical Instrumentation Engineers (SPIE) Conference Series, 1040119

Henry, R. C., Fritz, G., Meekins, J. F., Friedman, H., & Byram, E. T. 1968, ApJ, 153, L11

Hermanutz, S., Barnstedt, J., Diebold, S., et al. 2014, An introduction to the IAAT ultraviolet MCP detector development, doi:10.1117/12.2054888

Herzberg, G. 1950, Molecular spectra and molecular structure. Vol.1: Spectra of diatomic molecules (Prentice-Hall, New York)

Hill, A., Reynolds, R., Haffner, L., Wood, K., & Madsen, G. 2015, Highlights of Astronomy, 16, 574

Hoadley, K., France, K., Nell, N., et al. 2019, Experimental Astronomy, submitted

Hoadley, K., France, K., Nell, N., et al. 2014, in Proc. SPIE, Vol. 9144, Space Telescopes and Instrumentation 2014: Ultraviolet to Gamma Ray, 914406

Hoadley, K., France, K., Kruczek, N., et al. 2016, in Proc. SPIE, Vol. 9905, Space Telescopes and Instrumentation 2016: Ultraviolet to Gamma Ray, 99052V

Hollenbach, D. J., & Tielens, A. G. G. M. 1997, ARA&A, 35, 179

Howk, J. C., & Sembach, K. R. 2000, AJ, 119, 2481

Hoyle, F., & Ellis, G. R. A. 1963, Australian Journal of Physics, 16, 1

Hurwitz, M., & Bowyer, S. 1986, A High Resolution Spectrometer For EUV/FUV Wavelengths, doi:10.1117/12.968112

Indebetouw, R., McLean, R., Wilkinson, E., Green, J., & Beasley, M. 2001, Review of Scientific Instruments, 72, 1850

Jacquot, B. C., Monacos, S. P., Hoenk, M. E., et al. 2011, Review of Scientific Instruments, 82, 043102

Jenkins, E. B. 1975, Memo to Copernicus Astronomers and Guest Investigators: Computations of the U1 Instrument Profile

—. 2009, ApJ, 700, 1299

—. 2013, ApJ, 764, 25

Jenkins, E. B., Joseph, C. L., Long, D., Zucchino, P. M., & Carruthers, G. R. 1988, in Proc. SPIE, Vol. 932, Ultraviolet technology II, ed. R. E. Huffman, 213–229

Jenkins, E. B., & Meloy, D. A. 1974, ApJ, 193, L121

Jenkins, E. B., & Peimbert, A. 1997, ApJ, 477, 265

Jenkins, E. B., Reale, M. A., Zucchino, P. M., & Sofia, U. J. 1996, Ap&SS, 239, 315

Jenkins, E. B., & Tripp, T. M. 2001, ApJS, 137, 297

Jenkins, E. B., Woźniak, P. R., Sofia, U. J., Sonneborn, G., & Tripp, T. M. 2000, ApJ, 538, 275

Jensen, A. G., Snow, T. P., Sonneborn, G., & Rachford, B. L. 2010, ApJ, 711, 1236

Kane, R., Nell, N., Schultz, T., et al. 2013, in Proc. SPIE, Vol. 8859, UV, X-Ray, and Gamma-Ray Space Instrumentation for Astronomy XVIII, 885912

Klessen, R. S., & Glover, S. C. O. 2016, Star Formation in Galaxy Evolution: Connecting Numerical Models to Reality, Saas-Fee Advanced Course, Volume 43. ISBN 978-3-662-47889-9. Springer-Verlag Berlin Heidelberg, 2016, p. 85, 43, 85

Kriss, G. A., Blustin, A., Branduardi-Raymont, G., et al. 2003, A&A, 403, 473

Kruczek, N., Nell, N., France, K., et al. 2017, in SPIE, Vol. 10397, Society of Photo-Optical Instrumentation Engineers (SPIE) Conference Series, 103971G

Kruczek, N., Nell, N., France, K., et al. 2018, in SPIE, Vol. 10699, Space Telescopes and Instrumentation 2018: Ultraviolet to Gamma Ray, 106990K

Lacour, S., Ziskin, V., Hébrard, G., et al. 2005, ApJ, 627, 251

Lacy, J. H., Knacke, R., Geballe, T. R., & Tokunaga, A. T. 1994, ApJ, 428, L69

Landsman, W., & Bowers, C. 1997, in The 1997 HST Calibration Workshop with a New Generation of Instruments, ed. S. Casertano, R. Jedrzejewski, T. Keyes, & M. Stevens, 132

Le Bourlot, J., Pineau des Forêts, G., & Flower, D. R. 1999, MNRAS, 305, 802

Lerner, J. M., Flamand, J., Laude, J. P., Passereau, G., & Thevenon, A. 1981, in Proc. SPIE, Vol. 240, Society of Photo-Optical Instrumentation Engineers (SPIE) Conference Series, ed. C. H. Chi, E. G. Loewen, & C. L. O'Bryan, 82–89

Lumb, D. H., Berthiaume, G. D., Burrows, D. N., Garmire, G. P., & Nousek, J. A. 1991, Experimental Astronomy, 2, 179

Manchester, R. N. 1972, ApJ, 172, 43

Martin, R. N., & Barrett, A. H. 1978, ApJS, 36, 1

McCandliss, S. R. 2003, PASP, 115, 651

McCandliss, S. R., Burgh, E. B., & Feldman, P. D. 2000, in Proc. SPIE, Vol. 4139, Instrumentation for UV/EUV Astronomy and Solar Missions, 413970

McCandliss, S. R., France, K., Osterman, S., et al. 2010, ApJ, 709, L183

McCoy, J., McEntaffer, R., & DeRoo, C. 2016, in Proc. SPIE, Vol. 9905, Space Telescopes and Instrumentation 2016: Ultraviolet to Gamma Ray, 990524

McCray, R., & Kafatos, M. 1987, ApJ, 317, 190

McEntaffer, R., DeRoo, C., Schultz, T., et al. 2013, Experimental Astronomy, 36, 389

McKee, C. F., & Ostriker, J. P. 1977, ApJ, 218, 148

McPhate, J. B., Siegmund, O. H., Gaines, G. A., Vallerga, J. V., & Hull, J. S. 2000, in Proc. SPIE, Vol. 4139, Instrumentation for UV/EUV Astronomy and Solar Missions, ed. S. Fineschi, C. M. Korendyke, O. H. Siegmund, & B. E. Woodgate, 25–33

Meijer, A. J. H. M., Farebrother, A. J., Clary, D. C., & Fisher, A. J. 2001, Journal of Physical Chemistry A, 105, 2173

Merrill, P. W. 1934, PASP, 46, 206

Moos, H. W., Cash, W. C., Cowie, L. L., et al. 2000, ApJ, 538, L1

Morton, D. C., Drake, J. F., Jenkins, E. B., et al. 1973, ApJ, 181, L103

Morton, D. C., & Hu, E. M. 1975, ApJ, 202, 638

Muslimov, E., Bouret, J.-C., Neiner, C., et al. 2018, in Society of Photo-Optical Instrumentation Engineers (SPIE) Conference Series, Vol. 10699, Space Telescopes and Instrumentation 2018: Ultraviolet to Gamma Ray, 1069906

NASA. 2003, Copernicus (OAO-3), `https://heasarc.gsfc.nasa.gov/docs/copernicus/copernicus_about.html`, accessed: 2018-10-16

—. 2013, Hopkins Ultraviolet Telescope, `https://archive.stsci.edu/hut/index.html`, accessed: 2018-10-20

Nell, N., France, F., Harwit, A., et al. 2016, Characterization of an ultraviolet imaging detector with high event rate ROIC (HEROIC) readout, doi:10.1117/12.2233816

Nikzad, S., Hoenk, M. E., Grunthaner, P. J., et al. 1994, in Proc. SPIE, Vol. 2198, Instrumentation in Astronomy VIII, ed. D. L. Crawford & E. R. Craine, 907–915

Nikzad, S., Jewell, A. D., Hoenk, M. E., et al. 2017, Journal of Astronomical Telescopes, Instruments, and Systems, 3, 036002

Oosterbroek, R. E., Berenschot, J. W., Jansen, H. V., et al. 2000, Journal of Microelectromechanical Systems, 9, 390

Palmer, C. 1989, Journal of the Optical Society of America A, 6, 1175

Palmer, C., & Loewen, E. 2005, Diffraction Grating Handbook (Newport Corporation)

Pellerin, A., Fullerton, A. W., Robert, C., et al. 2002, ApJS, 143, 159

Prinja, R. K., Massa, D., Fullerton, A. W., Howarth, I. D., & Pontefract, M. 1997, A&A, 318, 157

Rachford, B. L., Snow, T. P., Tumlinson, J., et al. 2002, ApJ, 577, 221

Rachford, B. L., Snow, T. P., Destree, J. D., et al. 2009, ApJS, 180, 125

Redfield, S. 2006, in Astronomical Society of the Pacific Conference Series, Vol. 352, New Horizons in Astronomy: Frank N. Bash Symposium, ed. S. J. Kannappan, S. Redfield, J. E. Kessler-Silacci, M. Landriau, & N. Drory, 79

Reynolds, R. J., Scherb, F., & Roesler, F. L. 1973, ApJ, 185, 869

Robinson, R. D., Ake, T. B., Lindler, D. J., et al. 1998, PASP, 110, 68

Rogerson, J. B., Spitzer, L., Drake, J. F., et al. 1973, ApJ, 181, L97

Rybicki, G. B., & Lightman, A. P. 1979, Radiative processes in astrophysics

Sahnow, D. J., Moos, H. W., Ake, T. B., et al. 2000, ApJ, 538, L7

Sanders, D. B., Solomon, P. M., & Scoville, N. Z. 1984, ApJ, 276, 182

Savage, B. D., Bohlin, R. C., Drake, J. F., & Budich, W. 1977, ApJ, 216, 291

Savage, B. D., & Sembach, K. R. 1996, ARA&A, 34, 279

Scowen, P. A., Tripp, T., Beasley, M., et al. 2017, PASP, 129, 076001

Sharp, T. 1970, Atomic Data, 2, 119

Sheffer, Y., Rogers, M., Federman, S. R., et al. 2008, ApJ, 687, 1075

Shull, J. M., & Beckwith, S. 1982, ARA&A, 20, 163

Siegmund, O. H. W., Tremsin, A. S., & Vallerga, J. V. 2009, in Proc. SPIE, Vol. 7435, UV, X-Ray, and Gamma-Ray Space Instrumentation for Astronomy XVI, 74350L

Smith, A. M., Bruhweiler, F. C., Lambert, D. L., et al. 1991, ApJ, 377, L61

Snow, T. P., Destree, J. D., Burgh, E. B., et al. 2010, ApJ, 720, L190

Snow, T. P., & McCall, B. J. 2006, ARA&A, 44, 367

Sommerfeld, A. 1930, Wave Mechanics (Methuen, London)

Sonnentrucker, P., Friedman, S. D., Welty, D. E., York, D. G., & Snow, T. P. 2003, ApJ, 596, 350

Sonnentrucker, P., Welty, D. E., Thorburn, J. A., & York, D. G. 2007, ApJS, 168, 58

Spitzer, L., Drake, J. F., Jenkins, E. B., et al. 1973, ApJ, 181, L116

Spitzer, Jr., L., & Cochran, W. D. 1973, ApJ, 186, L23

Spitzer, Jr., L., Cochran, W. D., & Hirshfeld, A. 1974, ApJS, 28, 373

Stark, A. A., Gammie, C. F., Wilson, R. W., et al. 1992, ApJS, 79, 77

Stecher, T. P., & Williams, D. A. 1967, ApJ, 149, L29

STSCI. 2017, HST Cycle 26 Primer Optical Performance, Guiding Performance, and Observing Efficiency, `https://hst-docs.stsci.edu/display/HSP/HST+Cycle+26+Primer+Optical+Performance%2C+Guiding+Performance%2C+and+Observing+Efficiency`, accessed: 2018-10-20

Swings, P., & Rosenfeld, L. 1937, ApJ, 86, 483

Takahashi, J., Masuda, K., & Nagaoka, M. 1999, ApJ, 520, 724

Thomas, R. J. 2003, in Proc. SPIE, Vol. 4853, Innovative Telescopes and Instrumentation for Solar Astrophysics, ed. S. L. Keil & S. V. Avakyan, 411–418

Tielens, A. G. G. M., & Allamandola, L. J. 1987, in Astrophysics and Space Science Library, Vol. 134, Interstellar Processes, ed. D. J. Hollenbach & H. A. Thronson, Jr., 397–469

Timothy, J. G., & Bybee, R. L. 1986, in Proc. SPIE, Vol. 687, Society of Photo-Optical Instrumentation Engineers (SPIE) Conference Series, 109–116

Tumlinson, J., Shull, J. M., Rachford, B. L., et al. 2002, ApJ, 566, 857

Valenti, J., Busko, I., Quijano, J. K., Lindler, D., & Bowers, C. W. 2003, in HST Calibration Workshop : Hubble after the Installation of the ACS and the NICMOS Cooling System, ed. S. Arribas, A. Koekemoer, & B. Whitmore, 209

Vallerga, J., Raffanti, R., Tremsin, A., et al. 2010, in Proc. SPIE, Vol. 7732, Space Telescopes and Instrumentation 2010: Ultraviolet to Gamma Ray, 773203

Vallerga, J. V., McPhate, J. B., Martin, A. P., et al. 2001, in Proc. SPIE, Vol. 4498, UV/EUV and Visible Space Instrumentation for Astronomy and Solar Physics, ed. O. H. Siegmund, S. Fineschi, & M. A. Gummin, 141–151

van Dishoeck, E. F., & Black, J. H. 1988, ApJ, 334, 771

—. 1989, ApJ, 340, 273

Wagenblast, R. 1992, MNRAS, 259, 155

Wakker, B. P. 2006, ApJS, 163, 282

Williams, D. A. 2005, in Journal of Physics Conference Series, Vol. 6, Journal of Physics Conference Series, 1–17

Wittmann, R. 2007, PhD thesis, Vienna University of Technology

Wolfire, M. G., McKee, C. F., Hollenbach, D., & Tielens, A. G. G. M. 2003, ApJ, 587, 278

Wolniewicz, L., Simbotin, I., & Dalgarno, A. 1998, ApJS, 115, 293

Wood, K., Hill, A. S., Joung, M. R., et al. 2010, ApJ, 721, 1397

Woodgate, B. E., Kimble, R. A., Bowers, C. W., et al. 1998, PASP, 110, 1183

Yan, H., & Lazarian, A. 2012, Journal of Quantitative Spectroscopy and Radiative Transfer, 113, 1409

York, D. G. 1974, ApJ, 193, L127